THERMAL MODELLING OF CYLINDRICAL LI-ION BATTERY CELL

Lappeenranta–Lahti University of Technology LUT

Master’s thesis

Master’s programme in Energy Technology

2025

Soroush Mostafaie

Examiners: Docent Aki-Pekka Grönman

Professor Pertti Kauranen

ABSTRACT

Lappeenranta–Lahti University of Technology LUT
LUT School of Energy Systems
Energy Engineering

Soroush Mostafaie

THERMAL MODELLING OF CYLINDRICAL LI-ION BATTERY CELL

Master's thesis
2024
86 pages, 39 figures, 4 tables and 1 appendices
Examiners: Docent Aki-Pekka Grönman and Professor Pertti Kauranen

Keywords: Li-ion Battery, Thermal, Temperature, Modelling.

This thesis investigates the thermal behaviour of a commercial 21700 NCA lithium-ion cell through combined experimental characterisation and lumped thermal modelling. The work focuses on quantifying heat generation mechanisms and predicting temperature evolution under various operating conditions. Experimental measurements include open-circuit voltage profiling, entropic heat coefficient determination, heat-transfer coefficient estimation, and charge–discharge cycling at 0.5C, 1C, and 2C. Additional calorimetric experiments are conducted to validate the thermal model under controlled thermal boundary conditions. The modelling framework incorporates reversible and irreversible heat generation, temperature-dependent parameters, and a thermal time constant extracted from cooling-curve analysis. Model predictions are evaluated against measured temperature responses, showing reasonable agreement across all tested C-rates. The results highlight the influence of current rate on heat generation, voltage relaxation, and thermal response, while demonstrating the suitability of a calibrated lumped model for representing the thermal dynamics of cylindrical Li-ion cells. The developed methodology provides a practical foundation for future battery thermal management design and for scaling cell-level thermal characteristics to module-level simulations.

ACKNOWLEDGEMENTS

I would like to express my sincere gratitude to my supervisor, Prof. Pertti Kauranen, for his invaluable guidance, constructive feedback, and continuous support throughout the course of this thesis. His expertise, encouragement, and trust in my work have been fundamental to the successful completion of this research. This thesis was conducted within the framework of the Flexible Clean Propulsion Technologies project, and I gratefully acknowledge the financial support provided by Business Finland.

I also wish to thank the members of the Renewable Electricity Generation and Energy Storage Laboratory at LUT University for fostering a supportive, collaborative, and motivating research environment. Their willingness to share knowledge, offer assistance, and provide access to laboratory facilities greatly contributed to the progress of this work.

Finally, I extend my heartfelt appreciation to my family and friends for their unwavering support, patience, and encouragement throughout this journey. Their belief in me has been a constant source of strength.

SYMBOLS AND ABBREVIATIONS

Roman characters

A	Area	m^2
C_p	Specific heat capacity	$J.K^{-1}.kg^{-1}$
C_n	Battery capacity	A.h
h	Heat transfer coefficient	$W.m^{-2}.K^{-1}$
I	Current	A
P	Generated heat	J
T	Temperature	ºC
τ	Time constant	s
U	Voltage	V
V	Voltage	V

Subscripts

a	Ambient temperature
conv	Convection
diss	Dissipation
exp	Experimental
max	Maximum
min	Minimum
n	Nominal
ocv	Open circuit voltage
ohm	Ohmic overpotential
rad	Radiation

sim	Simulation
0	Initial

Abbreviations

AI	Artificial intelligence
ANN	Artificial neural networks
BEV	Battery electric vehicle
BMS	Battery management system
BTMS	Battery thermal management systems
CC	Constant Current
CCD	Cyclic Charge and Discharge
CV	Constant Voltage
DMC	Dimethyl carbonate
EC	Ethylene carbonate
ECM	Equivalent circuit models
EHC	Entropic heat coefficient
EV	Electric vehicles
HP	Heat pipe
HPPC	Hybrid pulse power characterization
IEC	International electrotechnical commission
IHTA	Inverse heat transfer analysis
ISC	Internal short circuit
LCO	Lithium Cobalt Oxide
LFP	Lithium iron phosphate

LIB	Lithium-ion battery
LMO	Lithium manganese oxide
LSPM	Lumped single particle model
NCA	Lithium nickel cobalt aluminium Oxide
NMC	Lithium nickel manganese cobalt oxide
NREL	National renewable energy laboratory
OCV	Open-circuit voltage
PDE	Partial differential equation
PEG	Polyethylene glycols
PET	Polyethylene Terephthalate
P2D	Pseudo-2D
RC	Resistor-capacitor
RSME	Root mean square error
SEI	Solid electrolyte interphase
SOH	State of health
SPM	Single particle model
SVM	Support vector machine
3D	Three-dimensional

Abstract

Acknowledgements

Symbols and abbreviations

Table of Contents

1 Introduction 9
  1.1 Lithium-ion Batteries Overview 9
    1.1.1 Working Principles of Lithium-ion Batteries 10
    1.1.2 Overview of Li-ion Battery Cell Formats 11
    1.1.2.1 Cylindrical Cells 12
    1.1.2.2 Pouch Cells 12
    1.1.2.3 Prismatic Cells 13
    1.1.2.4 Coin Cells 13
    1.1.3 Overview of Li-ion Battery Chemistries 14
    1.1.4 Thermal Runaway in Lithium-ion Batteries 17
  1.2 Battery Thermal Management Systems (BTMS) 18
    1.2.1 Active Cooling 20
    1.2.1.1 Air Cooling 21
    1.2.1.2 Liquid Cooling 22
    1.2.2 Passive Cooling 24
    1.2.2.1 Phase Change Materials (PCM) 24
    1.2.2.2 Heat Pipes 27
    1.2.3 Hybrid 28
  1.3 LIB Modelling Approaches 29
    1.3.1 Electrochemical Modelling 30
    1.3.1.1 Heterogeneous Models 30
    1.3.1.2 Pseudo-2D (P2D) Models 32
    1.3.1.3 Single Particle Models (SPM) 33
    1.3.1.4 Lumped Single Particle Models 34
    1.3.2 Equivalent Circuits Models (ECM) 35
    1.3.3 Machine Learning 36
2 Thermal Modelling 37
  2.1 Cell Modelling 37

2.1.1 Heat Generation in LIBs 38
2.1.2 Heat Transfer in LIBs 39
2.1.3 Previous works on Cell Modelling 42
2.2 Battery Module Modelling 45
2.2.1 Previous works on Module Modelling 46
3 Characterization Methods 50
3.1 Open Circuit Voltage (OCV) Measurements 51
3.2 Cycling 53
3.3 Heat Transfer Coefficient Measurement 54
3.4 Calorimetric Cycling Experiments 55
4 Single Cell Modelling 57
4.1 MATLAB Implementation 57
4.2 Error Analysis 59
4.2.1 Root Mean Square Error (RMSE) 59
4.2.2 Error Percentage 59
5 Results 60
5.1 Heat Transfer Coefficient 60
5.2 Reference OCV Measurements 61
5.3 OCV at Different Temperature Measurements 63
5.4 Entropic Heat Coefficient 63
5.5 Charge-discharge cycling 65
5.5.1 Results at 0.5C-Rate 65
5.5.2 Results at 1C-Rate 67
5.5.3 Results at 2C-Rate 69
5.6 Calorimetric Results 71
6 Conclusion 73
7 References 75

Appendices

Appendix 1. Experimental and Modelling Temperature Results at Different C-Rates

1 Introduction

Lithium-ion batteries are widely used in portable electronics, electric vehicles, and energy-storage systems due to their high energy density, long cycle life, and efficient performance. However, their thermal behavior remains a critical challenge, as temperature strongly influences internal resistance, ageing, safety, and overall performance. Understanding and predicting heat generation is therefore essential for ensuring reliable and safe battery operation.

During charge and discharge, electrochemical processes generate heat through both irreversible losses and reversible thermodynamic effects. The magnitude of this heat depends on the operating conditions, cell chemistry, and physical design of the cell. Cylindrical cells are widely adopted due to their robustness and manufacturing practicality, but their compact geometry can result in significant temperature rise under high current loads.

This thesis investigates the thermal behavior of a 21700 NCA cylindrical cell by developing a lumped thermal model capable of predicting cell temperature during operation. The model incorporates experimentally measured open-circuit voltage, entropic heat coefficients, and a thermal time constant obtained from cooling-curve analysis. Experimental characterization, including open circuit voltage (OCV) profiling, charge and discharge cycling at various C-rates, and calorimetric tests, provides the input data required to validate the model.

The objective of this work is to characterize the heat generation of the cell and develop a calibrated thermal model that can support future thermal management strategies for cylindrical lithium-ion batteries.

1.1 Lithium-ion Batteries Overview

The development of lithium-ion batteries began in the early 1980s in response to the demand for lightweight, high-capacity rechargeable power sources. Dr. Akira Yoshino created the first practical lithium-ion battery prototype in 1983, using lithium cobalt oxide ($LiCoO_2$) as the cathode and polyacetylene as the anode. The technology was patented in 1985, and commercialized by Sony in 1991, marking the beginning of a new era in energy storage (Yoshino, 2012).

In everyday usage, the term battery is often applied to any electrochemical energy storage device, whether it is a single cell, a module, or a complete battery pack. A cell is the fundamental electrochemical unit that converts chemical energy directly into electrical energy. When multiple cells are electrically connected, typically in series or parallel, they form a module, which increases the overall voltage or capacity. Several modules, combined with monitoring, control units, fuses, cooling systems, and structural enclosures, form a battery pack, which is the fully functional system used in applications such as electric vehicles or energy storage systems. Although some definitions specify that a battery must contain at least two cells, this distinction is not always upheld. In consumer and technical contexts alike, the term "battery" may refer to a single cell, a module, or a pack depending on the level of integration. In this thesis, the term “cell” will be used to refer specifically to the electrochemical unit, while “battery” will denote either the complete energy storage assembly or be specified further as a module or pack, depending on context. (Linden & Reddy, 2001).

1.1.1 Working Principles of Lithium-ion Batteries

A lithium-ion (Li-ion) battery consists of active materials at the positive and negative electrodes, an electrolyte, and a separator. The separator functions as a barrier between the electrodes to prevent short circuits. The active materials are responsible for the oxidation and reduction reactions that drive battery operation. These reactions occur through an intercalation process, where lithium ions are inserted into or removed from host materials without causing significant structural changes. Typically, the positive electrode is made of a lithium metal oxide or phosphate, while the negative electrode is composed of graphite. The electrolyte contains a lithium salt, such as $LiPF_6$, dissolved in a mixture of organic solvents like ethylene carbonate (EC) and dimethyl carbonate (DMC). Aluminium and copper are commonly used as current collectors for the positive and negative electrodes, respectively(Energy, 2021).

During discharge as shown in Figure 1, lithium ions are de-intercalated from the negative electrode and intercalated into the positive electrode, while Li in negative electrode undergoes oxidation and the Li-ions in the positive electrode undergo reduction. This movement of lithium ions is driven by the potential difference between the electrodes, and electrons flow through an external circuit, producing an electric current. When the battery is charged, the process is reversed: lithium ions move from the positive to the negative electrode. In the initial cycles, parasitic reactions between the electrolyte and the negative electrode form a passivation layer known as the solid–electrolyte interphase (SEI). The formation of this layer results in an irreversible loss of lithium, which can cause a small reduction in capacity. However, the rated capacity of a Li-ion cell accounts for this initial loss (Energy, 2021).

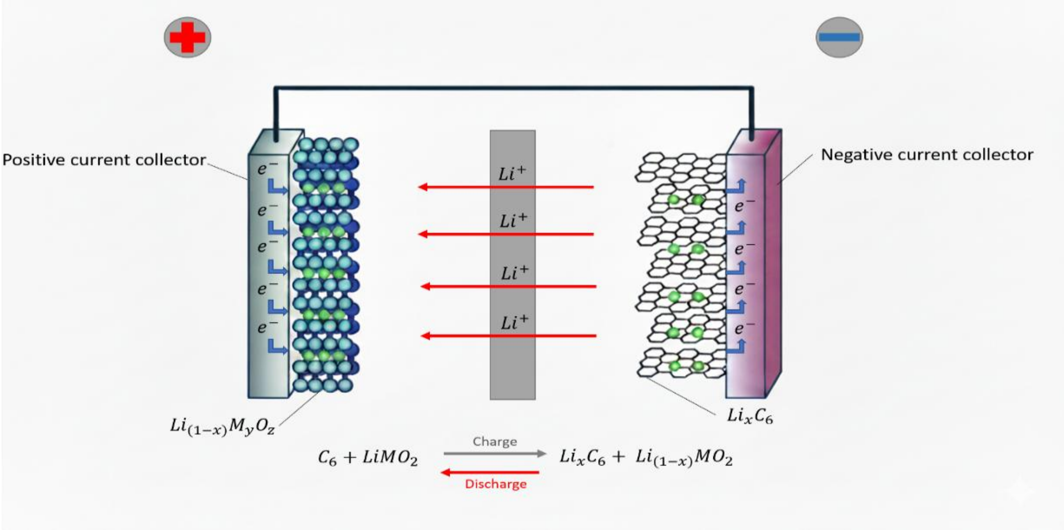

Figure 1 Discharging Process of a Lithium-ion Battery (Korthauer, 2018)

1.1.2 Overview of Li-ion Battery Cell Formats

Lithium-ion batteries are manufactured in several standardized cell formats, each designed to meet specific requirements related to energy density, mechanical stability, thermal performance, and packaging efficiency (Horiba, 2014). Although the fundamental electrochemical principles are identical across all configurations, the external geometry and internal assembly strongly influence the cell’s behaviour, integration flexibility, and suitability for different applications. The most common commercial formats include cylindrical, prismatic, pouch, and coin cells, each offering distinct advantages and trade-offs in terms of performance, safety, and manufacturing complexity. A brief overview of these cell types is presented below. Figure 2 illustrates the various lithium-ion cell formats currently available on the market, and the following sections describe each type in detail.

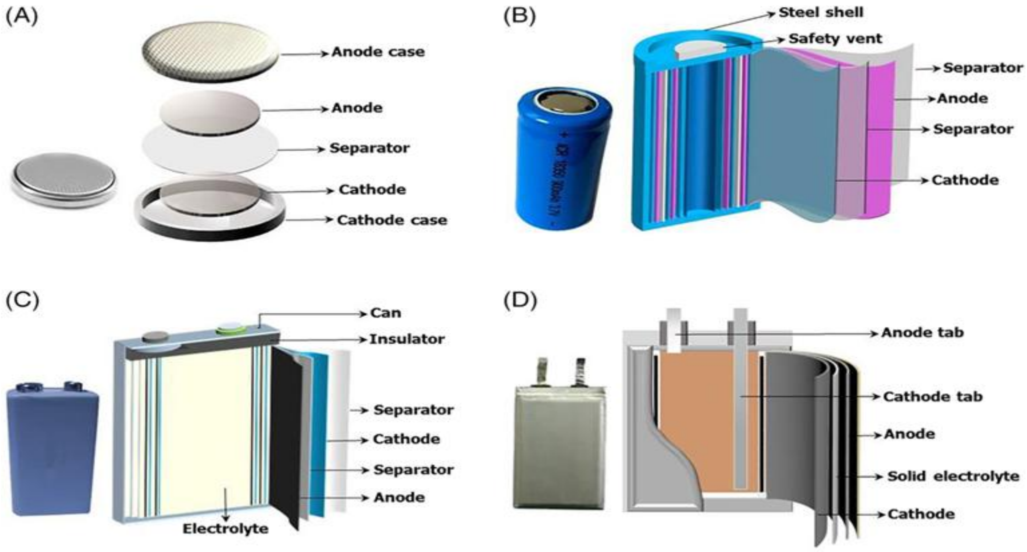

Figure 2 Schematic Representation of Common Lithium-ion batteries: (A) coin cell, (B) cylindrical cell, (C) prismatic cell, and (D) pouch cell (Liang et al., 2019).

1.1.2.1 Cylindrical Cells

In cylindrical cells, the electrodes and separator are rolled tightly in a spiral configuration and enclosed within a cylindrical casing. These cells feature a robust body with flat terminals, offering high cycle stability but relatively low packaging efficiency. Cylindrical cells are typically identified using five-digit codes; for instance, the widely used 18650 cell has a diameter of 18 mm and a length of 65.0 mm. Other commonly used cylindrical formats include 14500, 14650, 18500, 21700, 26650, and 32650. These cells are frequently used in applications such as laptops, medical devices, communication systems, e-bikes, power tools, and security equipment (Arote, 2022).

1.1.2.2 Pouch Cells

Pouch cells are characterized by their flexible, lightweight design, which utilizes laminated aluminium foil as the outer casing instead of a rigid metal enclosure. This structure enables exceptionally high packaging efficiency, over 90%, along with reduced weight and greater design flexibility, making pouch cells particularly suitable for compact electronic devices and space-constrained applications. Internally, they consist of stacked layers of anodes and cathodes, separated by a porous non-conductive separator. These components are enclosed in a multi-layered laminate: the innermost layer is a heat-sealable, electrolyte-resistant polymer (e.g., modified polypropylene), the middle layer is aluminium for barrier protection and thermal conductivity, and the outer layer is typically a durable polymer such as nylon or polyethylene terephthalate (PET), providing mechanical strength, insulation, and printability. Electrical connectivity is established by welding metallic tabs to the current collectors, allowing external connections. Despite their many advantages, pouch cells are more vulnerable to mechanical damage compared to rigid battery formats (Gopinadh et al., 2022).

1.1.2.3 Prismatic Cells

Prismatic cells use a semi-rigid or rigid rectangular casing, often made of aluminium or steel, providing high structural stability. The internal components, electrodes and separator, are stacked in sheets. These cells are preferred for space-constrained applications where minimizing swelling is important. They are marked with six-digit codes. For example, a 504050 cell measures 5.0 mm in thickness, 40 mm in width, and 50 mm in length (Arote, 2022).

1.1.2.4 Coin Cells

Coin cells, also known as button cells, are small, circular batteries commonly used in compact, portable devices such as wristwatches, LED lights, healthcare instruments (e.g., glucose meters, thermometers, heart rate monitors), calculators, remote controls, and car keys. These batteries typically consist of a stainless-steel casing, a graphite-coated copper foil serving as the anode (Purwamargapratala et al., 2020). The diameter of a coin cell is greater than its height, giving it its distinctive shape.

Lithium-ion coin cell formats follow International Electrotechnical Commission (IEC) standards and are designated by prefixes such as “LIR.” In this nomenclature, the letters indicate a rechargeable lithium-ion chemistry, while the numerical code specifies the cell diameter and thickness in tenths of a millimeter (e.g., LIR2032 corresponds to 20 mm × 3.2

mm). These cells typically consist of a stainless-steel case and cap, a separator, a graphite-based anode, a lithium-intercalating cathode material, and an electrolyte. Common rechargeable lithium-ion coin cell formats include LIR2032, LIR2025, and LIR2450 (Arote, 2022).

1.1.3 Overview of Li-ion Battery Chemistries

Lithium-ion batteries are composed of various chemistries, each offering distinct advantages and trade-offs in terms of energy density, safety, lifespan, and cost. The cathode material plays a critical role in determining the overall performance and suitability of the battery for specific applications. Lithium cobalt oxide ($LiCoO_2$, LCO) is widely used in portable electronics due to its high energy density, although it suffers from thermal instability and moderate cycle life. Lithium manganese oxide ($LiMn_2O_4$, LMO) provides improved thermal stability and safety but has a shorter lifespan, making it suitable for power tools and some electric vehicles (Horiba, 2014). Lithium iron phosphate ($LiFePO_4$, LFP) offers outstanding thermal stability and long cycle life, making it a preferred choice for electric vehicles and stationary storage, despite its lower energy density (Stan et al., 2014). Lithium nickel manganese cobalt oxide ($LiNiMnCoO_2$, NMC) represents a balanced option, combining good energy density, power capability, and cycle life, and is widely adopted in electric mobility solutions (Horiba, 2014). Lithium nickel cobalt aluminium oxide ($LiNiCoAlO_2$, NCA) delivers high specific energy and long lifespan, and is commonly found in premium electric vehicles, though it poses certain safety and cost concerns (Stan et al., 2014).

Alongside the cathode, the anode material contributes significantly to the overall behaviour and performance of the battery. Graphite remains the dominant commercial anode material due to its structural stability and reliable lithium-intercalation behaviour. However, its moderate theoretical capacity and susceptibility to lithium plating at high charge rates present notable limitations, motivating the development of higher-capacity and more robust anode alternatives (X. Chen et al., 2025; Koech et al., 2024). Silicon provides exceptionally high theoretical capacity and demonstrates strong electrochemical performance, but its large volume expansion during lithiation leads to stress, cracking, and instability of the SEI layer. To mitigate these effects, silicon is often incorporated into structured or composite designs that help accommodate the volume change and preserve mechanical integrity (Dasari &

Eisenbraun, 2021; Koech et al., 2024). Lithium titanate (LTO) is identified as a promising anode material due to its minimal volume change during cycling, which provides strong structural stability and improved safety compared with graphite. Although LTO exhibits low electronic conductivity and a moderate theoretical capacity, its performance can be substantially enhanced through nanostructured and composite material designs. LTO-based composites demonstrate reduced charge-transfer resistance, improved rate capability, and excellent cycling stability, achieving 97.2% capacity retention at 10C after 1000 cycles (Z. Zhao, 2023). Other anode materials, including alloy-type systems such as silicon and tin and a range of metal oxides, can offer higher capacity or enhanced electrochemical performance. However, these materials typically experience significant volume changes, pulverization, and limited electronic conductivity during cycling, which compromise their stability (Koech et al., 2024).

The initial phase of this research focused on the selection of suitable lithium-ion battery chemistries for comparative analysis. Four commercially established cathode materials, Nickel Cobalt Aluminium Oxide (NCA), Nickel Manganese Cobalt Oxide (NMC), Lithium Iron Phosphate (LFP), and Lithium Manganese Oxide (LMO), were selected because they represent technologically mature and widely deployed systems in modern lithium-ion batteries. These chemistries were chosen due to their distinctly different electrochemical and thermal characteristics, which provide a robust basis for evaluating performance, safety, and degradation mechanisms under diverse operating conditions. Collectively, these four cell chemistries account for more than 90 percent of global lithium-ion cell production for traction and stationary energy storage applications (Assi & Amer, 2025). In addition, they span a wide range of specific energy, approximately 100 to 260 Wh kg^{-1}, and cycle life, approximately 500 to 7000 cycles, thereby providing a representative and comprehensive dataset for comparative electro-thermal modelling and thermal behaviour analysis (M. K. Tran, Dacosta, et al., 2021; Walvekar et al., 2022).

NCA provides high specific energy of up to 260 Wh/kg and strong power capability, which makes it a reference material for high performance lithium-ion cells. However, its reduced thermal stability and relatively high cost, mainly driven by the high content of cobalt and nickel, remain important limitations (X. Chen et al., 2025; Velev et al., 2024). NMC offers a balanced compromise between energy density in the range of 180 to 220 Wh/kg, safety, and cost, and typically achieves 1000 to 2000 charge discharge cycles. Its degradation behaviour is strongly influenced by the nickel to manganese ratio and the applied current rate (Assi & Amer, 2025; Torregrosa et al., 2024). LFP is characterised by excellent thermal and chemical stability, long cycle life in the range of 3000 to 7000 cycles, and enhanced safety due to the absence of nickel and cobalt. Although its specific energy of 120 to 160 Wh/kg is lower than that of nickel rich chemistries, its structural robustness makes it highly suitable for applications that prioritise safety and durability (Walvekar et al., 2022). Lithium manganese oxide (LMO) provides high power capability, with a typical specific energy of approximately 120 Wh/kg, low material cost, and good thermal stability. However, it suffers from reduced cycle life, typically less than or equal to 1000 cycles, which is mainly associated with manganese dissolution and structural degradation under elevated operating temperatures (Lu et al., 2023; M. K. Tran, Dacosta, et al., 2021).

Figure 3 summarizes the key performance metrics of these chemistries, enabling evaluation of trade-offs among energy density, cycle life, safety, and cost, which are critical for battery design, thermal management, and application specific optimization.

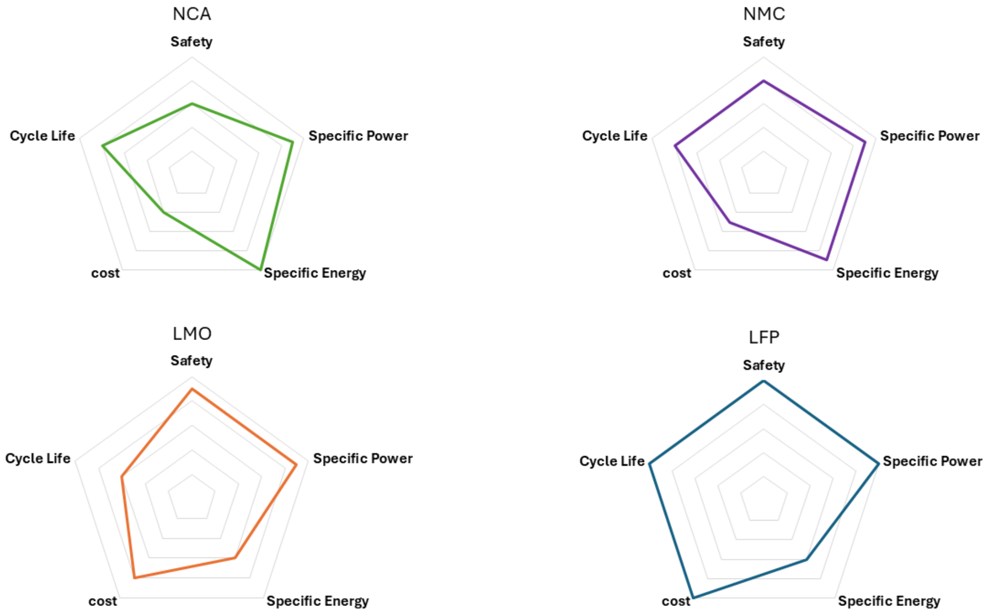

Figure 3 Illustrating the Key Performance Characteristics of Four Lithium-ion Battery Chemistries: NCA, NMC, LFP and LMO. Each radar plot compares Safety, Specific Power, Specific Energy, Cost and Cycle Life (Walvekar et al., 2022).

1.1.4 Thermal Runaway in Lithium-ion Batteries

The cathode in a lithium-ion battery is typically composed of lithium transition metal oxides or phosphates with a high redox potential, which determines the operating voltage of the cell and contributes to its energy capacity. The anode consists of materials with a low redox potential and stable electrochemical behaviour, enabling reversible lithium intercalation and long term cycling stability. The separator and electrolyte are critical components that strongly influence the overall performance of lithium-ion batteries. Their physicochemical properties affect ionic conductivity, thermal stability, cycle life, and capacity retention. The separator provides electrical insulation between the electrodes while allowing lithium-ion migration, and the electrolyte facilitates efficient ion transport between the electrodes during operation.

Figure 4 illustrates the causes of thermal runaway in lithium-ion batteries, which can be triggered by three types of abuse: mechanical, electrical, and thermal. Mechanical abuse includes crushing, impacts, or puncturing; electrical abuse involves overcharging, deep discharging, or short circuits; and thermal abuse results from high temperatures or exposure to fire. These conditions can damage the separator, leading to an internal short circuit (ISC), which generates excessive heat. This heat can accelerate chemical side reactions, release flammable gases, increase internal pressure, and eventually cause fire or explosion. The presence of flammable liquid electrolytes further increases this risk. Using solid-state electrolytes is one possible solution to improve battery safety.

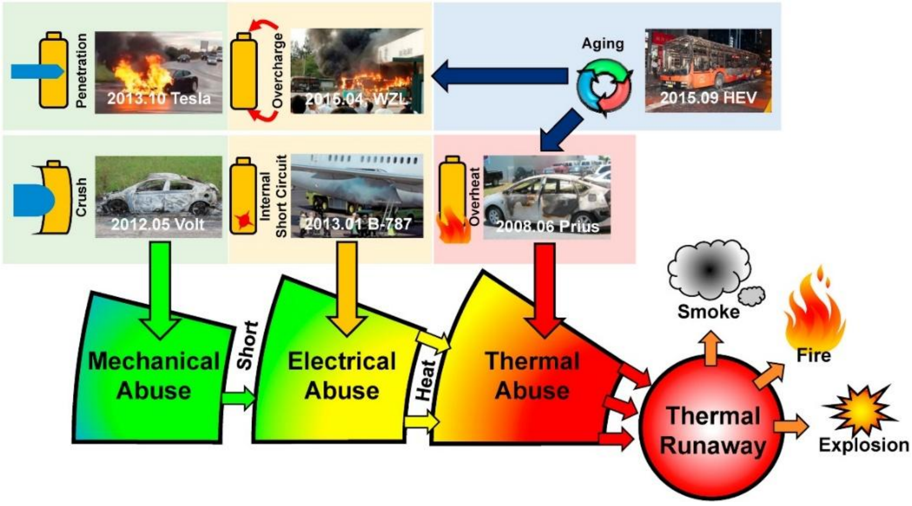

Figure 4 Factors Leading to Thermal Runaway in Lithium-ion Batteries (X. Feng et al., 2018)

The thermal runaway process is often described by three characteristic temperatures. T_1 is the temperature where self-heating begins, usually due to decomposition of the solid electrolyte interphase (SEI). T_2 is the temperature at which thermal runaway is triggered, often caused by separator failure and internal short circuit. At this point, the temperature rise becomes rapid. T_3 is the highest temperature reached during the process. Some thermal models focus on the entire process from T_1 to T_3, while others simulate only part of the response, such as from T_2 to T_3 (M.-K. Tran et al., 2022). Figure 5 illustrates these stages and highlights the sequence of thermal and electrochemical reactions leading to thermal runaway in lithium-ion batteries.

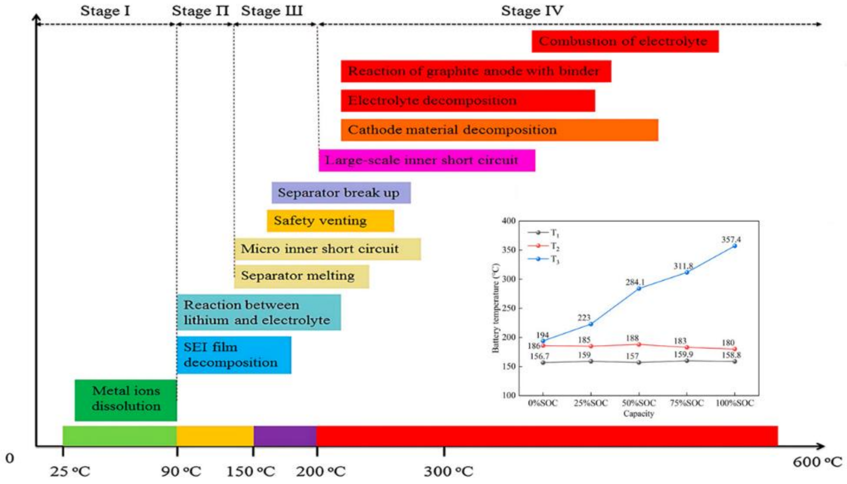

Figure 5 Runaway Mechanism and Critical Temperature Ranges for lithium-ion Batteries (H. Li et al., 2019; Qi et al., 2025).

1.2 Battery Thermal Management Systems (BTMS)

As electric vehicles (EVs) continue to evolve, manufacturers adopt different strategies in battery design and configuration to meet growing demands for performance and driving range. With the increasing capacity of EV batteries, the need for efficient thermal management becomes even more important. According to the Global EV Outlook Report (IEA, 2020), battery electric vehicles (BEVs) are expected to achieve average driving ranges of 350 to 400 km by 2030, supported by battery capacities of approximately 70-80 kWh. These advances bring batteries closer to the performance range of conventional fuel-powered vehicles (He, 2024). However, as battery size and power increase, so does the importance of integrating advanced battery thermal management systems (BTMSs). These systems play a key role in ensuring battery safety, extending lifespan, and maintaining consistent performance under various operating conditions. As the industry shifts toward more sustainable transportation solutions, the implementation of reliable and efficient BTMS becomes essential in supporting the next generation of EV technologies.

Lithium-ion batteries (LIBs), which are widely used in EVs, are sensitive to both high and low operating temperatures, as well as to temperature inconsistencies within the battery pack. The primary goal of a BTMS is to keep the entire battery within a safe and efficient temperature range during operation and charging. However, thermal performance is not the only consideration. A practical BTMS must also be lightweight, scalable, energy-efficient, and compatible with other components within the battery pack. It is generally recommended that the BTMS should not exceed 20% of the total battery pack weight, and it should not interfere with critical elements such as wires, busbars, or structural components (Olabi et al., 2022).

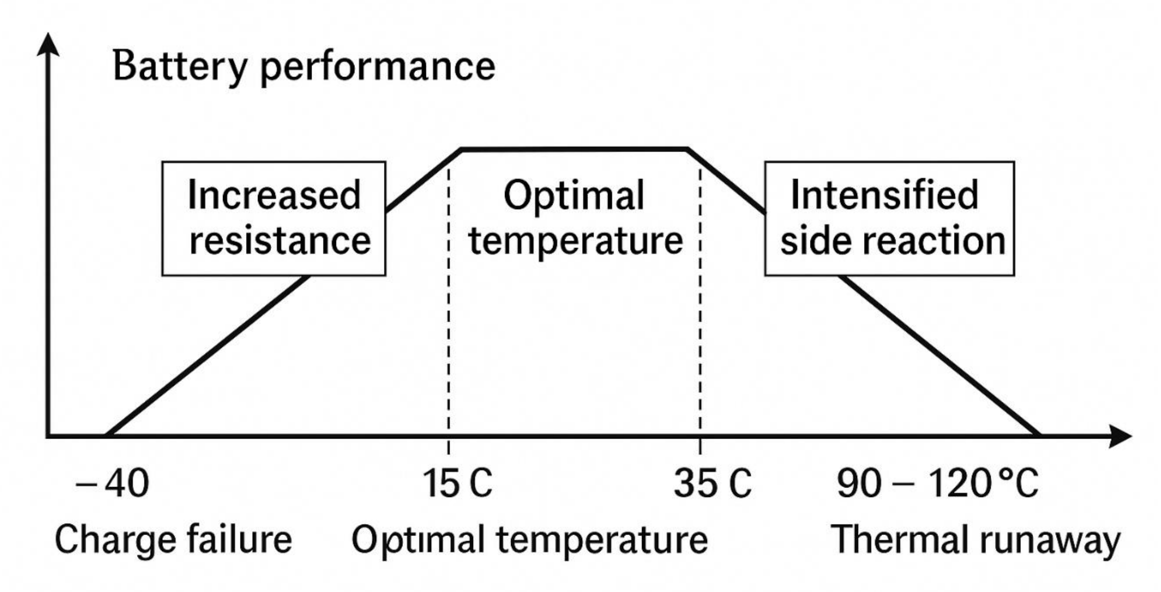

Figure 6 Temperature window ensuring optimal LIB efficiency (Ianniciello et al., 2018)

In terms of thermal targets, effective cooling strategies aim to maintain the maximum battery temperature (T_{max}) below 40°C, and preferably under 35°C, while ensuring that the minimum temperature (T_{min}) remains above 15°C during colder conditions. To promote uniform performance and reduce degradation, the temperature variation within the battery pack (ΔT) should be kept under 5°C.

BTMS technologies can be categorized in several ways, including active or passive systems, heating or cooling approaches, and by the type of cooling method used such as air, liquid, phase change materials (PCM), or heat pipes (HP). Active systems, which use fans or pumps to drive cooling, are common in liquid and air-based designs and are known for their high efficiency, though they add system complexity. In contrast, passive systems use PCMs or HPs to dissipate heat without the need for external power. PCM-based systems are particularly useful for improving temperature uniformity, while HPs are valued for their fast response and high thermal conductivity (Olabi et al., 2022).

An overview of different cooling methods is presented in Figure 7, and will be explored in more detail below.

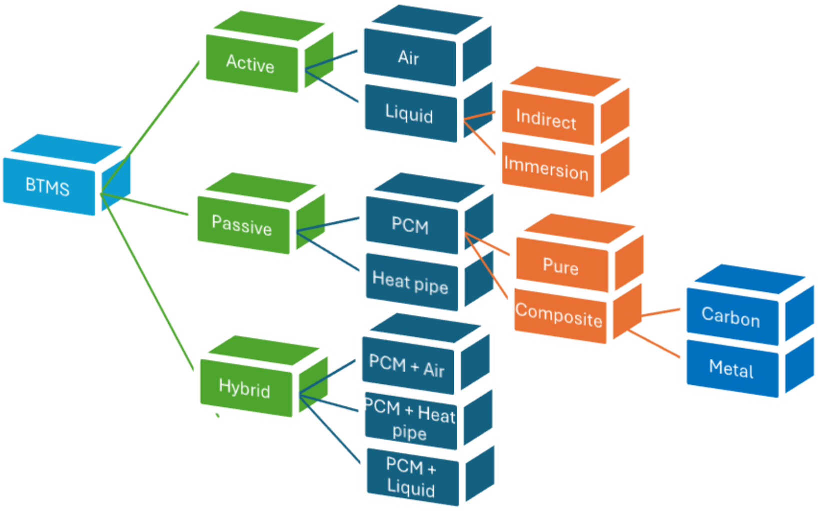

Figure 7 Categories of Battery Thermal Management Systems (Olabi et al., 2022)

1.2.1 Active Cooling

Active cooling methods are essential in battery thermal management systems (BTMS), particularly for applications involving high power demands such as fast charging, steep accelerations, or prolonged operation. These systems employ external mechanisms to drive a working fluid, typically air or liquid, to effectively dissipate the heat generated during battery operation. By offering enhanced thermal regulation and precise temperature control, active cooling helps maintain battery safety, efficiency, and lifespan (Z. Zhao et al., 2021). The two most common active cooling strategies are air-based and liquid-based systems, which are discussed in detail below.

1.2.1.1 Air Cooling

Air-based cooling systems are widely adopted in BTMS due to their simplicity, reliability, cost-effectiveness, and safety. Air, being abundant and having excellent dielectric properties, eliminates the need for electrical isolation between coolant and battery cells. This allows for flexible integration with various cell geometries and simplifies battery-swapping designs by removing the need for liquid coolants.

Air BTMS typically employs blowers or air conditioning units to regulate battery temperature. Forced air convection provides higher heat rejection compared to natural convection, but it may generate additional noise and require larger ducts and blowers, increasing the system's size, weight, and parasitic power consumption, which may offset its inherent advantages (Basu et al., 2016).

Recent studies have focused on improving air cooling performance by optimizing cell layout, airflow paths, or combining air cooling with other thermal strategies (Basu et al., 2016). Among these, cell arrangement plays a crucial role. Poor layout can restrict airflow, trap heat, and create thermal hotspots, posing safety and performance risks during EV operation (Yang et al., 2015).

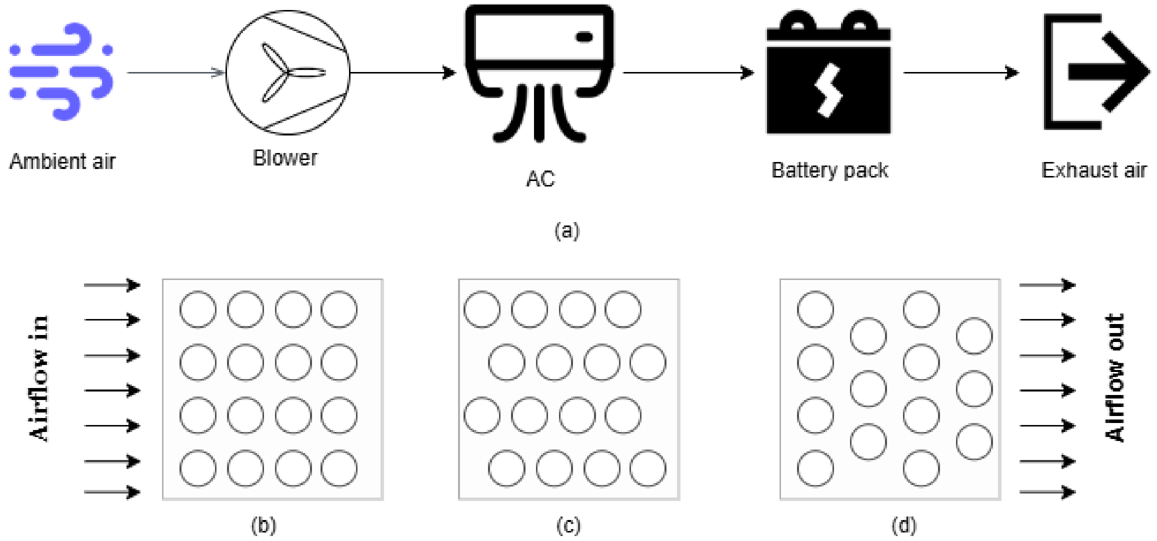

Figure 8 Schematic diagram of (a) an air-based battery cooling system, and cell arrangement configurations: (b) aligned, (c) staggered, and (d) cross (He, 2024)

It is also important to highlight an additional configuration of the air cooling system. In terms of airflow direction, various path configurations have been proposed and can be mainly categorized into three types: U-type, Z-type, and other novel designs, as illustrated in Figure 9. The U-type and Z-type represent conventional layouts. In the U-type battery pack, where both the inlet and outlet are located on the same side, cooling air enters through the lower duct, passes through the channels between adjacent battery cooling plates, and exits as heated air from the upper vent via the outlet. In contrast, the Z-type battery pack positions the inlet and outlet on opposite sides (He, 2024). Since the outlet is fixed in these conventional designs, (Y. Liu & Zhang, 2019) proposed a novel J-type airflow configuration incorporating two outlets controlled by valves to improve cooling flexibility.

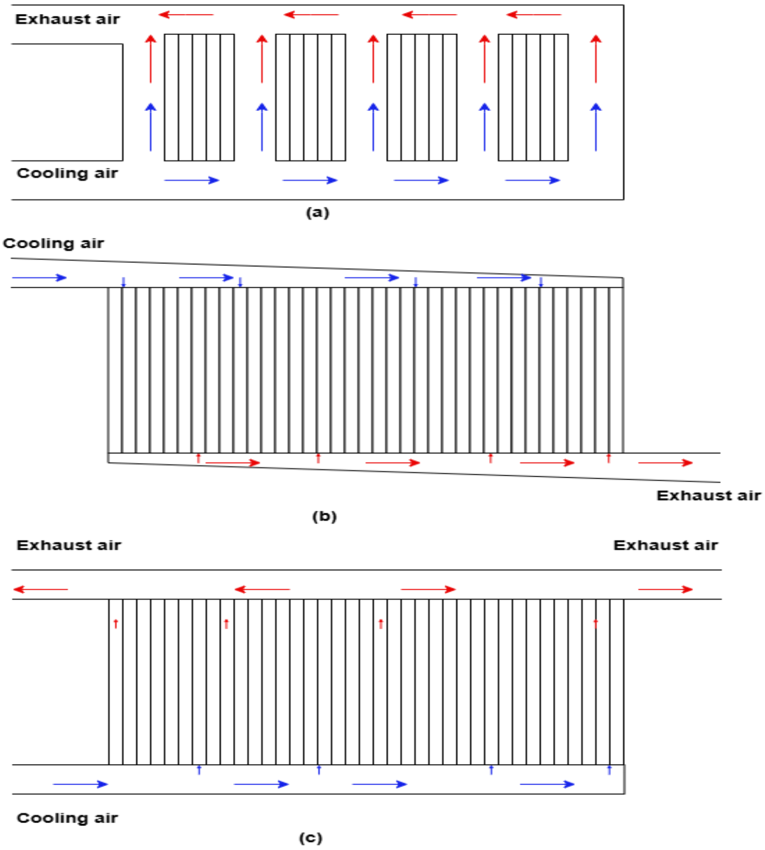

Figure 9 (a) U-type, (b) Z-type, and (c) J-type BTMS configurations (He, 2024).

1.2.1.2 Liquid Cooling

Liquid cooling is one of the most effective thermal management methods for lithium-ion battery systems, and it can be categorized into two main types: indirect cooling and direct cooling (also referred to as immersion cooling), depending on whether the coolant comes into direct contact with the battery components.

In indirect liquid cooling, the coolant circulates through components such as cooling plates (E et al., 2018), discrete tubes (Xia et al., 2017), or cooling jackets (Sheng et al., 2021) placed in contact with the outer surfaces of the battery cells. This method allows the heat generated by the battery to be transferred away without the coolant directly touching the cells, thereby reducing the risk of electrical hazards (Thakur et al., 2020).

On the other hand, direct liquid cooling involves full contact between the coolant and the battery. This requires the use of non-conductive fluids to prevent short circuits. The key advantage of this method is the significantly improved thermal contact area, resulting in a much higher heat transfer rate. Direct liquid cooling can be further divided into single-phase and two-phase systems, based on whether the coolant undergoes a phase change during heat absorption. Compared to indirect systems, direct liquid cooling generally provides better thermal regulation and more uniform temperature distribution across the battery pack. The direct contact between the battery and coolant also allows for simpler flow path designs and reduces the complexity of sealing systems, thereby lowering the risk of coolant leakage and subsequent failures. Despite these advantages, direct liquid cooling is not yet widely implemented in commercial electric vehicles due to challenges such as fluid selection, cost, and safety considerations (J. Liu et al., 2023).

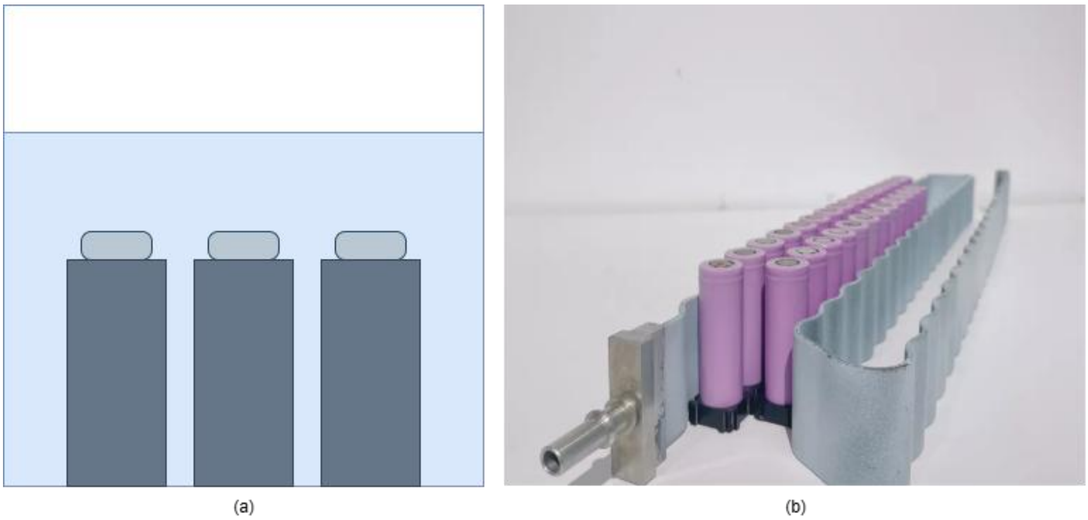

Figure 10 Schematic Illustration of (a) Direct and (b) Indirect (Trumony, 2025) Liquid Cooling Methods for Battery Packs

1.2.2 Passive Cooling

Passive cooling strategies in Battery Thermal Management Systems (BTMS) have gained traction due to their ability to regulate battery temperature without relying on external energy input or complex mechanical components (Siddique et al., 2018). These systems capitalize on the inherent properties of materials and physical phenomena, such as latent heat absorption, to dissipate heat. Compared to active systems, passive methods offer advantages such as reduced weight, improved reliability, and lower parasitic power consumption, making them especially suitable for compact or cost-sensitive applications (Nicholls et al., 2024). Among the most widely studied passive approaches are phase change materials (PCMs) and heat pipes (HPs), both of which have shown promise in maintaining temperature stability and improving battery safety (Sharifi et al., 2024). The following sections explore the mechanisms, classifications, and performance characteristics of these passive cooling technologies in detail.

1.2.2.1 Phase Change Materials (PCM)

PCMs have recently gained attention as a promising solution for managing the thermal behavior of lithium-ion batteries. Compared to conventional air or liquid cooling methods, PCMs offer distinct advantages, primarily due to their ability to absorb and store significant amounts of heat via latent heat during phase transitions between solid and liquid states. Figure 11 illustrates this thermal response, highlighting the isothermal segment that corresponds to the phase change process. When the battery temperature rises near the PCM's melting point, the material begins to melt and absorbs heat, effectively maintaining a stable temperature close to the phase change temperature. By carefully selecting a PCM with an appropriate melting point, the battery can be kept within its optimal operating temperature range. During this melting process, the PCM continues to absorb heat without a significant increase in temperature until the phase change is complete. Unlike traditional materials that rely on sensible heat storage, PCMs utilize latent heat, which enables a much higher heat storage capacity in a compact and lightweight form. PCM-based cooling systems are entirely passive, requiring no fans, pumps, or external power sources. This passive nature not only reduces system complexity and maintenance needs but also enhances reliability.

Additionally, PCMs can help suppress thermal runaway events by passively absorbing excess heat generated during uncontrolled exothermic reactions, potentially preventing dangerous temperature spikes (Nasiri & Hadim, 2025).

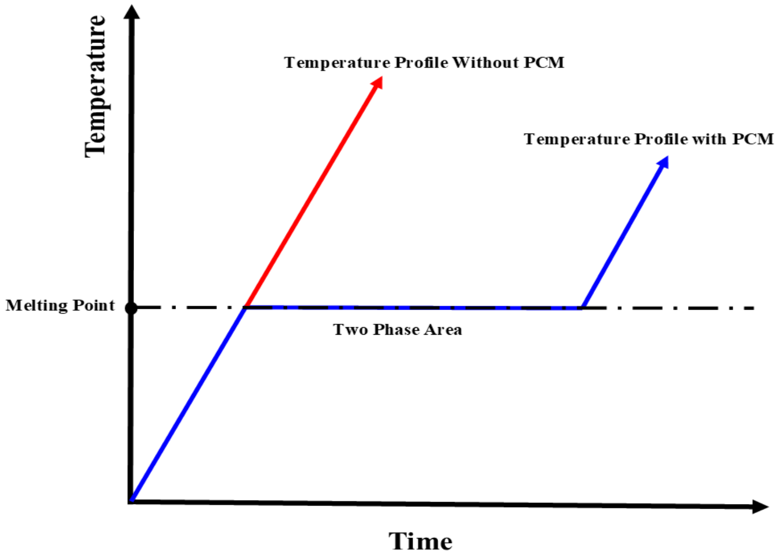

Figure 11 Temperature vs. Time profile of a Phase Change Material (PCM) during heating

However, one of the main limitations of PCMs is their inherently low thermal conductivity, which slows both the rate of heat absorption from the battery and the rate of heat dissipation to the environment. This can reduce the effectiveness of PCM-based systems, especially in applications with high heat loads or rapid charge/discharge cycles. As a result, improving the thermal conductivity of PCMs through material enhancement strategies has become a key area of research in battery thermal management (Dong et al., 2023).

One way to classify PCMs is by the type of phase transition they undergo. These include solid-solid (SSPCMs), solid-liquid (SLPCMs), solid-gas (SGPCMs), and liquid-gas (LGPCMs) transitions (Maknikar & Pawar, 2023; Pielichowska & Pielichowski, 2014; W. Wu et al., 2020). Among these, solid-liquid PCMs (SLPCMs) are the most used in battery thermal management systems because they offer a high capacity for storing thermal energy and experience only minimal volume change during melting and solidifying (W. Wu et al., 2020). However, one drawback is that they can leak when in liquid state. To address this, researchers often add materials known as functional fillers to stabilize the structure and improve heat transfer (Zhi et al., 2022). In contrast, solid-solid PCMs (SSPCMs) avoid the leakage issue entirely because they do not melt. Instead, they change their internal crystal structure during phase transition. This makes them a stable and clean option, especially in applications where dimensional stability and cleanliness are essential (Zeng et al., 2024).

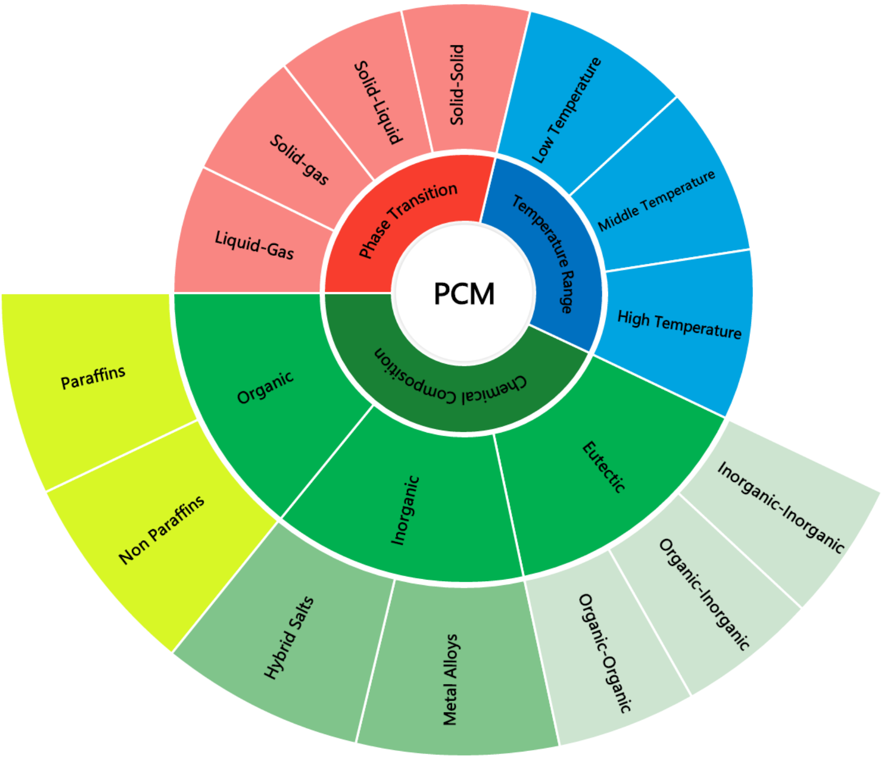

Figure 12 Classification of Phase Change Materials (PCMs)

The second classification is based on chemical composition, dividing PCMs into organic, inorganic, and eutectic types. Organic PCMs are preferred in many applications due to their stability, non-corrosiveness, and relatively high latent heat capacity. They include paraffin hydrocarbons whose properties improve with longer carbon chains. However, increasing the chain length also elevates the melting point, which may be unfavorable for battery thermal management applications. Non-paraffins such as fatty acids, esters, alcohols, and polyethylene glycols (PEGs) offer alternative phase-change options, providing a wider range of melting temperatures and improved tunability for specific thermal management requirements (Ianniciello et al., 2018). Despite their benefits, organic PCMs suffer from low thermal conductivity, flammability, and potential leakage during the melting phase, all of which can increase thermal resistance and safety risks in BTMS (Cai et al., 2023; C. Liu et al., 2020; Zhi et al., 2022). Inorganic PCMs, such as hydrated salts and metal alloys, offer better thermal conductivity and latent heat values across a broad temperature range (−100 °C to +1000 °C), but they face issues like supercooling, corrosion, and phase separation

(Avik, 2024). Hydrated salts like $CaCl_2{\cdot}6H_2O$ and $MgCl_2{\cdot}6H_2O$ are among the most researched for PCM applications. Metal-based PCMs, though highly conductive, are dense, expensive, corrosive and less practical for large-scale systems (Ianniciello et al., 2018). Eutectic PCMs, which are mixtures of two or more pure materials, exhibit congruent melting and solidification behavior at a fixed temperature, often lower than the components themselves (Milián et al., 2017). These can be categorized into organic–organic, inorganic–inorganic, and organic–inorganic eutectics (Baetens et al., 2010; Zhi et al., 2022). While eutectic PCMs offer enhanced thermal reliability and tunable melting points, their thermal conductivity and long-term performance remain underexplored (C. Liu et al., 2020; Nazir et al., 2019).

Lastly, PCMs are classified by temperature range, which is critical for selecting the appropriate material for BTMS applications. One classification approach groups PCMs into low-temperature (<220 °C), medium-temperature (220–420 °C), and high-temperature (>420 °C) categories (Alehosseini & Jafari, 2020). A more BTMS-relevant classification proposed by Cai et al., 2023) defines low-temperature PCMs as those melting below 100 °C, medium-temperature PCMs between 100 and 300 °C, and high-temperature PCMs above 300 °C. For lithium-ion battery systems, PCMs with melting points between 20 and 50 °C are recommended, as they help maintain operating temperatures below the safety threshold of 50 °C (Rao et al., 2011). Organic PCMs are suited for low-temperature conditions, while inorganic PCMs are more suitable for high-temperature thermal storage (Y. Zhao et al., 2022).

1.2.2.2 Heat Pipes

Heat pipes (HPs) have become a popular solution for temperature regulation across many residential and commercial applications, largely because of their exceptional heat transfer abilities. Often called "thermal superconductors", HPs can conduct heat up to ninety times more efficiently than a copper rod of the same size. This property allows them to maintain a nearly uniform temperature at the evaporator surface. Their adaptable geometry also makes them suitable for integration into various spatial configurations. As a result, HPs are increasingly viewed as an effective option for cooling and temperature control in hybrid and electric vehicle (HEV/EV) battery systems (Afzal et al., 2023).

At their core, heat pipes operate using a two-phase heat transfer mechanism, which allows them to move substantial amounts of thermal energy with minimal temperature differences. This phase-change process provides a significantly higher effective heat transfer coefficient compared to conventional single-phase systems. Additionally, HPs do not require any auxiliary coolant-circulation system, which reduces system complexity and energy consumption (Tardy & Sami, 2009; Xiao & Faghri, 2008).

As illustrated in Figure 13, a heat pipe typically consists of a closed metal tube divided into three sections: the evaporator, the adiabatic zone, and the condenser. Inside this sealed structure, a working fluid exists in both liquid and vapor phases. When heat is applied to the evaporator, the fluid absorbs this energy and vaporizes. The resulting vapor travels to the condenser, where it releases its latent heat and returns to a liquid state. This extracted heat is usually removed through a cooling loop, commonly air or water based. Finally, the liquid flows back to the evaporator section through a wick structure via capillary action. Thanks to their high thermal efficiency, passive operation, and design flexibility, heat pipes present a highly promising approach for future battery thermal management systems (Afzal et al., 2023).

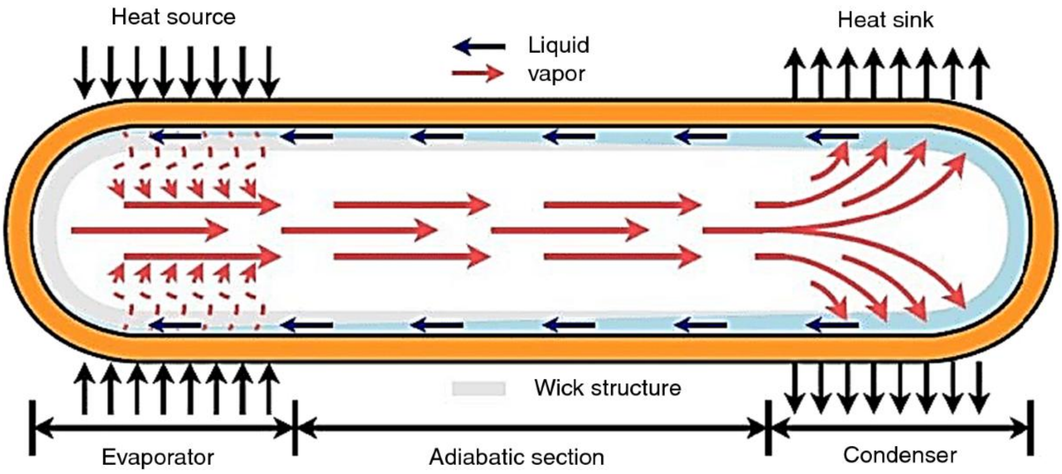

Figure 13 Schematic of a heat pipe illustrating two-phase heat transfer via vapor flow and liquid return through the wick structure(Afzal et al., 2023).

1.2.3 Hybrid

Recently, hybrid cooling techniques that integrate passive and active cooling strategies have gained increasing attention to address the growing thermal management challenges in battery modules. These approaches are particularly relevant under extreme operating conditions such as high-speed driving, uphill movement, or fast charging, where the charging rate can reach 4C to 6C with power levels up to 400 kW, significantly exceeding the conventional 1.5–2.0C rates used in typical electric vehicles. A common hybrid configuration involves the combination of PCM cooling with forced air, liquid, or heat pipe systems. Figure 11 illustrates various hybrid cooling strategies used in battery thermal management. Such integration helps leverage the latent heat absorption of PCMs while enabling active heat removal to maintain acceptable temperature ranges. Studies have shown that PCM-liquid cooling systems can effectively control the maximum temperature during high-rate discharges, although maintaining uniform temperature distribution across the module remains a challenge. Temperature differences have often exceeded the ideal threshold of 5 °C, highlighting the need for further optimization in both system design and thermal uniformity. Moreover, hybrid systems generally introduce additional weight due to the inclusion of PCMs, pumps, fans, and heat sinks. Since increased weight directly affects vehicle energy efficiency, lightweight design should also be a key optimization objective alongside thermal performance parameters (X. Wu et al., 2020).

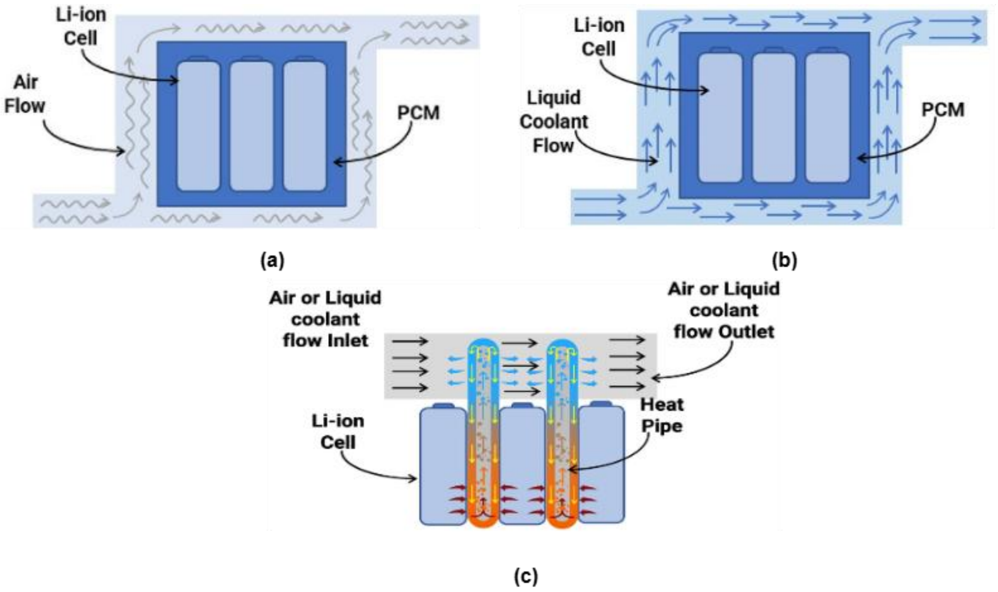

Figure 14 Basic layout of hybrid battery thermal management systems: (a) air–PCM, (b) liquid–PCM, and (c) heat pipe (Vikram et al., 2024) configurations.

1.3 LIB Modelling Approaches

To design efficient and safe battery systems, especially for electric vehicles (EVs), it is crucial to accurately model both the electrochemical and thermal behaviour of lithium-ion batteries. Battery modelling approaches are generally categorized into empirical, electrochemical, and data-driven models. Empirical models, such as equivalent circuit models (ECMs), are derived from experimental data and widely used in battery management systems (BMS) due to their simplicity and low computational demands. These models typically consist of combinations of resistors and capacitors to represent the dynamic electrical behaviour of the battery (M. K. Tran, Mathew, et al., 2021). In contrast, electrochemical models, including the Pseudo-2D (P2D) and Single Particle Model (SPM), provide deeper insight by solving partial differential equations based on ion transport, reaction kinetics, and spatial variations within the cell, offering a detailed understanding of the internal physical and chemical processes (S. Han et al., 2021). Although these models are powerful, they come with increased computational complexity. With the rise of artificial intelligence, data-driven models have emerged as a promising approach. These models use machine learning algorithms to predict battery behaviour and performance from large datasets, often without requiring explicit physical equations (Felix Omojola et al., 2024; Oh et al., 2024). Each of these modelling strategies has its advantages and limitations, and their selection depends on the specific application and required level of accuracy.

1.3.1 Electrochemical Modelling

This section focuses specifically on electrochemical modelling approaches, which describe lithium-ion battery behaviour using governing equations for ion transport, charge transfer, and thermodynamic processes. These models vary in their level of detail and computational requirements, ranging from microstructure-resolved heterogeneous models (Lu et al., 2020) to porous-electrode formulations such as the P2D framework (Doyle et al., 1993), as well as reduced-order representations including the Single Particle Model (Haran et al., 1998) and its variants. The following subsections provide an overview of these electrochemical modelling categories.

1.3.1.1 Heterogeneous Models

The heterogeneous model provides a detailed and spatially resolved approach to simulating the behaviour of lithium-ion batteries by reconstructing the actual three-dimensional (3D) microstructure of the electrodes and electrolyte phases. This is achieved using advanced imaging techniques such as X-ray micro-computed tomography, which enables accurate modelling of the solid and pore domains without requiring volume-averaged parameters such as porosity or average particle size (Lu et al., 2020).

Unlike conventional volume-averaged models, the heterogeneous model incorporates explicit geometrical features and boundary conditions at the particle scale. This allows for a high-resolution analysis of spatial variations in lithium concentration, current density distribution, and local temperature gradients within the electrode. Such detail is particularly important for analysing performance during high-rate charge/discharge cycles and for investigating degradation phenomena at the microstructural level (Fang et al., 2020; Lu et al., 2020).

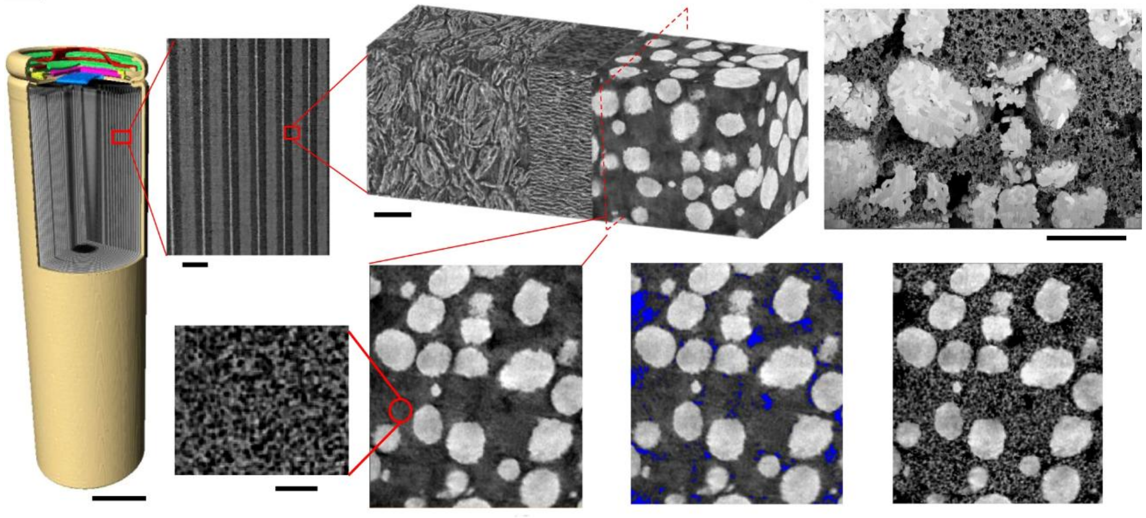

Figure 15 Reconstructed 3D Volume of the Electrode Showing Distinct Phases in Greyscale: White Represents NMC Active Material, Dark Grey Indicates the Carbon-Binder Domain, and Black Corresponds to the Pore Space (Lu et al., 2020).

Additionally, the model facilitates the evaluation of mechanical stresses that develop during electrochemical cycling. These stresses originate from the non-uniform expansion and contraction of active materials due to inhomogeneous lithiation, which may lead to cracking, delamination, or separator deformation. This, in turn, affects both the mechanical integrity and safety of the cell (Fang et al., 2020).

Despite its advantages, the application of heterogeneous modelling in practical battery design remains limited by several challenges. High computational demands and the need for high-resolution tomographic data can restrict scalability. Moreover, limitations in imaging resolution and possible distortions during image acquisition may affect the model's accuracy.

Certain interfacial features such as contact resistance between the current collector and the electrode coating also remain difficult to capture with current imaging techniques (Fang et al., 2020).

1.3.1.2 Pseudo-2D (P2D) Models

The Pseudo-Two-Dimensional (P2D) model, originally developed by Doyle, Fuller, and Newman based on concentrated solution theory, is widely regarded as one of the most accurate and detailed electrochemical models for describing the behaviour of porous electrode lithium-ion batteries (Doyle et al., 1993). This model has been successfully validated across various lithium chemistries, including lithium iron phosphate (LFP), lithium cobalt oxide (LCO), lithium nickel cobalt aluminium oxide (NCA), and lithium nickel manganese cobalt oxide (NMC) (Haosong He, 2024).

The P2D model operates under two core assumptions: (1) the active material in the electrode is composed of spherical particles, with lithium transport governed by solid-state diffusion; and (2) the electrical conductivity of the current collectors is sufficiently high to neglect variations along the transverse directions (y and z), allowing the model to focus on one-dimensional (x-direction) dynamics for reaction and transport processes. As illustrated in Figure 16, the model divides the battery cell into three primary domains: the negative electrode, the electrolyte (separator), and the positive electrode. During discharge, lithium ions de-intercalate from the solid phase in the negative porous electrode, migrate through the electrolyte, and intercalate into the solid phase of the positive porous electrode. This process reverses during charging (Kemper et al., 2015).

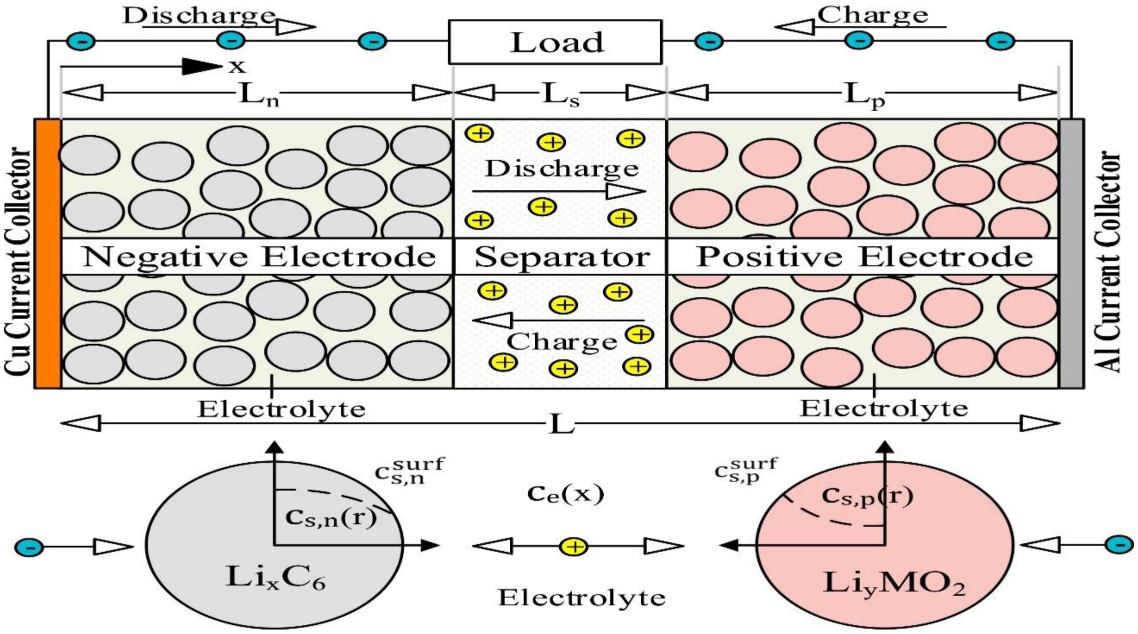

Figure 16 Pseudo-Two-Dimensional Model During the Charge and Discharge Process (Al-Gabalawy et al., 2020).

Despite its high accuracy, the full-order P2D model involves many nonlinear partial differential equations (PDEs), which require numerical solutions due to the lack of analytical ones, resulting in high computational costs (S. Han et al., 2021). This makes it impractical for simulating thermal and electrochemical behaviour under varying duty cycles in real-time applications, particularly in battery thermal management system (BTMS) design for electric vehicles (EVs) (Cheng, 2019). Although some studies have developed reduced-order P2D models to improve computational efficiency (C. Li et al., 2021)(Li et al., 2021), the inclusion of detailed internal phenomena such as current distribution often adds limited value for thermal analysis at the module level (Kantharaj & Marconnet, 2019). As a result, the P2D model may be considered overly complex for large-scale thermal modelling in EV applications.

1.3.1.3 Single Particle Models (SPM)

To reduce the complexity of the P2D model, (Haran et al., 1998 proposed the single particle model (SPM), which assumes that each electrode in a cell can be represented by a single, uniformly sized spherical particle (see Figure 17). This simplification is valid under the condition of uniform current distribution across both electrodes. The model neglects spatial variations in concentration and potential within the electrolyte phase, replacing them with a lumped solution resistance term. Consequently, the electrolyte phase is excluded from the model, and lithium concentration within the solid phase is described using a second-order polynomial. This approach significantly improves computational efficiency while maintaining acceptable accuracy under 1C operating conditions. To enhance the model's realism, Guo et al., 2011 incorporated temperature dependence into the original SPM. Their results showed strong agreement with experimental voltage data for lithium-ion pouch cells discharged at rates of 0.03C, 0.5C, and 1C across a temperature range of 15 °C to 45 °C.

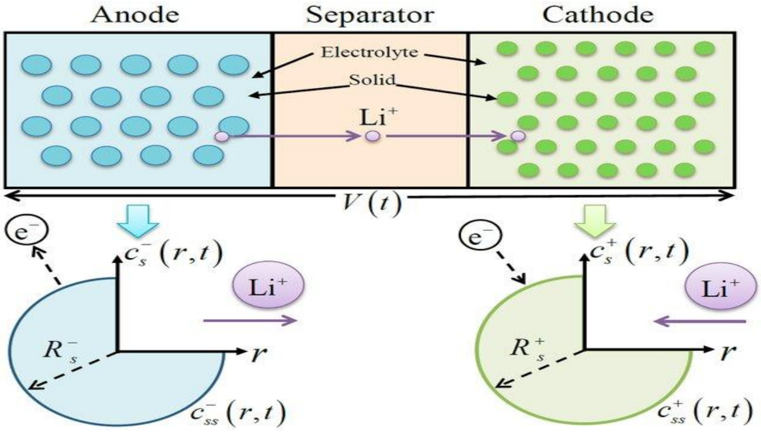

Figure 17 Simplified Concept of the Single Particle Model (SPM), Representing Each Electrode as a Single Spherical Particle (Zhang et al., 2020).

However, the assumptions of the SPM break down at high C-rates (i.e., >1C), where concentration gradients in the electrolyte phase become significant (Guo et al., 2011). This leads to over 10% error in voltage predictions and a comparable discrepancy in heat generation estimation (Khaleghi Rahimian et al., 2013). Consequently, the SPM becomes inadequate for accurate heat generation prediction under full-range EV operating conditions, limiting its suitability for BTMS design.

1.3.1.4 Lumped Single Particle Models

To address the limitations of the SPM at higher C-rates, (Ekström et al., 2018) introduced the Lumped Single Particle Model (LSPM), which simplifies the SPM by assuming that only one electrode contributes significantly to diffusion-related voltage losses. This approach reduces model complexity, lowering the number of required parameters to approximately 10, compared to 22 and 40 for the SPM and P2D models, respectively. The LSPM improves accuracy under >1C conditions by fitting three key electrochemical parameters ohmic overpotential at 1C ($\eta_{ohm,1c}$), dimensionless charge exchange current (J_o), and diffusion time constant (τ) to experimental data using the Levenberg–Marquardt algorithm (Ekström et al., 2018). The non-destructive nature of the data acquisition process makes the model suitable for EV applications (Ng et al., 2020). Voltage prediction errors remained within 12 mV under dynamic drive cycles up to ±10C (Ekström et al., 2018), and under low C-rates (e.g., 0.3C), discrepancies were less than 7 mV (Ng et al., 2020). These benefits have led to increasing adoption of LSPM in thermal modelling studies.

1.3.2 Equivalent Circuits Models (ECM)

The Equivalent Circuit Model (ECM) is an empirical model developed based on experimental data. It typically consists of a series resistor and one or more parallel resistor-capacitor (RC) networks, as shown in Figure 18 The resistor R_0 represents the internal ohmic resistance of the battery cell, while the RC networks capture dynamic electrochemical phenomena such as double-layer capacitance, charge transfer, and mass transport effects (Ding et al., 2019). Due to its simplicity and low computational demand, the ECM is widely employed in battery management systems (BMS) for estimating the state of charge (SOC) and state of health (SOH) (M. K. Tran, Mathew, et al., 2021). However, unlike physics-based electrochemical models, the ECM provides no direct insights into the internal physicochemical processes of the cell. Its parameters (e.g., resistors and capacitors) are generally extracted using hybrid pulse power characterization (HPPC) tests under isothermal conditions at varying SOC levels. In practice, however, electric vehicle (EV) batteries operate across a broad temperature spectrum, limiting the ECM's effectiveness in predicting thermal behaviour for battery thermal management system (BTMS) applications (M. K. Tran, Mathew, et al., 2021). Furthermore, achieving high accuracy with ECM requires extensive datasets, which becomes particularly challenging for aging studies, where parameter recalibration is frequently needed to reflect the evolving battery characteristics (Teliz et al., 2022).

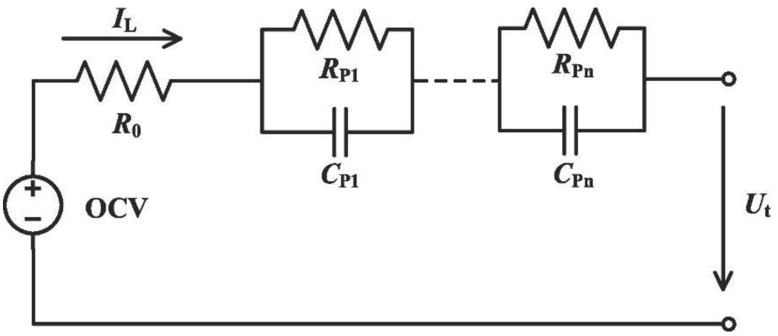

Figure 18 Schematic of an Equivalent Circuit Model (ECM) with multiple RC parallel networks (n-RC)(Ding et al., 2019)

1.3.3 Machine Learning

Artificial intelligence (AI) has emerged as a powerful approach for modelling and simulating lithium-ion batteries, offering high prediction accuracy and reduced computational cost compared to traditional physics-based models. AI-driven techniques, particularly those based on machine learning (ML), can learn complex relationships from large datasets, enabling accurate predictions of state of charge (SOC), state of health (SOH), voltage response, internal temperature, and capacity degradation without requiring detailed electrochemical equations. Models such as artificial neural networks (ANNs), support vector machines (SVMs), and deep learning architectures have been successfully applied to forecast battery behaviour under diverse operational conditions. These data-driven methods are especially beneficial for real-time implementation in battery management systems (BMS), where they facilitate fast decision-making to enhance battery safety, efficiency, and lifespan. Furthermore, hybrid approaches that integrate physics-based understanding with AI techniques, known as physics-informed machine learning, are gaining attention for combining interpretability with predictive performance. Thus, AI modelling presents a promising path for advancing battery simulation, particularly when conventional modelling is limited by computational burden or incomplete knowledge of material parameters (Felix Omojola et al., 2024).

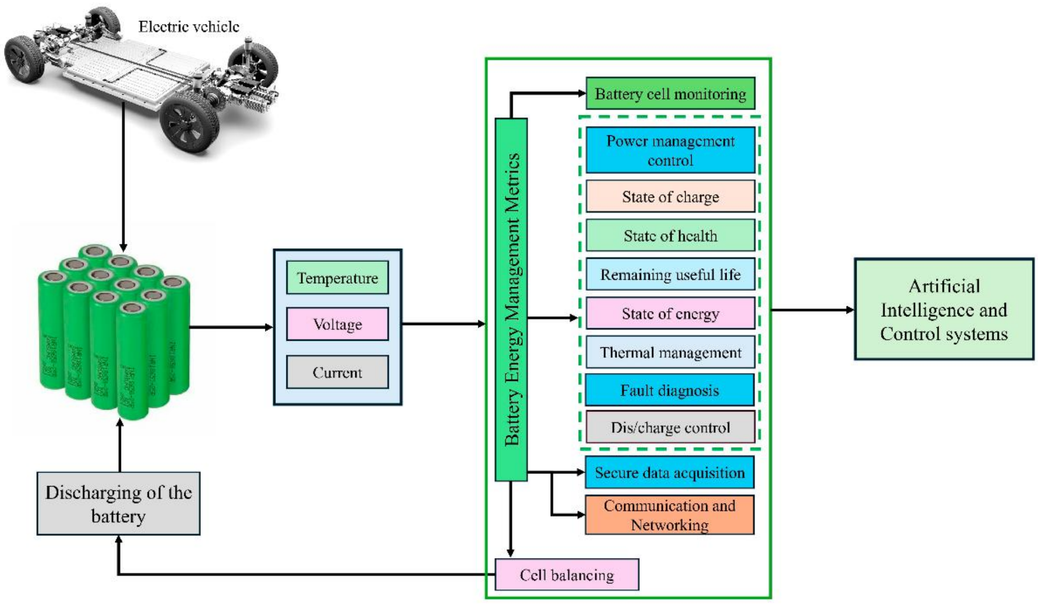

Figure 19 Battery Energy Management and Control Framework for EV Applications (Cavus et al., 2025).

2 Thermal Modelling

Battery modelling approaches can be applied at different levels of abstraction, ranging from module and pack configurations down to the electrochemical processes within a single cell. Since the thermal behaviour of the overall system originates from cell-level phenomena such as reaction kinetics, transport processes, and local heat generation, cell modelling provides the necessary foundation for accurate thermal simulations (Cheng, 2019; S. Han et al., 2021).

2.1 Cell Modelling

Within cell modelling, heat generation plays a central role because it directly links the electrochemical processes to the resulting thermal response. Understanding how reversible and irreversible sources of heat arise is therefore a prerequisite for predicting temperature evolution and designing effective thermal management strategies (Jindal et al., 2022; Nazari & Farhad, 2017).

2.1.1 Heat Generation in LIBs

The thermal response of lithium-ion batteries is a critical factor influencing their performance, safety, and lifespan. The heat generated inside a battery during operation originates from two primary sources: reversible and irreversible heat. The reversible heat is associated with the entropy change of the electrochemical reactions and can be either endothermic or exothermic, depending on the sign of the entropy coefficient ($\frac{\partial U_{ocv}}{\partial T}$), where U_{ocv} is the open-circuit voltage. It is given by:

$$Q_{rev} = \pm IT\frac{\partial U_{ocv}}{\partial T} \tag{1}$$

where I denotes the current, and T is the cell temperature (K). On the other hand, irreversible heat arises from ohmic losses and polarization effects within the cell, mainly due to internal resistance to ion and electron transport. The total irreversible heat generation can be represented as:

$$Q_{irr} = I^2R \tag{2}$$

where R denotes the total internal resistance of the cell (Ω). This includes ohmic, charge-transfer, and mass transport resistances, which collectively contribute to polarization as shown in Figure 20. Polarization leads to a voltage deviation from the equilibrium potential during operation, further increasing heat generation under high current loads(Nazari & Farhad, 2017). The total heat generation rate in the cell, often referred to as the Bernardi equation, combines these components:

$$Q_{total} = I(V - U_{ocv}) - IT\frac{\partial U_{ocv}}{\partial T} \tag{3}$$

Here, V is the terminal voltage (V) and U_{ocv} is open circuit voltage (V), which represents the equilibrium potential of the cell under no-load conditions. The first term represents polarization heat, while the second term captures entropy-related heat effects. This equation is widely used in thermal modelling of batteries, providing a reliable basis for designing BTMS (Jindal et al., 2022).

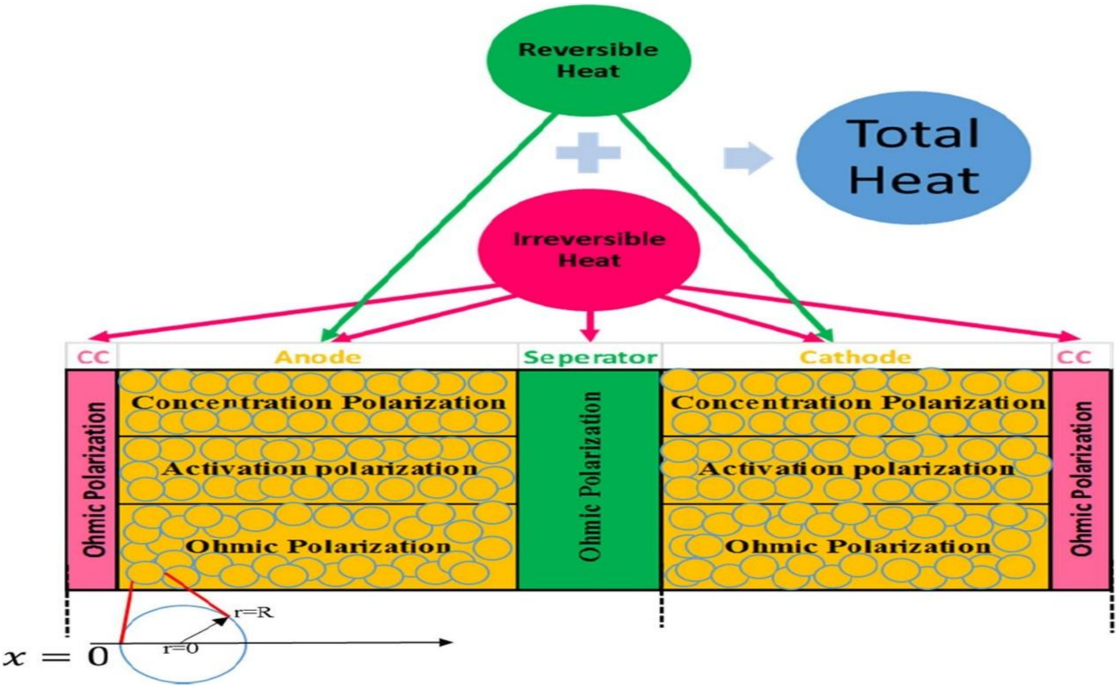

Figure 20 Illustration of the model structure and heat generation sources in lithium-ion batteries (Nazari & Farhad, 2017).

2.1.2 Heat Transfer in LIBs

LIBs are complex, heterogeneous systems in which electrochemical and thermal phenomena are strongly coupled. When considering heat transfer within these systems, the three primary mechanisms, conduction, convection, and radiation must be evaluated. Given the internal structure of LIBs, which predominantly consists of solid–solid and solid–liquid interfaces, heat conduction serves as the principal mode of internal heat transfer (Sun et al., 2025).

If significant temperature gradients are anticipated within the lithium-ion cell, thermal modelling typically employs a form of the three-dimensional heat conduction equation, as shown in Equation (4). This approach is particularly relevant for scenarios such as safety simulations, pre-heating studies, and fast-charging investigations. In this context, the thermal conductivity directly influences the spatial and temporal distribution of the cell temperature, T, which is a function of both position (x, y, z) and time t. Due to the layered structure of the electrode and separator stack, lithium-ion batteries exhibit anisotropic thermal conductivity, with distinct values in each Cartesian direction (k_x, k_y, k_z). Although Equation (4) is typically expressed in Cartesian coordinates, it can also be formulated in cylindrical coordinates (r, z, φ), which is often more appropriate for cylindrical cell geometries (Steinhardt et al., 2022).

$$\rho C_p \frac{\partial T}{\partial t} = \frac{\partial}{\partial x}\left(k_x \frac{\partial T}{\partial}\right) + \frac{\partial}{\partial y}\left(k_y \frac{\partial T}{\partial}\right) + \frac{\partial}{\partial z}\left(k_z \frac{\partial T}{\partial}\right) + q''' \tag{4}$$

where ρ is the average density of the battery, C_p is the average specific heat capacity, q''' is the volumetric heat generation rate.

If internal temperature gradients within the cell are negligible, typically indicated by a low Biot number, the lumped capacitance model, as presented in Equation (5), provides a suitable approach for modelling the cell temperature. In this simplified model, the temperature rise of the cell is primarily governed by its specific heat capacity and the heat dissipation, which together determine the amount of energy required to alter the cell's temperature (Steinhardt et al., 2022).

$$\rho \mathrm{V_{cell}} \mathrm{C_p} \frac{\partial T}{\partial t} = q''' \mathrm{V_{cell}} - q_{diss} \tag{5}$$

$$q_{diss} = q_{conv} + q_{rad} \tag{6}$$

where the q_{diss} is heat dissipation that is combination of convection and radiation heat transfer and V_{cell} is the volume of the cell. Thermal convection and radiation are considered at the free boundary, as expressed in Equations (7) and (8).

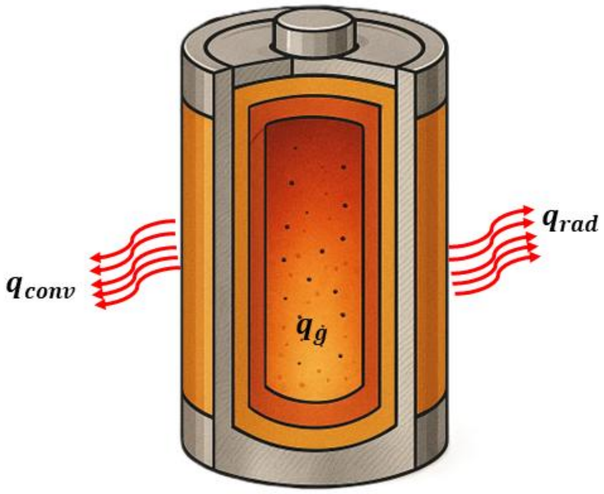

Figure 21 Illustration of Two Primary Heat Dissipation Mechanisms in a Battery Cell: Natural Convection and Thermal Radiation (Kovács et al., 2025).

$$q_{conv} = \mathrm{hA}(T - T_a) \tag{7}$$

$$q_{rad} = \varepsilon\sigma(T^4 - T_a^4) \tag{8}$$

where h is the natural convective heat transfer coefficient, T represents the surface boundary temperature, T_a is the ambient temperature, ε denotes the surface emissivity, and σ is the Stefan–Boltzmann constant.

Natural convective heat transfer between the battery and the external environment occurs through the relative motion of a fluid, typically air or liquid, across the battery surface. This passive method of thermal dissipation is employed in large scale energy storage systems. The effectiveness of natural convection is influenced by several factors, including fluid velocity, temperature gradients, and thermophysical properties such as density, specific heat capacity, and thermal conductivity (Sun et al., 2025).

When a fluid flows over a heated battery surface, higher flow velocities enhance heat removal. At a constant flow rate, a lower fluid temperature increases the temperature difference between the surface and the fluid, thereby improving convective heat transfer. Fluids with high specific heat capacity can absorb more heat, while those with high thermal conductivity are more effective in transporting it away from the surface (J. W. Han et al., 2022).

In addition to convection, thermal radiation also plays a role in heat dissipation, especially at higher operating temperatures. Radiation is a form of energy transfer that does not require a medium and occurs through electromagnetic waves emitted from the battery surface. The net radiative heat transfer depends on surface emissivity, surface temperature, and ambient temperature. Although radiation is generally less dominant compared to conduction and convection in lithium-ion batteries, its contribution becomes more significant at elevated temperatures due to its proportionality to the fourth power of temperature (Hatchard et al., 2000).

Convection can be further classified into natural and forced types, as illustrated in the Figure 22 . Natural convection arises from buoyancy effects driven by density differences in the fluid, while forced convection is induced by external means such as fans or pumps. Compared to forced convection, natural convection typically exhibits lower heat transfer rates and limited temperature control (Sun et al., 2025).

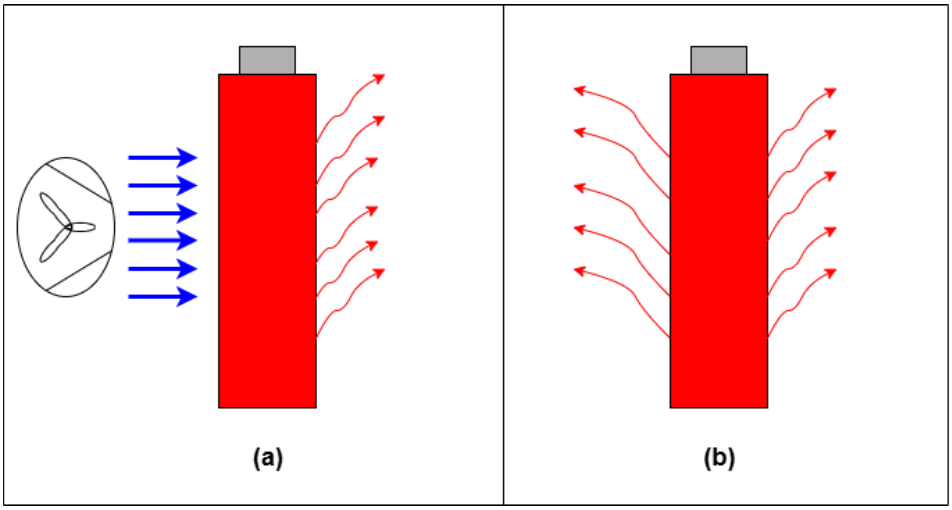

Figure 22 Illustration of (a) Forced Convection and (b) Natural Convection Mechanisms.

2.1.3 Previous works on Cell Modelling

The first comprehensive formulation for quantifying heat generation in electrochemical systems was presented by (Bernardi et al., 1985), who derived a general energy balance equation that accounted for reversible, irreversible, and mixing heat contributions within a unified thermodynamic framework. This model provided the theoretical foundation for analysing the thermal behaviour of batteries and continues to underpin contemporary electro-thermal modelling approaches. Subsequently, (Doyle et al., 1993) extended this concept by developing the first pseudo-two-dimensional (P2D) electrochemical model for lithium-ion polymer cells. Their model coupled charge, mass, and energy conservation to predict spatial variations in potential, concentration, and temperature during galvanostatic cycling. Collectively, these pioneering works established the fundamental framework for integrated electrochemical–thermal modelling and have remained the cornerstone for subsequent advancements in battery system analysis. Building upon these foundational studies, a range of recent investigations have advanced battery thermal and electrochemical modelling through experimental validation and multi-dimensional simulation approaches. A summary of these representative studies is presented in Table 1, highlighting their key findings.

Table 1 Recent Studies on Thermal and Electrochemical Simulation of Lithium-Ion Cells.

Serial no.	Author	Battery Type	Key Findings
1	(Paccha-Herrera et al., 2020)	Cylindrical 26650 cell, LCO	Compared three thermal modeling approaches under constant and dynamic discharges. All models agreed with experiments (max error ≈ 1.3 °C at 1.5C). Lumped model provided reliable results with minimal computational cost, while coupled electrochemical–thermal model captured voltage and temperature fields most accurately.
2	(Al Hallaj et al., 1999)	Cylindrical 18650, LCO	Developed and validated a 1D transient thermal model for Sony 18650 Li-ion cells using calorimetric data. The model accurately predicted temperature evolution at moderate C-rates and demonstrated a strong dependence of temperature rise on cooling rate. Thermal runaway was observed between 104–144 °C depending on state of charge, defining safety thresholds for larger-scale cell designs.
3	(U. Han & Lee, 2022)	Cylindrical 21700, NMC	The proposed inverse heat transfer analysis (IHTA) method was validated under discharge rates ranging from 0.25C to 2.0C, demonstrating excellent agreement with experimental data (≈1% error) and confirming its reliability in predicting temperature evolution across varying load conditions.
4	(Bahiraei et al., 2017)	Prismatic Cell, NCA	Developed a pseudo-3D electrochemical–thermal model coupling 1D electrochemical and 3D heat transfer equations to simulate temperature evolution in an NCA prismatic cell. The model accurately predicted cell temperature within 4% deviation from experiments and demonstrated increasing temperature with discharge rate, reaching 39.7 °C at 3C under safe operating limits.
5	(Xie et al., 2018)	Pouch Single Cell, LTO	A combined experimental and analytical study developed a transient heat-generation model under air cooling. Higher C-rates and lower ambient temperatures increased heat generation and temperature rise. The model accurately predicted cell temperature (with less than 2% error), confirming discharge produced more heat than charge and overdischarge caused sharp temperature rise.

Table 1 Continued.

6	(M. Chen et al., 2020)	Cylindrical 18650 cells, NMC and LFP	Conducted charge–discharge experiments at 1C–2C comparing natural convection, PCM, and PCM-fin cooling. PCM cooling reduced NMC cell temperature by 4.7 °C at 1C and 12.8 °C at 2C, while LFP cells showed smaller drops (approximately 2 °C). The method effectively stabilized temperature and preserved capacity under higher C-rates.
7	(Q. Wu et al., 2023)	Cylindrical 21700, NCA	Measured anisotropic thermal conductivity and heat capacity, then established a 2D axisymmetric thermal model using HPPC-derived resistance and entropy data. The model accurately predicted core and surface temperatures (with less than 1.5 °C deviation) under 1C–2C discharge. Core temperature reached 60 °C at 2C with approximately 3 °C internal gradient, validating the model's reliability for real-cell thermal behavior.
8	(Jeon, 2014)	Cylindrical 18650, LCO	Developed a coupled electrochemical–thermal model combining porous-electrode and transient heat-transfer formulations to predict temperature evolution of a cell. The model accurately reproduced experimental trends, showing higher discharge temperatures (approximately 50 °C at 2C) and a transition from entropic to Joule-dominated heating with increasing C-rate.
9	(Shi et al., 2022)	Cylindrical 18650, LFP	Developed a lumped thermal characteristic model coupled with the Bernardi equation to estimate internal temperature online. Introduced an adaptive forgetting-factor recursive least squares – joint Kalman filter for co-estimation of internal temperature and external thermal resistance. Experimental validation under HPPC, Beijing bus dynamic stress test BBDST, and full-cycle tests showed high accuracy with a maximum RMSE of 0.53 °C, confirming robustness for real-time battery management applications.

Table 1 Continued.

10	(Özdemir et al., 2021)	Cylindrical 18650, NCA	A coupled electrochemical–thermal model was developed to solve mass, charge, and heat-transfer equations incorporating a variable convective coefficient. Experimental validation under 0.5C–1.5C discharges demonstrated excellent agreement with measured data (with less than 1 °C and 0.11 V RMSE). The model effectively captured mandrel-induced temperature gradients while confirming nearly uniform thermal behavior at low C-rates.
11	(Mevawalla et al., 2020)	pouch cell, LFP	A pseudo-three-dimensional electrochemical–thermal model was developed by coupling one-dimensional electrochemical and three-dimensional heat-transfer equations to simulate a 5 Ah NCA prismatic pouch cell. The model demonstrated strong agreement with experimental data (with less than 4 % deviation) and accurately captured the temperature rise with increasing discharge rate, reaching 39.7 °C at 3C while remaining within the safe operational range.
12	(Abbas et al., 2024)	Pouch cell, NMC	A three-dimensional lumped thermal model based on a resistance-network approach was developed and validated against a detailed finite-element model for a single NMC pouch cell. The model accurately reproduced both transient and steady-state temperature evolution under 1C–5C discharges, achieving less than 0.5 °C deviation from FEM predictions while reducing computational time from six hours to approximately three seconds.

2.2 Battery Module Modelling

A lithium-ion battery module is an assembly of interconnected cells configured to deliver higher voltage and capacity than a single cell. Modules are typically designed with integrated thermal management features to maintain the temperature within safe operational limits, thereby enhancing reliability and safety. In addition, BMSs are often incorporated at the module level to monitor parameters such as cell voltage and temperature, enabling active balancing and performance optimization. This not only improves overall system efficiency but also contributes to prolonging the battery's service life (Shinde et al., 2023).

Figure 23 Battery Module Configured in a 3P4S Arrangement(Avik, 2024).

2.2.1 Previous works on Module Modelling

The earliest systematic investigations into battery pack thermal behaviour were conducted at the national renewable energy laboratory (NREL) in the late 1990s. (Pesaran & Burch, 1997) made a pioneering contribution by presenting one of the first comprehensive analyses of the thermal performance of EV and HEV battery modules and packs. Their work combined fundamental heat transfer modelling with finite element simulations to assess temperature evolution within lead–acid modules and across multi-module pack assemblies. The study demonstrated how internal heat generation, module geometry, airflow configuration, and casing thermal conductivity influence temperature gradients at the pack level. Importantly, it highlighted that inadequate thermal design can lead to temperature non-uniformity, accelerated aging, and electrical imbalance among cells and modules, emphasizing the necessity of dedicated battery thermal management systems.

Building on this foundation, (Pesaran, 2002) introduced one of the earliest lumped-capacitance thermal models for battery pack analysis within NREL's ADVISOR vehicle simulation platform. This work enabled prediction of battery temperature evolution under realistic drive-cycle conditions and linked thermal behaviour to electrochemical performance indicators such as internal resistance, available power, and efficiency.

Additionally, 2D and 3D finite element analyses were used to explore pack-level airflow configurations, revealing that parallel airflow architectures offer markedly improved temperature uniformity compared to series configurations. Collectively, these studies laid the groundwork for modern approaches to battery pack thermal modelling.

Table 2 summarises recent studies on lithium-ion battery pack modelling, highlighting the cell chemistries employed and the key findings of each work.

Table 2 Recent Studies on Thermal and Electrochemical Modelling of Lithium-Ion Battery Module.

Serial no.	Author	Battery Type	Key Findings
1	(Wang et al., 2025)	6 Prismatic cells, LFP	Using a thermoelectric coupling model, the study analyzed airflow direction, intake velocity, and cell arrangement in a six-cell prismatic LFP pack. Aligning airflow with cell length improved cooling, while staggered arrangements reduced local hotspots. An optimal configuration (10 mm staggered distance, 5 mm spacing) lowered maximum temperature by 0.5% and temperature difference by 4.2%, demonstrating enhanced cooling and improved uniformity.
2	(Abbas et al., 2024)	10 Pouch cells, NMC	Proposed a low-computational 3D lumped thermal model that captures thermal interactions between cells, tabs, and insulation layers. The model closely matched FEM predictions with a maximum deviation of approximately 0.42 °C while reducing computational time from 21 h (FEM) to 6 s for a 10-cell module. Results demonstrated accurate temperature prediction for both single-cell and multi-cell modules across discharge and periodic cycling conditions.

Table 2 Continued.

3	(Mangaiyarkarasi & Jayaganthan, 2024)	12 cylindrical cells of 21700, NMC	Developed a 3D electrochemical–thermal model using the P2D framework to evaluate heat generation, dissipation, and life span of a 6s2p pack with multiple cathode chemistries under air cooling. The NMC pack achieved the best thermal stability with an optimal temperature range of 21.3–32.8 °C, maximum heat dissipation of 102.5 W, and SOC/SOH retention of 100%/80%. Despite faster capacity fade, NMC chemistry provided superior heat management and operational efficiency compared with LCO, LFP, and LMO systems.
4	(J. W. Han et al., 2022)	16 cylindrical cells of 18650, NMC	Conducted experimental and numerical evaluation of a liquid-cooled 4S4P NMC pack under 1C–4C discharges. The system maintained cell temperatures below 40 °C, and the chiller-assisted configuration improved temperature uniformity by up to 35%. Model–experiment agreement was within 2 K, confirming the accuracy of the thermal predictions and the effectiveness of the pack's symmetrical cooling design.
5	(M. K. Tran, Mathew, et al., 2021)	5 pouch cells, LFP	Developed a Thevenin-based equivalent circuit model that incorporates the effects of state of charge, state of health, and temperature on model parameters. Experimental validation demonstrated an RMSE below 20 mV and a MAPE below 0.5%, representing approximately a 50% improvement in voltage prediction accuracy compared to conventional models and confirming its suitability for real-time battery management applications
6	(F. Chen et al., 2020)	16 cylindrical cells of 26650, LFP	Compared air and PCM cooling under an HEV load profile. Air cooling kept temperatures within safe limits but showed higher non-uniformity, whereas PCM cooling achieved excellent uniformity ($\Delta T < 0.4$ °C) but increased mean temperature and reduced cycle life. Overall, air cooling was found to be more cost-effective and durable when considering thermal performance and ageing.

Table 2 Continued.

7	(K. Li et al., 2018)	16 cylindrical cells of 18650, NMC	Demonstrated that water-pipe cooling significantly improves pack thermal behavior under dynamic CC–CV cycling. Simulation closely matched experiments, with deviations mainly attributed to constant thermo-physical parameters and neglected contact resistance. Water cooling maintained safe temperatures at low C-rates, while PCM became more effective at high C-rates. Results indicate that a hybrid PCM–water system offers optimal performance across varying load conditions.
8	(Yang et al., 2015)	60 cylindrical cells of 18650, LFP	Developed and validated a coupled electrochemical–thermal model to investigate forced air-cooling in aligned and staggered cylindrical-cell packs. Results showed that increasing longitudinal spacing reduced maximum temperature but increased power demand, while larger transverse spacing improved uniformity but raised average temperature. The optimized aligned configuration (S_x = 34 mm, S_y = 32 mm) achieved balanced cooling performance with minimal temperature non-uniformity.
9	(Jaguemont et al., 2016)	4 Prismatic cells, LFP	Developed a coupled electro-thermal model for prismatic LFP cells and a 4-cell pack, validated from –20 °C to 25 °C with approximately 3% error. The model accurately captured voltage behavior, energy loss, and self-heating at low temperatures, and reproduced pack-level non-uniformity with higher temperatures in inner cells.
10	(Basu et al., 2016)	30 cylindrical cells of 18650, NCA	Developed a 3D coupled electrochemical–thermal model for a liquid-cooled 6S5P NCA pack. Experimental validation showed approximately 90% accuracy with less than 1 K deviation, while the proposed design maintained temperature rise below 7 K at 2.7C, ensuring compactness and high thermal uniformity.

3 Characterization Methods

In this master's thesis, the experimental investigations were carried out on a commercial cylindrical lithium-ion cell in the 21700 format with NCA chemistry and a nominal capacity of 4.5 Ah. The key specifications of the cell are listed in Table 3. Further analysis of the cell required measurement of the open circuit voltage and the implementation of charge–discharge cycling under controlled loading conditions, which will be presented in the following sections.

To perform the experimental measurements, a Neware battery cycler Model BTS-4000 was used. A battery cycler is an essential instrument that enables the controlled application of current and the simultaneous measurement of voltage in electrochemical cells. In practice, the cycler allows the operator to define charging and discharging protocol, apply the required current with high precision, and continuously record the corresponding voltage response of the cell. In addition, the cycler actively monitors both current and voltage in real time, ensuring accurate execution of test profiles and reliable data acquisition.

Table 3 Technical Specifications of the Lithium-Ion Cells Used in This Study

No.	Particulars	Values
1	Brand Name	Molicel
2	Model Name	INR-21700-P45B
3	Capacity (Typical)	4500 mAh
4	Cell Voltage	3.6 V (Nominal)
		4.2 V (Charge)
		2.5 V (Discharge)
5	Charge Current	4.5 A (Standard)
		13.5 A (Maximum)
6	Discharge Current	45 A (Continuous)
7	Operating Temperature	0°C to 60°C (Charge)
		-40°C to 60°C (Discharge)
8	Shape	Cylindrical
9	Diameter	21.55 mm
10	Height	70.15 mm
11	Weight	70 g

In this work, the Neware BTS-4000 was employed to conduct both OCV characterization and dynamic cycling tests.

Figure 24 Single-cell testing was conducted using the Neware battery cycler(Avik, 2024).

3.1 Open Circuit Voltage (OCV) Measurements

The OCV of a cell is a static function of its state of charge (SOC) and temperature, whereas most other aspects of cell performance are dynamic in nature. Therefore, separate experiments are required to characterize the OCV–SOC relationship and the cell's dynamic behaviour. To determine the OCV profile, the general procedure is as follows: the cell is first fully charged, then discharged at a very low current to the minimum operating voltage while continuously monitoring both the terminal voltage and the cumulative ampere-hours discharged. Subsequently, the cell is recharged, again at a very low current, to its maximum operating voltage, with voltage and charge data recorded throughout the process. This slow charge–discharge cycle ensures that the voltage approximates the true equilibrium OCV at each SOC point (Plett, 2015).

The slow charge–discharge rate is intended to minimize excitation of the cell's dynamic behaviour and maintain a quasi-equilibrium state throughout the test. While a C/30 rate is commonly used as a compromise between equilibrium accuracy and test duration, a C/50 rate was employed in this study to further reduce transient effects (Petzl & Danzer, 2013). Based on Figure 18, the terminal voltage can be expressed as Equation (9),

$$U_t = R_0 I + \sum_i R_i I exp(-t/\tau_i) + U_{ocv} \tag{9}$$

Here, R_0 represents the ohmic resistance, and τ is the time constant defined as the product of resistance and capacitance in the equivalent RC circuit. Therefore, by reducing the current, the first two terms on the right-hand side of Equation (9) can be neglected.

OCV profiles obtained during charging and discharging differ due to voltage hysteresis, which arises from thermodynamic asymmetry, kinetic polarization, and structural changes in the electrode materials. As a result, the OCV is not a single-valued function of the SOC, with the charging OCV typically appearing higher than the discharging OCV at the same SOC. To maintain consistency in modelling, an averaged OCV–SOC curve is commonly used to suppress hysteresis-related variations and provide a smooth, single-valued relationship suitable for equivalent-circuit and electrochemical models (Barai et al., 2015; H. Feng et al., 2021).

To obtain a unified OCV curve from both charging and discharging data, two methods were employed. The first is the conventional approach, referred to as the averaged-OCV at constant-SOC method (Bussios et al., 2024). As illustrated in Figure 25, this method requires averaging between points **B** and **C**, which represent the OCV values from the discharge and charge cycles, respectively. The second approach, known as the averaged-SOC at constant-OCV method (Ning & Zhang, 2015), involves averaging between points **A** and **B**, which correspond to the SOC values from the charge and discharge cycles, respectively.

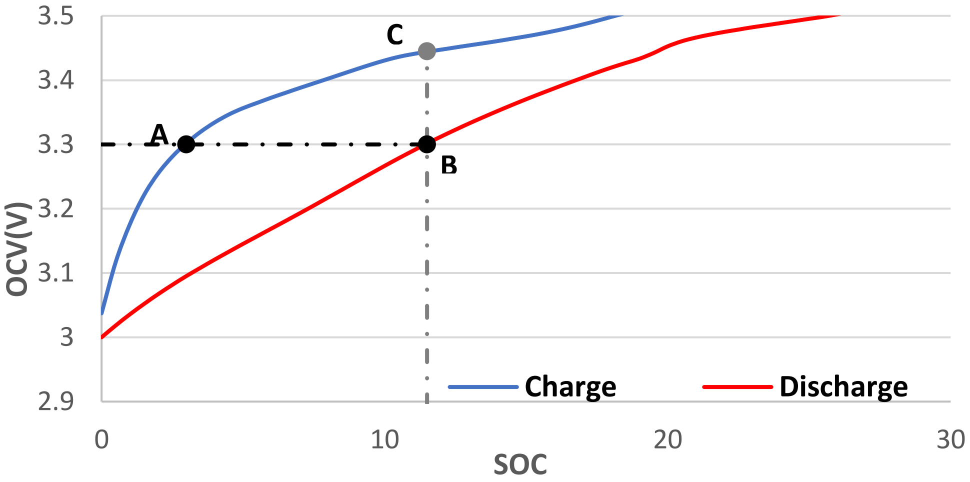

Figure 25 Schematic Representation of OCV Calculation Using Two Different Methods.

As previously noted, the OCV is also a function of temperature, and in Section 2.1.1 , we introduced the concept of reversible (entropic) heat. To evaluate the entropic heat coefficient in a lithium-ion battery, charge and discharge experiments were conducted at different temperatures using a low current rate of C/50 (Hua et al., 2023). The slope of this linear fit at each SOC point corresponds to the entropic heat coefficient which quantifies the reversible heat contribution. This analysis was repeated for multiple SOC levels to obtain a full profile of the entropic heat coefficient as a function of SOC.

For this experimental procedure, a Gamry Reference 3000 potentiostat was employed to precisely regulate the applied current and voltage throughout the measurements. In parallel, a Weiss climate chamber was utilized to ensure a stable and well-controlled ambient temperature, thereby minimizing external thermal disturbances and enabling consistent test conditions.

3.2 Cycling

The looped cyclic charge and discharge test was conducted using the Neware BTS 8.0. The cells were cycled using a constant current–constant voltage (CC–CV) charging protocol followed by a constant current (CC) discharging protocol at various C-rates. After each charge and discharge step, a 30-minute rest period was implemented to allow the cell's voltage and temperature to stabilize before proceeding to the next cycle. The temperature of each cell during cycling was measured using a PT100 sensor, which provides an accuracy in the range of ±0.1 to ±0.3 °C (Kako, 2023). To verify the thermal model under different operating conditions, three C-rates were selected. A 0.5C rate represents mild cycling with limited heat generation, serving as a baseline for model accuracy under low-stress conditions. The 1C rate corresponds to nominal operation, often used as a benchmark in both experiments and simulations. Finally, the 2C rate reflects an extreme scenario with significantly higher heat generation and thermal gradients, testing the robustness of the model under aggressive cycling. This range of C-rates is commonly adopted in battery studies to cover realistic usage as well as worst-case conditions (Kako, 2023; Patel et al., 2025). A comprehensive summary of the cycling parameters is presented in Table 4.

Table 4 Cycling Protocol for Different C-rates

C-rate **Parameters**	0.5C	1C	2C
Charging Current (A)	2.25	4.5	9
Charging Voltage cut-off (V)	4.2	4.2	4.2
Charge Current Cut-off after CV charge (mA)	50	50	50
Rest Period (s)	1800	1800	1800
Discharge Current (A)	-2.25	-4.5	-9
Discharge Voltage Cut-off (V)	3.0	3.0	3.0
Rest Period (s)	1800	1800	1800
Number of Cycles tested	2	2	2

3.3 Heat Transfer Coefficient Measurement

To characterize the overall heat transfer coefficient h of the battery cell, a dedicated cooling experiment was conducted. Estimating h through empirical correlations was considered impractical, as convective and radiative heat losses are influenced by various factors, including ambient temperature, airflow conditions, cell geometry, and surface properties that are difficult to capture accurately with standard models. Instead, h was determined by analyzing the battery's cooling behaviour following a charge cycle. In the experiment, the cell was charged using CC charging and then left to cool in a quiescent environment. Throughout this cooling period, two thermocouples were used to continuously monitor the ambient air temperature, while a third thermocouple, affixed to the cell surface using thermal paste to ensure good thermal contact, measured the cell temperature. This setup ensured that the recorded temperature decay was predominantly governed by natural convection and radiation to the surroundings, allowing for a reliable estimation of the overall heat transfer coefficient (U. Han & Lee, 2022).

During the rest period, when no electrochemical reactions take place, the thermal behaviour of the cell can be described by a simplified energy balance. The general form of the energy conservation equation for the cell is given in Equation (5). Once the discharge ends, the volumetric heat generation term becomes negligible, and the temperature decay is governed solely by heat dissipation. This heat loss is modelled using Newton's law of cooling, incorporating convection as expressed in Equations (6)-(8). Substituting these terms into the energy balance yields a first-order differential equation that describes the cell temperature T during the cooling phase.

$$\mathrm{\rho V_{cell} C_p} \frac{\partial T}{\partial t} = -\,\mathrm{hA}(T - T_a) \tag{10}$$

This differential equation describes how the cell temperature decays toward the ambient temperature due to heat loss. All quantities in Equation (10) are known or measurable except for h, which must be determined. The cell's mass was known, and area was calculated from the cell geometry and the value for specific heat was taken from (Murashko et al., 2020). Thus, h was treated as an unknown parameter to be extracted from the cooling data. To estimate h,an inverse heat transfer analysis was carried out by fitting the model to the measured cooling curve. By manipulating the governing equations, the following expression is obtained:

$$T_a - T = \left(T_{a,0} - T_0\right)e^{-\frac{t}{\tau}} \tag{11}$$

$$\tau = \frac{\mathrm{mC_p}}{\mathrm{hA}} \tag{12}$$

where τ is the time constant and $T_{a,0}$ and T_0 ambient and cell temperature, respectively.

3.4 Calorimetric Cycling Experiments

An isothermal calorimeter was used to precisely measure the total heat generation of the lithium-ion cell during charge–discharge cycling. This method allows direct quantification of both reversible and irreversible heat, ensuring accurate evaluation of the cell's thermal behaviour. As shown by (Nazari & Farhad, 2017), conducting measurements under constant temperature conditions using an isothermal calorimeter minimizes external temperature effects and provides reliable data for validating thermal models and improving battery thermal management systems.

The calorimetric cycling experiments were conducted using a Thermal Hazard Technology (THT) IBC-PL Isothermal Battery Calorimeter, integrated with a Huber MPC Minichiller 600 temperature control unit. The IBC-PL is specifically designed to study the thermal behaviour of pouch and prismatic lithium-ion cells under strictly controlled isothermal conditions. The calorimeter quantifies the heat generated by the cell through precise measurement of the temperature differential between two parallel plates, one fixed and one adjustable, thermally connected to a heat-sink block via a calibrated thermal resistance plate. The heat produced by the cell induces a proportional temperature difference across these plates, which is continuously monitored to calculate the corresponding heat flow.

A Huber Minichiller 600 circulated thermostated fluid through the calorimeter jacket to maintain the chamber temperature at a fixed set point of 30 °C, ensuring stable isothermal operation as described in the manufacturer's documentation. The cell was positioned centrally between the measurement plates, and good thermal contact was ensured using the recommended clamping procedure and a thin thermal interface layer.

To perform the charge–discharge cycling, a Chroma 17011 battery cell tester was connected to the calorimeter via the electrical feedthroughs provided on the instrument. The tester supplied controlled current and voltage profiles while the calorimeter simultaneously recorded the associated heat generation. Data acquisition was carried out using both the THT Control Software and Battery Pro Software: the former recorded heat-flow data, whereas the latter collected voltage, current, and cell temperature data. Figure 26 illustrates a schematic representation of the calorimeter setup.

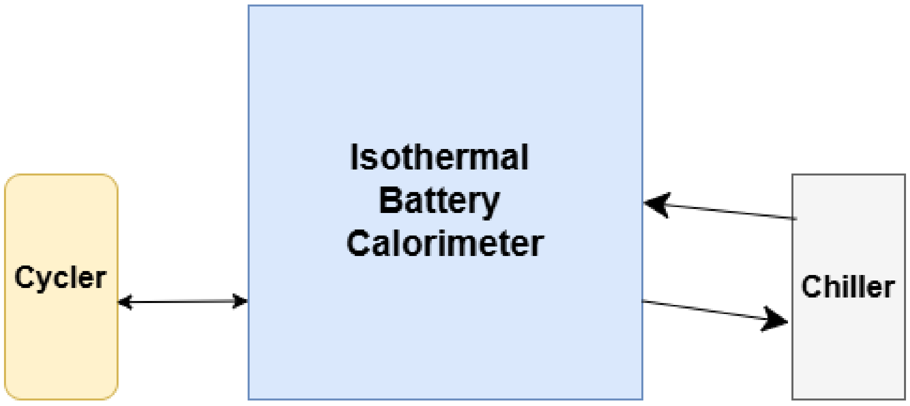

Figure 26 Schematic representation of the calorimeter setup.

This integrated setup enables accurate quantification of total, reversible, and irreversible heat generation during dynamic cycling of pouch and prismatic lithium-ion cells under well-defined isothermal conditions. However, the calorimeter used in this study was not originally intended for cylindrical cells, which introduces additional uncertainty in the measurements. The cylindrical 21700 cell establishes only a narrow line of contact with the flat calorimeter plates, leading to higher and non-uniform thermal contact resistance; as a result, part of the generated heat may dissipate laterally or through pathways that bypass the calibrated heat-flux sensors. Small air gaps between the curved surface and the plates further increase uncertainty, and although the calorimeter maintains an isothermal boundary, it cannot compensate for these geometry-dependent deviations in heat-flux distribution.

4 Single Cell Modelling

To translate the developed single-cell thermal model into a practical simulation framework, a computational platform was required that could efficiently handle nonlinear, time-dependent equations and allow for flexible integration of experimental data. MATLAB® was selected for this purpose due to its widespread use in battery modelling, its robust numerical solvers for differential equations, and its built-in tools for data processing and visualization. Moreover, MATLAB enables straightforward integration of experimental inputs such as open-circuit voltage (OCV), entropic heat coefficients, and specific heat capacity into the model, while providing flexibility to test different boundary conditions and cycling profiles. These capabilities make MATLAB an appropriate choice for implementing the thermal model, ensuring both computational efficiency and reproducibility of results (Y. Liu, 2025).

4.1 MATLAB Implementation

The single-cell thermal model was implemented in MATLAB® R2024b to simulate the temperature evolution of the lithium-ion cell during charge and discharge cycles. The governing equations, presented in the section 2.1 , are derived from the Bernardi equation, which accounts for both irreversible heat generation and reversible entropic contributions, as expressed in Equation (13). To numerically solve the coupled first-order differential equations describing the cell's thermal dynamics, the ode45 solver was employed. This solver uses an adaptive Runge–Kutta method, providing an optimal balance between computational efficiency and numerical accuracy, making it particularly suitable for problems involving nonlinear temperature-dependent parameters (Álvarez et al., 2021).

$$\mathrm{mC_p}\frac{\partial T}{\partial t} = \left(V - OCV - T\frac{\partial U_{ocv}}{\partial T}\right)I - \mathrm{hA}(T - T_a) \tag{13}$$

The model input parameters consisted of the experimentally measured OCV, the entropic heat coefficients, and the specific heat capacity reported by (Auch et al., 2023). These parameters were integrated into MATLAB scripts to evaluate transient thermal responses under different C-rate profiles. Additionally, the implementation was structured to allow flexible configuration of boundary conditions, enabling the inclusion of various convective heat transfer coefficients and ambient temperature settings. By rearranging Equation (13), hA can be eliminated, allowing the thermal behavior to be expressed in terms of a lumped time constant. As discussed in Section 3.3 , this simplification enables the model to be reformulated using the thermal time constant, τ, facilitating a more compact and practical implementation for parameter estimation and simulation.

$$\frac{\partial T}{\partial t} = \frac{\left(V - OCV - T\frac{\partial U_{ocv}}{\partial T}\right)I - \frac{\mathrm{mC_p}}{\tau}(T - T_a)}{\mathrm{mC_p}} \tag{14}$$

The voltage, current, and temperature data are time-dependent variables. To simulate them in MATLAB, an interpolation function was required to align the datasets with a uniform time interval. For this purpose, the built-in one-dimensional interpolation function “interp1” was employed.

To compare the OCV and terminal voltage by evaluating their difference, it was first necessary to determine the SOC for each data point. The SOC was tracked using the coulomb-counting method during both the charge and discharge cycles. Because the cells were allowed to rest at the end of each cycle, the voltage relaxed toward equilibrium, enabling the final SOC of each rest period to be used as the initial SOC for the subsequent cycle. This approach ensured a consistent and accurate SOC reference throughout the entire dataset.

$$SOC = SOC_0 + \int \frac{I(t)}{\mathrm{C_n}}dt \tag{15}$$

Where SOC_0 is the initial SOC and $\mathrm{C_n}$ is the nominal capacity of the cell.

4.2 Error Analysis

To evaluate the accuracy of the thermal model and its agreement with the experimental measurements, two common error metrics are used: the Root Mean Square Error (RMSE) and the error percentage. These indicators quantify the deviation between simulated and measured values and provide an objective measure of model performance.

4.2.1 Root Mean Square Error (RMSE)

RMSE is a widely used statistical metric that expresses the average magnitude of the error between predicted and observed values. It is calculated as:

$$RSME = \sqrt{\frac{1}{n}\sum_{1}^{n}(T_{sim} - T_{exp})^2} \tag{16}$$

Where T_{sim} is the simulated value, T_{exp} is the corresponding experimental value, and n is the total number of data points.

RMSE places a higher weight on larger deviations due to the squared error term, making it sensitive to peak differences or rapid transitions in the dataset. A lower RMSE indicates better agreement between simulation and experiment (Chai & Draxler, 2014).

4.2.2 Error Percentage

Error percentage provides a normalized measure of deviation relative to the magnitude of the reference (experimental) value. It is often calculated using absolute error:

$$Error(\%) = \left(\frac{|T_{sim} - T_{exp}|}{T_{exp}}\right) \times 100 \tag{17}$$

This metric expresses the error in percentage terms, allowing the performance to be assessed independently of the scale of the measured variable. It is particularly useful when comparing different operating conditions or datasets with varying magnitudes (Kim & Kim, 2016).

5 Results

This chapter summarises the key experimental findings and modelling outcomes of this work. It begins with the identification of parameters required for the thermal model, followed by the characterisation of cell voltage behaviour and temperature-dependent properties. The latter part of the chapter evaluates the model performance under different C-rate conditions and compares the predicted heat generation with calorimetric measurements. Together, these results provide the basis for assessing the accuracy and applicability of the developed thermal model.

5.1 Heat Transfer Coefficient

To assess the repeatability of the measurement procedure, the experiment was performed independently on two separate cells. As shown in Figure 27, the ΔT decay profiles of both cells exhibit very similar behaviour, and the fitted exponential curves overlap closely across the entire time range. The extracted time constant for both cells is approximately $\tau = 500$ s, demonstrating a high level of consistency between the two measurements and confirming the reliability of the experimental setup.

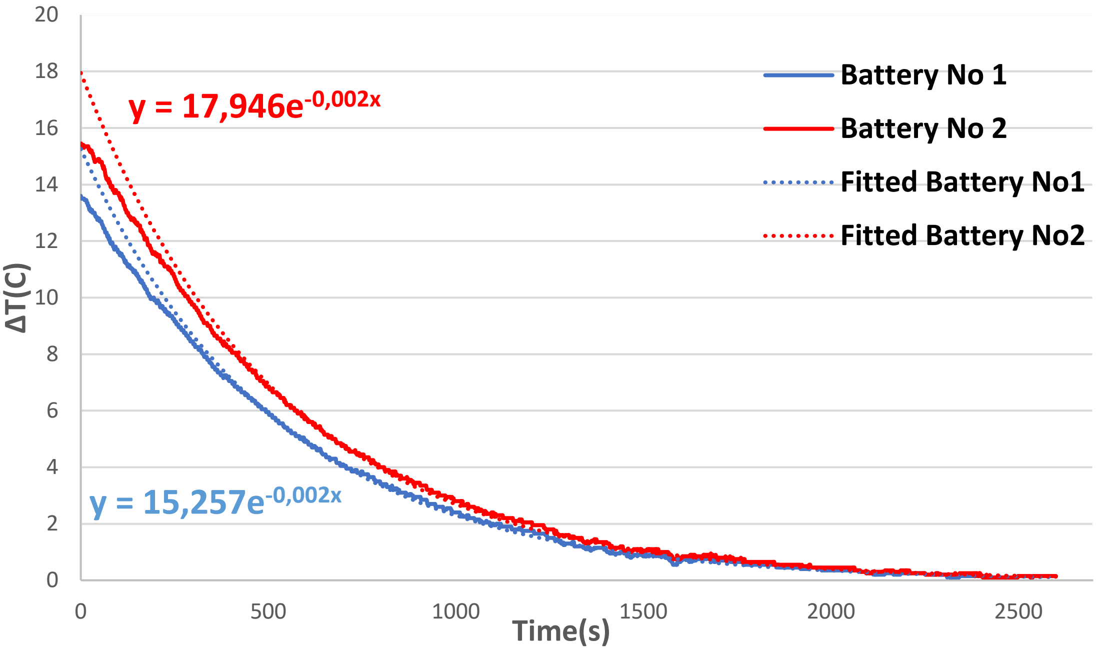

Figure 27 Fitted Cooling Curve from Experimental Data.

5.2 Reference OCV Measurements

Figure 28 presents the OCV–SOC relationship for both the charging and discharging paths. A distinct voltage hysteresis is observed across most of the operating range. At low SOC, the charging OCV is noticeably higher than the discharging OCV, with the difference gradually diminishing toward mid-SOC. Between approximately 40–90% SOC, the two curves nearly converge, after which a small separation becomes visible again as the cell approaches full charge. Overall, the OCV–SOC profiles remain smooth for both directions, with the charging trajectory consistently exhibiting slightly higher voltages than the discharging trajectory throughout the entire SOC window.

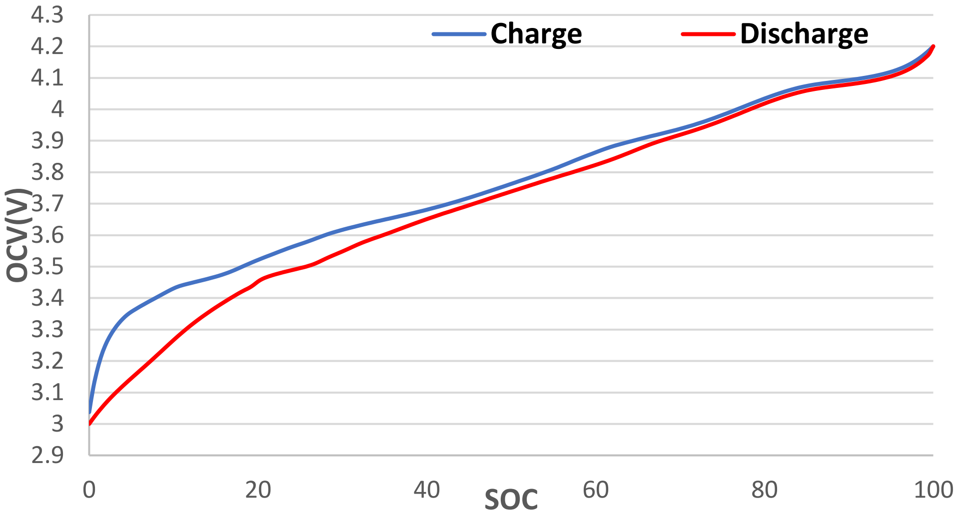

Figure 28 OCV as a Function of SOC for Both Charging and Discharging Processes.

Figure 29 compares the OCV–SOC profiles obtained using the Averaged-OCV at Constant-SOC method and the Averaged-SOC at Constant-OCV method. Both methods produce nearly identical OCV curves, following the same smooth and monotonically increasing trend across the entire SOC range. The two profiles overlap closely throughout most of the window, with only minor deviations appearing at very low SOC (0–30%). These differences remain small, and the overall shape and magnitude of the OCV–SOC relationship are consistent between the two approaches, indicating that both methods provide a comparable representation of the cell's OCV–SOC relationship.

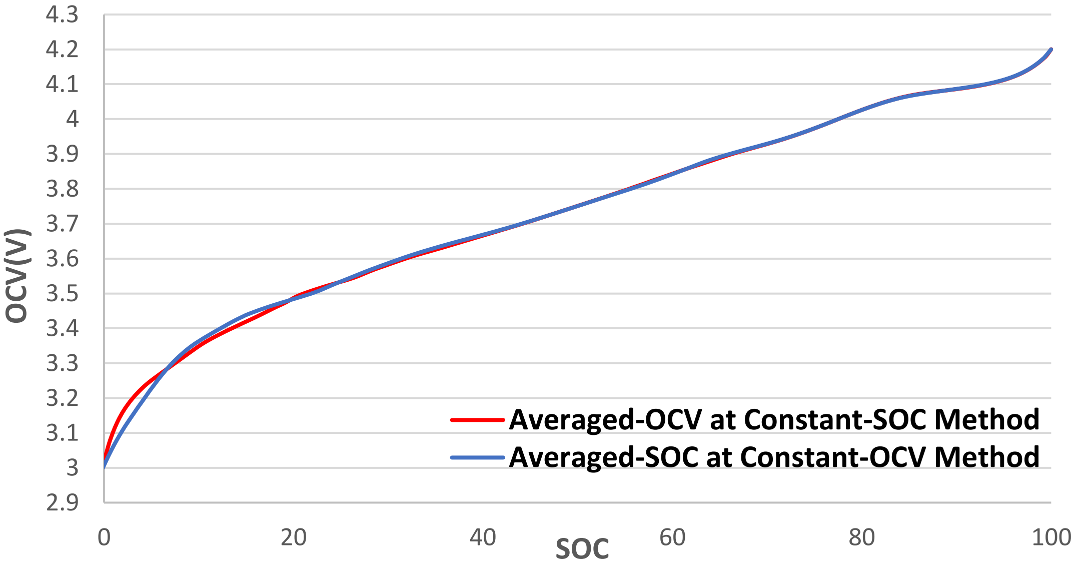

Figure 29 Two Different Methods for Obtaining a Unified OCV Curve.

5.3 OCV at Different Temperature Measurements

The experiments were conducted at three temperatures: 23 °C, 30 °C, and 40 °C. However, during the OCV measurement at 30 °C, an unexpected issue occurred, rendering the corresponding dataset unreliable for use in the simulations. As shown in Figure 30, the measured values at 30 °C deviate markedly from the consistent trends observed at 23 °C and 40 °C.

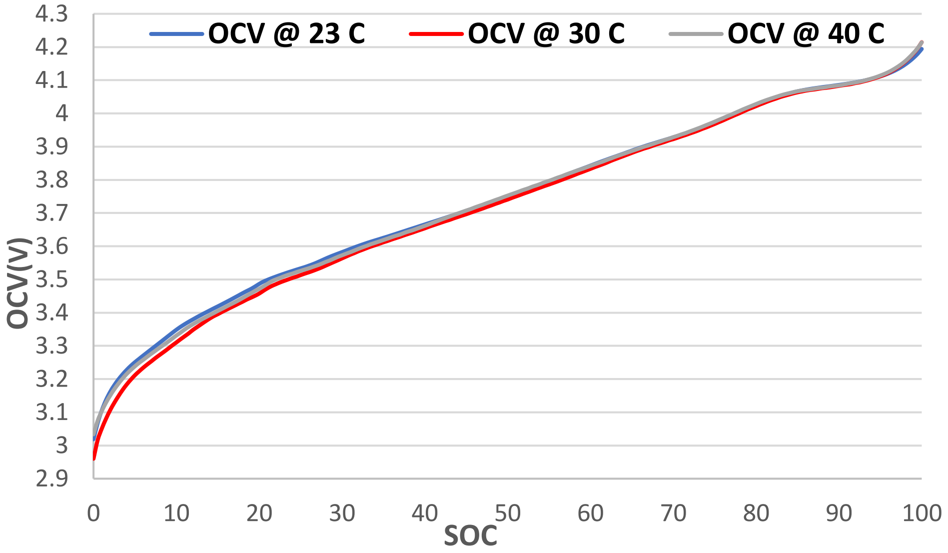

Figure 30 Comparison of OCV–SOC Curves Measured at 23 °C, 30 °C, and 40 °C.

5.4 Entropic Heat Coefficient

Figure 31 presents the entropic heat coefficient (EHC) as a function of SOC for both the charging and discharging paths, including the experimentally measured curves and the reference data extracted from (Friedrich et al., 2022). The experimental charging and discharging curves show clear directional asymmetry, with the charging EHC remaining close to zero and mostly negative across the SOC range, aside from a sharp rise at very low SOC. In contrast, the discharging curve exhibits a much wider variation, reaching more negative values at low SOC, becoming positive between roughly 40–90% SOC, and showing a steep increase near full charge. Overall, the discharging path displays consistently larger absolute values, and the two experimental profiles do not overlap. The reference curves from

Friedrich show significantly smaller magnitudes and smoother behaviour, remaining mostly negative and only becoming slightly positive at high SOC.

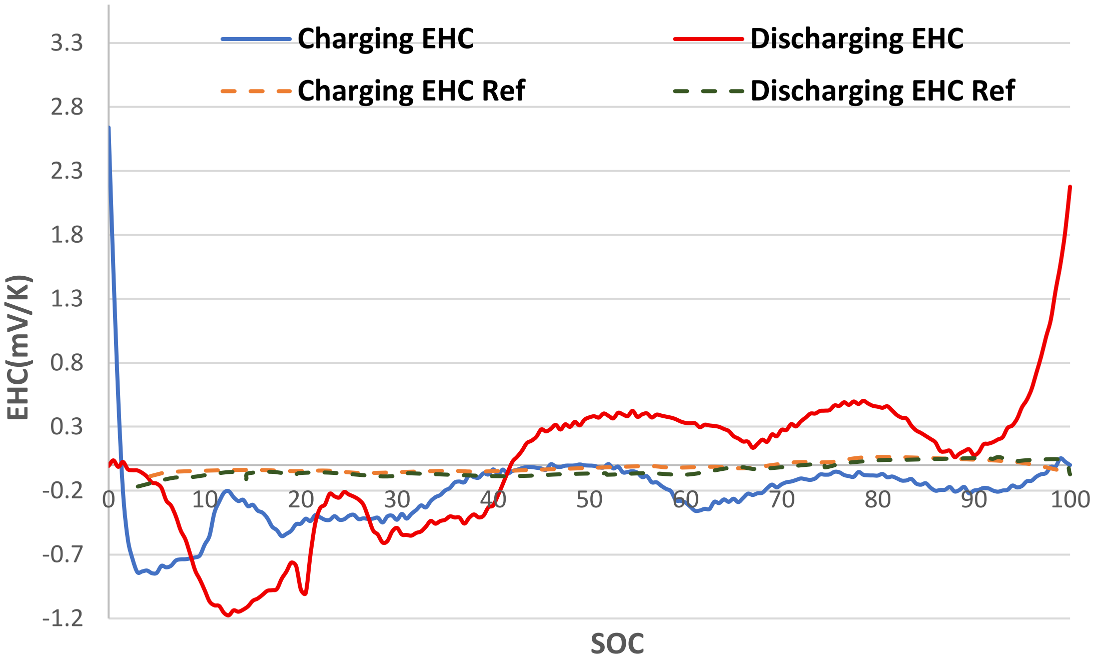

Figure 31 Charging vs. discharging entropic heat coefficient (EHC), including experimentally measured data and reference EHC from (Friedrich et al., 2022).

The entropic heat coefficient (EHC) represents the reversible heat exchange associated with lithium intercalation and deintercalation. In a fully reversible electrochemical system, the EHC profiles obtained during charging and discharging would be identical, as the underlying entropy change is thermodynamically the same in both directions. However, numerous studies have reported that the charge and discharge EHC curves do not coincide in practical lithium-ion systems (Bernardi et al., 1985; Zilberman et al., 2018). This asymmetry is typically attributed to electrode hysteresis, kinetic polarization, and path-dependent entropy variations. These effects are especially pronounced at low and high SOC, where phase transitions, staging phenomena, and non-ideal solid-solution behaviour occur (Assat et al., 2019). As a result, although symmetric EHC curves would indicate perfectly reversible thermodynamics, the asymmetry observed in the literature reflects the intrinsic irreversibility of real lithium-ion cells.

5.5 Charge-discharge cycling

In this section, the results corresponding to the 0.5C, 1C, and 2C cycling rates are presented. The temperature figures in this section report the temperature rise (ΔT), whereas the absolute temperature profiles for each operating condition are provided in Appendix 1.

5.5.1 Results at 0.5C-Rate

Figure 32 shows the voltage and current profiles for the 0.5C-rate cycle. At this low C-rate, the constant-current (CC) charging period lasted approximately 6224 s, followed by a CC discharging period of 6519 s. After the discharge current was cut off, the cell exhibited a voltage relaxation of $\Delta V \approx 130\,\text{mV}$, reflecting the decay of ohmic and concentration overpotentials toward the equilibrium OCV.

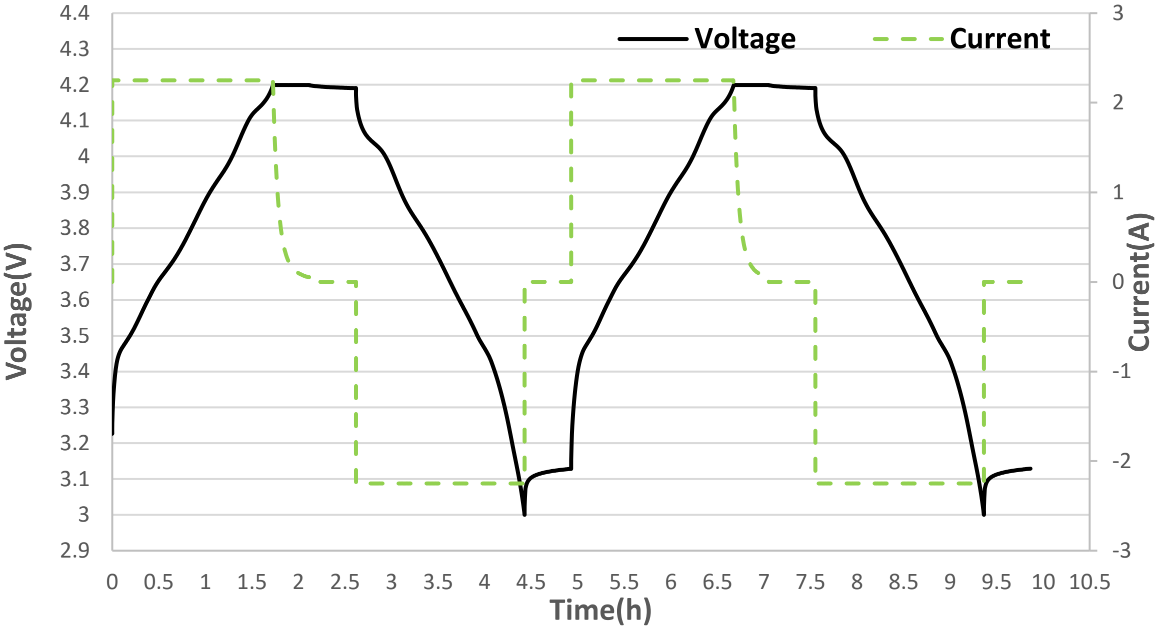

Figure 32 Experimental Voltage and Current Profiles at 0.5C-Rate.

Figure 33(a) presents the simulated and experimental cell–ambient temperature difference (ΔT) for the 0.5C-rate cycle using both OCV-processing approaches. The Averaged-OCV at Constant-SOC method resulted in an RMSE of 0.57 K and a maximum error of 5.1%, yielding a peak simulated ΔT of 3.1 K during discharge. In contrast, the Averaged-SOC at Constant-OCV method improved the agreement with the experimental data, reducing the RMSE to 0.47 K and the maximum error to 5.03%, while producing the same peak simulated

ΔT of 3.1 K. The maximum experimental ΔT reached 3.25 K, which provides the reference level for evaluating model fidelity under low C-rate conditions. As expected, the temperature rise during discharge is higher than during charge, with an average peak difference of 0.72 K between the charging and discharging phases of each cycle.

Figure 33(b) presents the simulation results obtained when the entropic heat coefficient (EHC) is included in the model. Incorporating the EHC leads to an increase in the RMSE to 1.75 K, which can be attributed to uncertainties in the experimental EHC measurements. The largest deviations occur at the beginning of both the charging and discharging steps, where the EHC is highly sensitive to the state of charge. As discussed in Section 5.4 , the experimentally determined EHC values are higher than the reference values reported in the literature. Because the entropic heat contribution is directly proportional to the EHC, this discrepancy propagates through the model and results in the observed differences in the predicted temperature profiles.

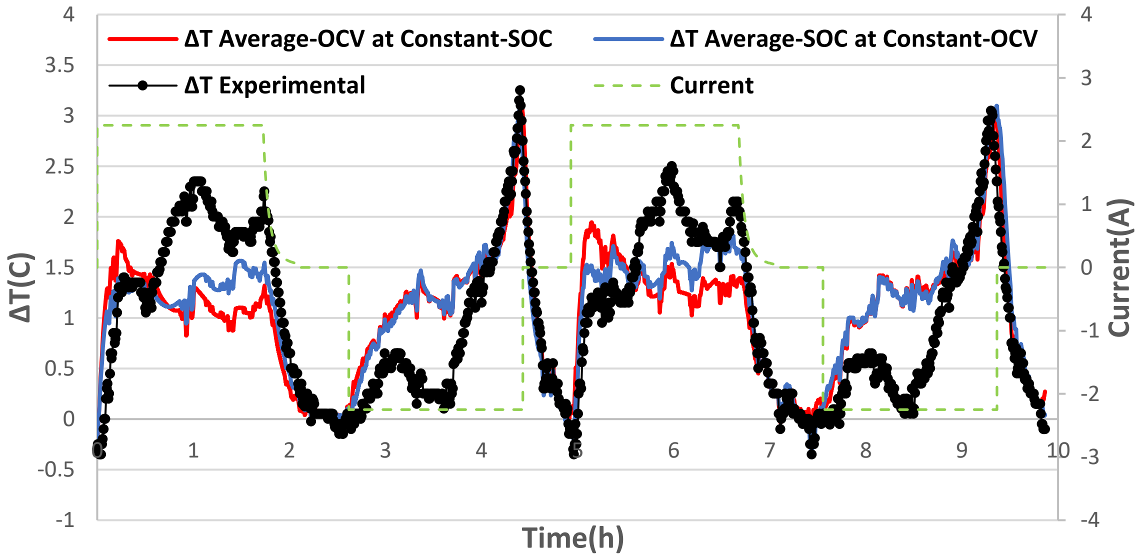

(a)

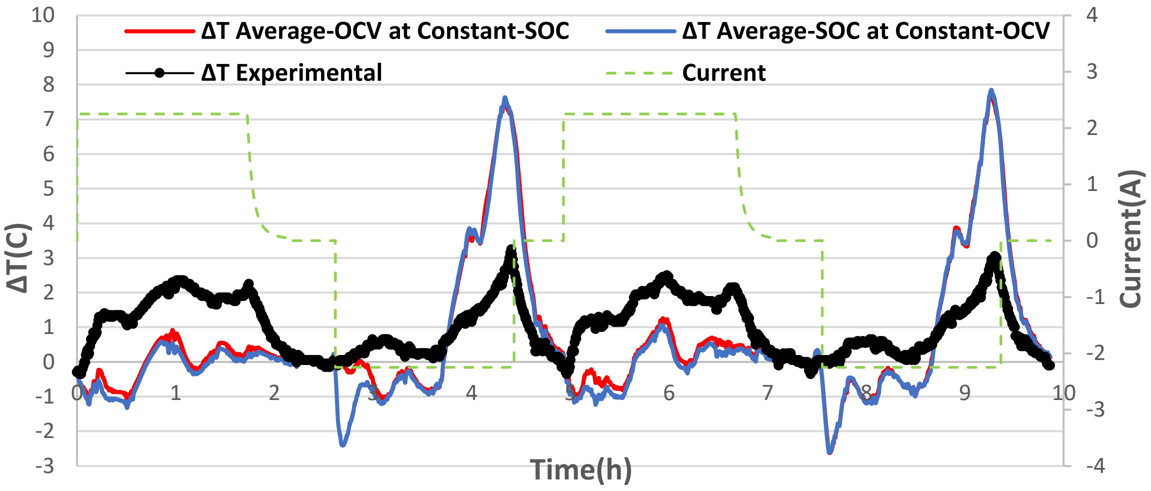

(b)

Figure 33 Illustration of the Simulated and Experimental Cell–Ambient Temperature Difference (ΔT) with the Applied Current Profile at 0.5C-Rate: (a) Excluding the EHC and (b) Including the EHC.

5.5.2 Results at 1C-Rate

Figure 34 presents the voltage and current behaviour at a 1C-rate cycle. Under this nominal operating condition, the constant-current (CC) charging period lasted approximately 2999 s, and the CC discharging period lasted 3235 s. After the discharge phase, the voltage recovered by ΔV ≈ 160 mV, indicating a stronger relaxation effect compared with the 0.5C case due to increased polarization.

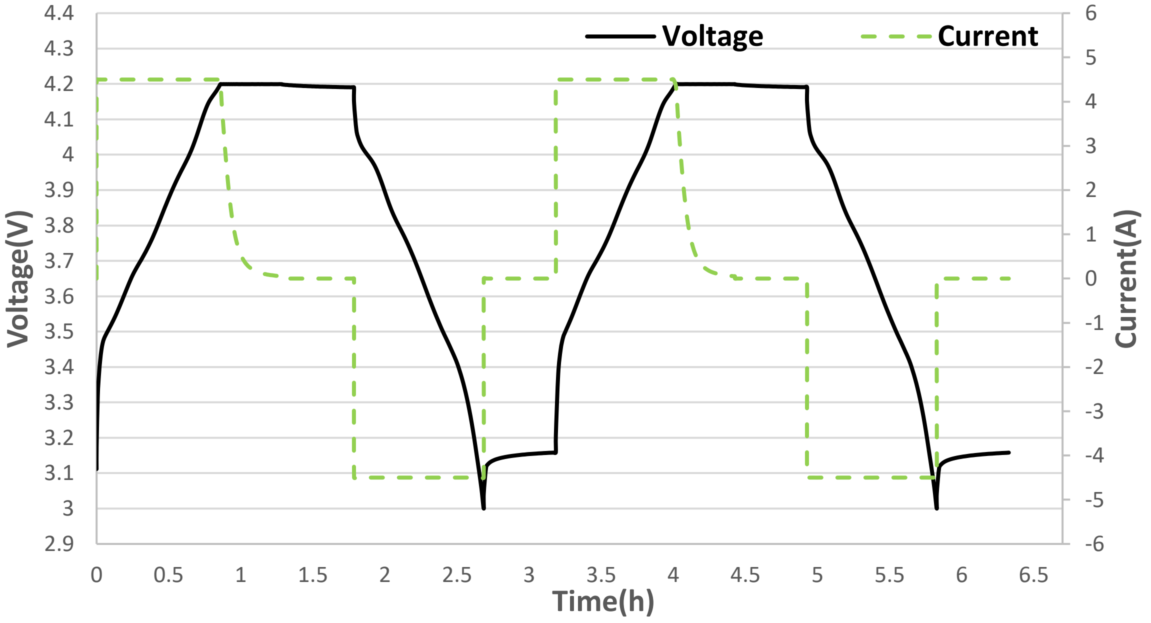

Figure 34 Experimental Voltage and Current Profiles at 1C-Rate.

Figure 35(a) presents the ΔT comparison for the 1C-rate cycle. As expected, increasing the current results in a higher temperature rise and greater sensitivity to the selected OCV averaging methods. Using the Averaged-OCV at Constant-SOC method, the RMSE increased to 1.14 K and the maximum error to 10.12%, with a peak simulated ΔT of 5.6 K during discharge. When applying the Averaged-SOC at Constant-OCV method, the agreement with the experimental trend improved, lowering the RMSE to 0.93 K and the maximum error to 9.79%, and yielding a peak ΔT of 5.9 K. The maximum experimental ΔT reached 6.2 K, illustrating the stronger thermal response at nominal C-rate operation. The temperature rise during discharge remained higher than during charge, though with a reduced peak difference of 0.58 K compared with the 0.5C case.

Figure 35(b) shows the results when the EHC is included. Similar to the 0.5C condition, inaccuracies in the measured EHC data introduce additional deviations. However, the influence is more pronounced at 1C, where the RMSE increases to 2.77 K. The largest errors appear at low and high SOC, where the entropic contribution to heat generation is strongest.

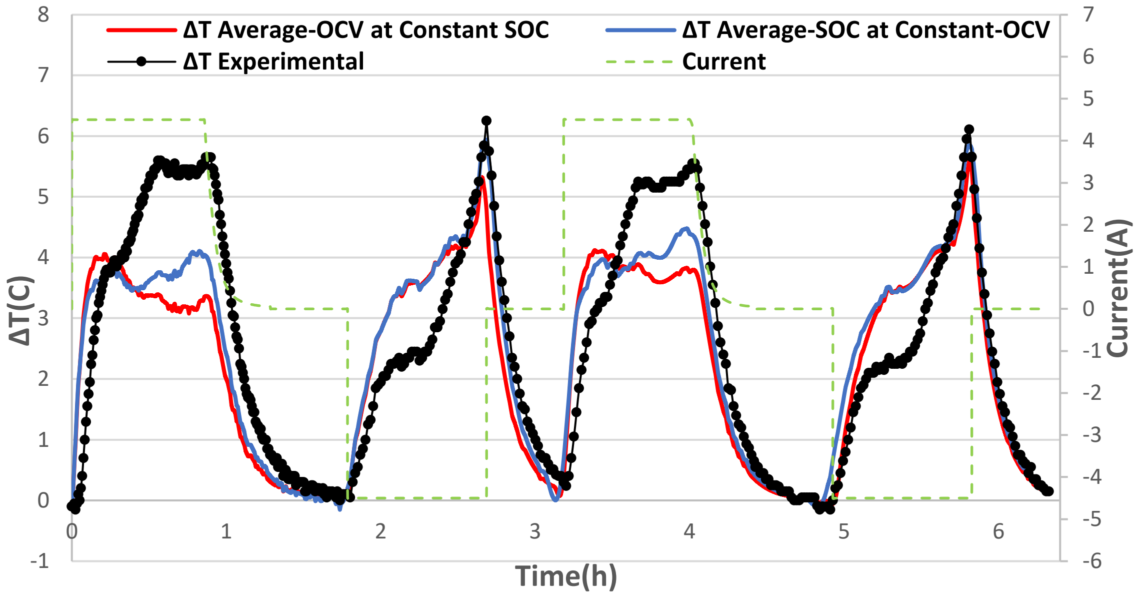

(a)

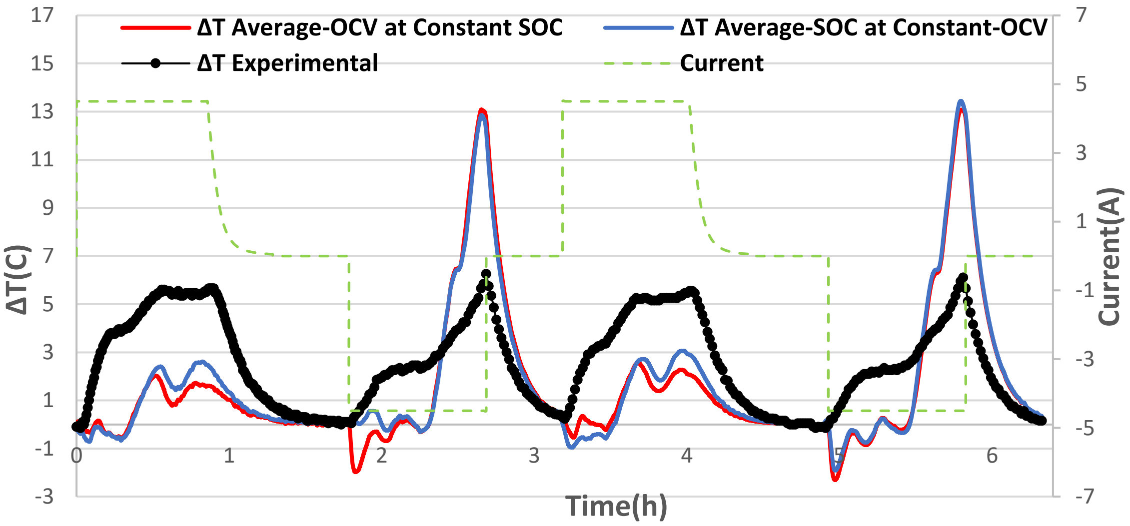

(b)

Figure 35 Illustration of the Simulated and Experimental Cell–Ambient Temperature Difference (ΔT) with the Applied Current Profile at 1C-Rate: (a) Excluding the EHC and (b) Including the EHC.

5.5.3 Results at 2C-Rate

Figure 36 illustrates the voltage and current profiles at the 2C-rate. The higher current results in a significantly shorter constant-current (CC) charging duration of 1349 s and a CC discharging duration of 1594 s. A pronounced voltage relaxation of $\Delta V \approx 190$ mV was observed after the discharge phase, which is larger than the 130 mV relaxation at 0.5C and the 160 mV observed at 1C. This increasing trend reflects the stronger polarization and overpotential effects that develop at higher C-rates. The 2C case therefore represents the most demanding operating condition and is used to evaluate the model's robustness under aggressive cycling.

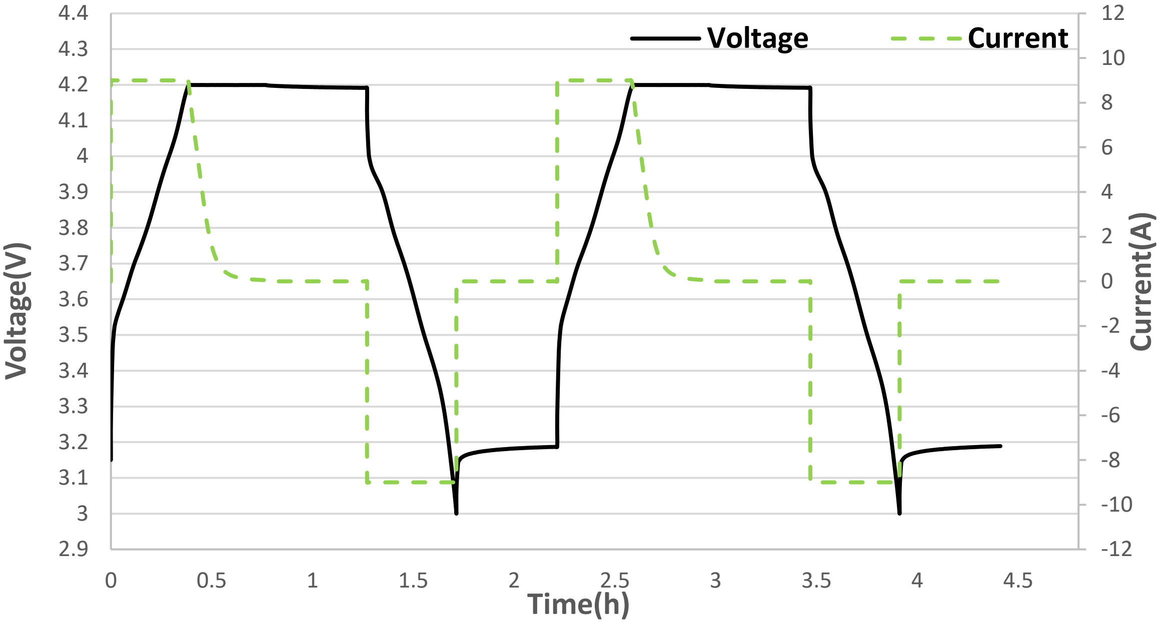

Figure 36 Experimental Voltage and Current Profiles at 2C-Rate.

Figure 37(a) illustrates the ΔT profiles for the 2C-rate cycle. This operating condition produces the highest thermal stress among all investigated cases, resulting in the largest ΔT values and the strongest amplification of modelling uncertainties. Using the Averaged-OCV at Constant-SOC approach, the RMSE reached 1.61 K and the maximum error 12.69%, with a peak simulated ΔT of 13.3 K. These values represent a substantial increase relative to the 0.5C and 1C results. The Averaged-SOC at Constant-OCV method retained superior accuracy, reducing the RMSE to 1.29 K and the maximum error to 9.48%. The peak experimental ΔT reached 14.25 K, confirming the significant heat accumulation associated with high-rate cycling.

Figure 37(b) presents the simulation results obtained with the EHC included in the model. As observed at the other C-rates, uncertainties in the measured EHC introduce additional deviations; however, the effect is most pronounced at 2C, where the entropic heat contribution coincides with the large irreversible (ohmic and polarization) losses. Consequently, the RMSE increases to 4.24 K, and the mismatch becomes most apparent during the late-charging and early-discharging stages. Furthermore, because the entropic heat term scales with the applied current, the high current at 2C amplifies the thermal response, resulting in the largest temperature deviation among all tested C-rates.

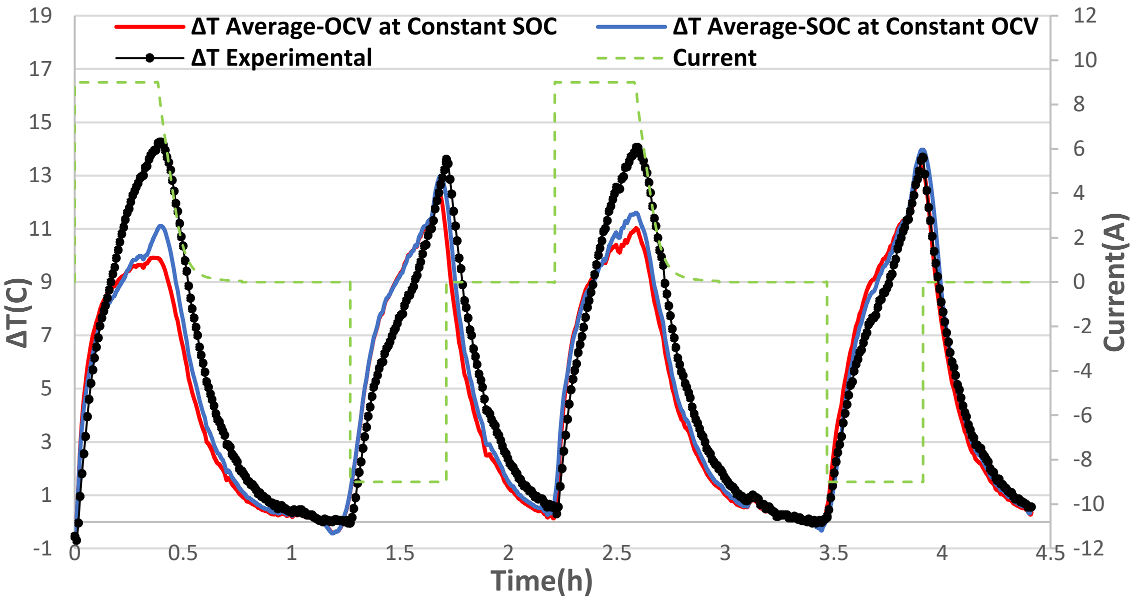

(a)

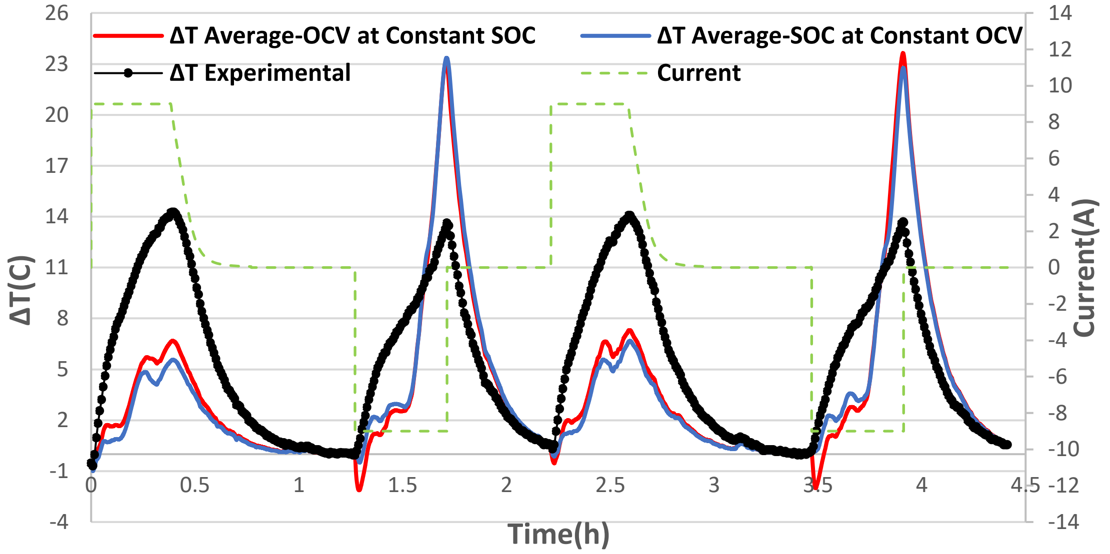

(b)

Figure 37 Illustration of the Simulated and Experimental Cell–Ambient Temperature Difference (ΔT) with the Applied Current Profile at 2C-Rate: (a) Excluding the EHC and (b) Including the EHC.

5.6 Calorimetric Results

Figure 38 illustrates the voltage and current profiles at the 1C- and 2C-rates used for calorimetric heat measurement. The average constant-current (CC) charging duration was 2737 s for 1C and 1176 s for 2C, while the corresponding discharge durations were 3166 s and 1526 s, respectively. A pronounced voltage relaxation was observed after the discharge phase, with $\Delta V \approx 187$ mV at 1C and $\Delta V \approx 242$ mV at 2C. These relaxation magnitudes are larger than those seen in the separate 1C and 2C measurements, as the cell was charged and discharged consecutively without a long rest period between the tests. Although the cutoff current for the constant-voltage (CV) charging phase was set to 50 mA, the device terminated the charge at approximately 90 mA. All other test conditions were identical to those listed in Table 4.

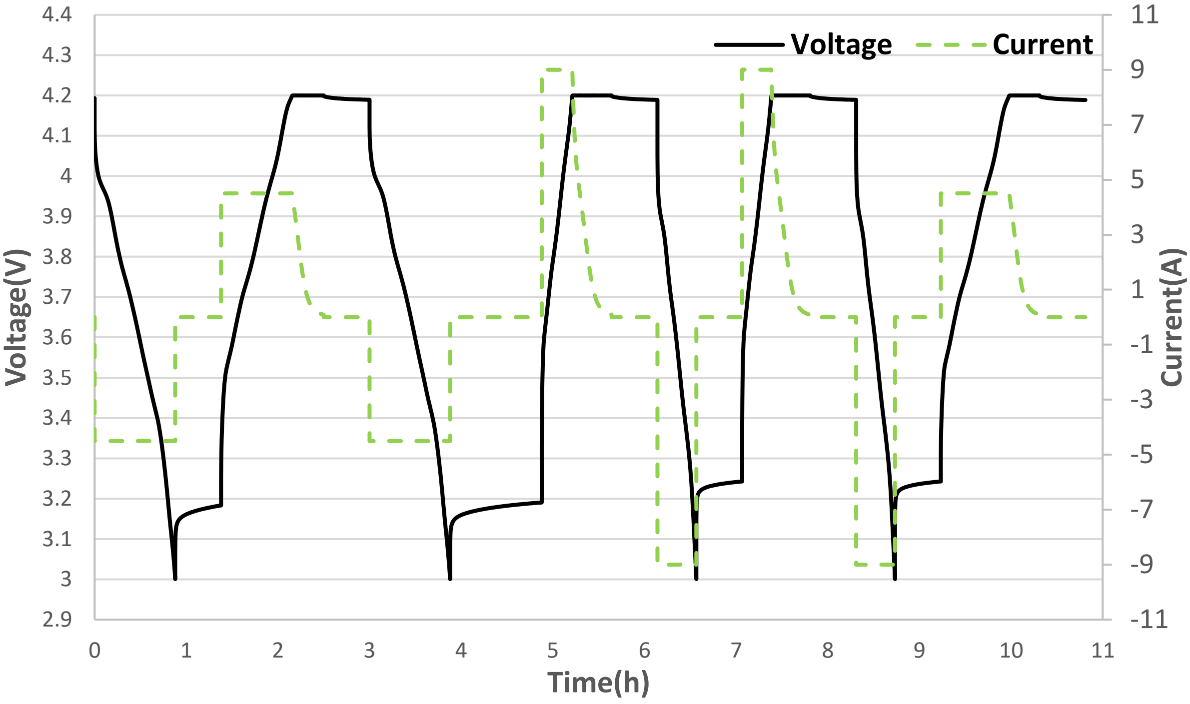

Figure 38 Experimental Voltage and Current Profiles at Different C-Rates.

Figure 39 presents the calorimetric heat measurement (black dashed line) alongside the heat derived from the irreversible heat generation expression $(V - U_{ocv}) * I$ (red solid curve). Although both profiles represent heat generation, the irreversible heat is approximately twice as high as the experimentally measured value. As discussed in Section 3.4 , this discrepancy arises from the design limitations of the calorimeter, which is optimised specifically for pouch and prismatic cells. As a result, its thermal response tends to underestimate the heat produced by cylindrical cells, leading to the observed deviation between the experimental and calculated heat generation profiles.

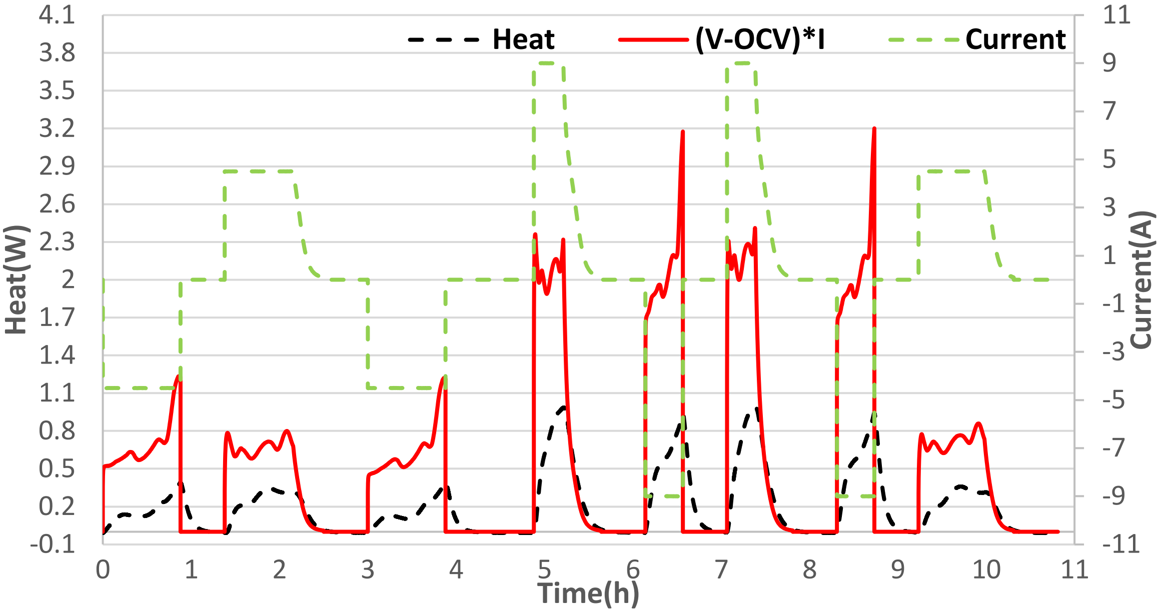

Figure 39 Experimental Calorimetric Heat Profiles for Two Consecutive Charge–Discharge Cycles at 1C and 2C.

6 Conclusion

This thesis examined the thermal behaviour of a 21700 NCA cylindrical lithium-ion cell and evaluated a lumped thermal model using experimentally derived inputs. A central focus of the work was the comparison of two different OCV–SOC construction methods, Averaged-OCV at Constant-SOC and Averaged-SOC at Constant-OCV, and their influence on the simulated temperature response across different C-rates.

The parameter identification demonstrated good repeatability, as cooling-curve measurements from two separate cells produced nearly identical ΔT decay profiles and a consistent thermal time constant of approximately 500 s. The reference OCV–SOC results confirmed voltage hysteresis between charging and discharging, and both OCV-averaging methods produced almost identical equilibrium curves with only minor deviations at low SOC. Temperature-dependent OCV measurements showed consistent behaviour at 23 °C and 40 °C, while clear irregularities were observed at 30 °C, leading to the exclusion of that dataset. The entropic heat coefficient measurements exhibited notable differences between the charge and discharge paths, especially at low and high SOC, which affected the accuracy of simulations that included reversible heat.

Using the two OCV-processing methods, the thermal model was evaluated at three C-rates: 0.5C, 1C, and 2C. At 0.5C, both methods produced similar results, with the Averaged-SOC at Constant-OCV method achieving slightly better agreement (RMSE 0.47 K) compared with the Averaged-OCV at Constant-SOC approach (RMSE 0.57 K). At 1C, the temperature rise increased, and the difference between the two methods remained small, though the SOC-averaged method again yielded better alignment with experiment. At 2C, the highest thermal stress occurred, resulting in the largest ΔT values and the strongest model deviations. Even under these demanding conditions, the SOC-averaged method provided the lower RMSE, demonstrating a more robust performance across all operating conditions.

Simulations incorporating the entropic heat coefficient demonstrated consistently higher errors across all C-rates, with discrepancies most prominent at low and high SOC where the entropy measurements exhibited the greatest instability. These results indicate that, although the reversible heat term is physically meaningful, its effective use in thermal modelling depends on highly reliable entropy data. To address this limitation, the potentiometric method at constant SOC can be proposed as a more accurate technique for determining the entropic heat coefficient. By evaluating the variation of open-circuit voltage with temperature under quasi-static or equilibrium conditions at fixed SOC values, this method isolates the reversible entropic contribution by eliminating current-dependent polarization and kinetic effects, thereby providing a more robust representation of the cell's thermodynamic behaviour.

Calorimetric cycling tests provided additional validation by measuring the heat generation directly. The irreversible heat calculated using $(V - U_{ocv}) * I$ was nearly twice the calorimetric measurement. This gap is explained by the known limitations of the calorimeter, which is optimized for pouch and prismatic cells and underestimates heat generation for cylindrical formats.

Overall, the results show that the developed lumped thermal model can accurately capture the temperature evolution of the 21700 cell when reliable input parameters are used. Among the two investigated simulation methods, the Averaged-SOC at Constant-OCV approach consistently provided better agreement with the experimental ΔT across all C-rates. The model is therefore suitable for use in thermal analysis and can support future thermal-management development for cylindrical lithium-ion cells.

7 References

Abbas, A., Rizoug, N., Trigui, R., Redondo-Iglesias, E., & Pelissier, S. (2024). Low-Computational Model to Predict Individual Temperatures of Cells within Battery Modules. *Batteries*, *10*(3). https://doi.org/10.3390/batteries10030098

Afzal, A., Kaladgi, A. R., Samee, M., Kumar, R., Ağbulut, Ü., & Park, S. G. (2023). A critical review on renewable battery thermal management system using heat pipes. *Journal of Thermal Analysis and Calorimetry*, *148*. https://doi.org/10.1007/s10973-023-12100-9

Al Hallaj, S., Maleki, H., Hong, J. S., & Selman, J. R. (1999). Thermal modeling and design considerations of lithium-ion batteries. *Journal of Power Sources*, *83*(1), 1–8. https://doi.org/https://doi.org/10.1016/S0378-7753(99)00178-0

Alehosseini, E., & Jafari, S. M. (2020). Nanoencapsulation of phase change materials (PCMs) and their applications in various fields for energy storage and management. *Advances in Colloid and Interface Science*, *283*, 102226. https://doi.org/https://doi.org/10.1016/j.cis.2020.102226

Al-Gabalawy, M., Hosny, N. S., & Hussien, S. A. (2020). Lithium-ion battery modeling including degradation based on single-particle approximations. *Batteries*, *6*(3), 1–26. https://doi.org/10.3390/batteries6030037

Álvarez, C., Espinel, E., & Noriega, C. J. (2021). Study of different alternatives for dynamic simulation of a steam generator using matlab. *Fluids*, *6*(5). https://doi.org/10.3390/fluids6050175

Arote, S. A. (2022). Lithium-ion and Lithium–Sulfur Batteries. In *Fundamentals to performance*. IOP Publishing. https://doi.org/10.1088/978-0-7503-4881-2

Assat, G., Glazier, S. L., Delacourt, C., & Tarascon, J.-M. (2019). Probing the thermal effects of voltage hysteresis in anionic redox-based lithium-rich cathodes using isothermal calorimetry. *Nature Energy*, *4*(8). https://doi.org/10.1038/s41560-019-0410-6ï

Assi, M., & Amer, M. (2025). A Comparative Analysis of Lithium-Ion Batteries Using a Proposed Electrothermal Model Based on Numerical Simulation. *World Electric Vehicle Journal*, *16*(2). https://doi.org/10.3390/wevj16020060

Auch, M., Kuthada, T., & Wagner, A. (2023). Simple experimental method to determine the specific heat capacity of cylindrical Lithium-Ion-Battery cells. *Applied Thermal Engineering*, *234*. https://doi.org/10.1016/j.applthermaleng.2023.121212

Avik, A. P. (2024). *Passive Thermal Management of a Li-Ion Battery Module Using Phase Change Materials (PCM)*.

Baetens, R., Jelle, B. P., & Gustavsen, A. (2010). Phase change materials for building applications: A state-of-the-art review. *Energy and Buildings*, *42*(9), 1361–1368. https://doi.org/https://doi.org/10.1016/j.enbuild.2010.03.026

Bahiraei, F., Fartaj, A., & Nazri, G. A. (2017). Electrochemical-thermal Modeling to Evaluate Active Thermal Management of a Lithium-ion Battery Module. *Electrochimica Acta*, *254*, 59–71. https://doi.org/10.1016/j.electacta.2017.09.084

Barai, A., Widanage, W. D., Marco, J., Mcgordon, A., & Jennings, P. (2015). A study of the open circuit voltage characterization technique and hysteresis assessment of lithium-ion cells. *Journal of Power Sources*, *295*, 99–107. https://doi.org/10.1016/j.jpowsour.2015.06.140

Basu, S., Hariharan, K. S., Kolake, S. M., Song, T., Sohn, D. K., & Yeo, T. (2016). Coupled electrochemical thermal modelling of a novel Li-ion battery pack thermal management system. *Applied Energy*, *181*, 1–13. https://doi.org/https://doi.org/10.1016/j.apenergy.2016.08.049

Bernardi, D., Pawlikowski, E., & Newman, J. (1985). A General Energy Balance for Battery Systems. *Journal of The Electrochemical Society*, *132*(1), 5. https://doi.org/10.1149/1.2113792

Bussios, M., Goldar, A., Garone, E., & Kinnaert, M. (2024). Fast Determination of OCV Curve for Lithium-ion Batteries. *2024 European Control Conference (ECC)*, 206–211. https://doi.org/10.23919/ECC64448.2024.10591299

Cai, S., Zhang, X., & Ji, J. (2023). Recent advances in phase change materials-based battery thermal management systems for electric vehicles. *Journal of Energy Storage*, *72*, 108750. https://doi.org/https://doi.org/10.1016/j.est.2023.108750

Cavus, M., Dissanayake, D., & Bell, M. (2025). Next Generation of Electric Vehicles: AI-Driven Approaches for Predictive Maintenance and Battery Management. In *Energies* (Vol. 18, Issue 5). Multidisciplinary Digital Publishing Institute (MDPI). https://doi.org/10.3390/en18051041

Chai, T., & Draxler, R. R. (2014). Root mean square error (RMSE) or mean absolute error (MAE)? - Arguments against avoiding RMSE in the literature. *Geoscientific Model Development*, *7*(3), 1247–1250. https://doi.org/10.5194/gmd-7-1247-2014

Chen, F., Huang, R., Wang, C., Yu, X., Liu, H., Wu, Q., Qian, K., & Bhagat, R. (2020). Air and PCM cooling for battery thermal management considering battery cycle life. *Applied Thermal Engineering*, *173*. https://doi.org/10.1016/j.applthermaleng.2020.115154

Chen, M., Zhang, S., Wang, G., Weng, J., Ouyang, D., Wu, X., Zhao, L., & Wang, J. (2020). Experimental analysis on the thermal management of lithium-ion batteries based on phase change materials. *Applied Sciences (Switzerland)*, *10*(20), 1–15. https://doi.org/10.3390/app10207354

Chen, X., Wang, B., Ye, Y., Liang, J., & Kong, J. (2025). Design of Electrodes and Electrolytes for Silicon-Based Anode Lithium-Ion Batteries. In *Energy and Environmental Materials* (Vol. 8, Issue 2). John Wiley and Sons Inc. https://doi.org/10.1002/eem2.12838

Cheng, Z. (2019). *Cylindrical Cell Thermal Modeling for an Automotive Battery Pack*. https://api.semanticscholar.org/CorpusID:189273890

Dasari, H., & Eisenbraun, E. (2021). Predicting capacity fade in silicon anode-based li-ion batteries. *Energies*, *14*(5). https://doi.org/10.3390/en14051448

Ding, X., Zhang, D., Cheng, J., Wang, B., & Luk, P. C. K. (2019). An improved Thevenin model of lithium-ion battery with high accuracy for electric vehicles. *Applied Energy*, *254*. https://doi.org/10.1016/j.apenergy.2019.113615

Dong, Y., Meng, J., Sun, X., Zhao, P., Sun, P., & Zheng, B. (2023). Experimental Study on Effects of Triggering Modes on Thermal Runaway Characteristics of Lithium-Ion Battery. *World Electric Vehicle Journal*, *14*(10). https://doi.org/10.3390/wevj14100270

Doyle, M., Fuller, T. F., & Newman, J. (1993). Modeling of Galvanostatic Charge and Discharge of the Lithium/Polymer/Insertion Cell. *Journal of The Electrochemical Society*, *140*(6), 1526. https://doi.org/10.1149/1.2221597

E, J., Xu, S., Deng, Y., Zhu, H., Zuo, W., Wang, H., Chen, J., Peng, Q., & Zhang, Z. (2018). Investigation on thermal performance and pressure loss of the fluid cold-plate used in thermal management system of the battery pack. *Applied Thermal Engineering*, *145*, 552–568. https://doi.org/https://doi.org/10.1016/j.applthermaleng.2018.09.048

Ekström, H., Fridholm, B., & Lindbergh, G. (2018). Comparison of lumped diffusion models for voltage prediction of a lithium-ion battery cell during dynamic loads. *Journal of Power Sources*, *402*, 296–300. https://doi.org/https://doi.org/10.1016/j.jpowsour.2018.09.020

Energy, U. S. D. of. (2021). Chapter 3: Lithium-Ion Batteries. In *Energy Storage Handbook (ESHB)*. Sandia National Laboratories. https://www.sandia.gov/app/uploads/sites/163/2021/09/ESHB-Ch3_Lithium-Batteries_Preger.pdf

Fang, R., Ge, H., Wang, Z., Li, Z., & Zhang, J. (2020). A Two-Dimensional Heterogeneous Model of Lithium-Ion Battery and Application on Designing Electrode with Non-Uniform Porosity. *Journal of The Electrochemical Society*, *167*(13), 130513. https://doi.org/10.1149/1945-7111/abb83a

Felix Omojola, A., Omata Ilabija, C., Ifeanyi Onyeka, C., Ishiwu, J. I., Olaleye, T. G., Juliet Ozoemena, I., & Nzereogu, P. U. (2024). Artificial Intelligence-Driven Strategies for Advancing Lithium-Ion Battery Performance and Safety. *International Journal of Advances in Engineering and Management*, *6*(10), 452–484. https://doi.org/10.35629/5252-0610452484

Feng, H., Wang, Z., & Zhang, F. (2021). A Comprehensive Evaluation of the Influence of Major Hysteresis on State of Charge Prediction of LiNiMnCoO2 Battery. *Frontiers in Energy Research*, *9*. https://doi.org/10.3389/fenrg.2021.666092

Feng, X., Ouyang, M., Liu, X., Lu, L., Xia, Y., & He, X. (2018). Thermal runaway mechanism of lithium ion battery for electric vehicles: A review. *Energy Storage Materials*, *10*, 246–267. https://doi.org/https://doi.org/10.1016/j.ensm.2017.05.013

Friedrich, F., Zünd, T., Hoefling, A., Tübke, J., & Gasteiger, H. A. (2022). Classification of Heat Evolution Terms in Li-Ion Batteries Regarding the OCV Hysteresis in a Li- and Mn-Rich NCM Cathode Material in Comparison to NCA. *Journal of The Electrochemical Society*, *169*(4), 040547. https://doi.org/10.1149/1945-7111/ac6541

Gopinadh, S. V, Anoopkumar, V., Ansari, Md. J. N., Srivastava, D., Raj M., A., John, B., Samridh, A., Vijayakumar, P. S., & Mercy, T. D. (2022). Lithium-Ion Pouch Cells: An Overview. In M. K. Jayaraj, A. Antony, & P. P. Subha (Eds.), *Energy Harvesting and Storage: Fundamentals and*

Materials (pp. 209–224). Springer Nature Singapore. https://doi.org/10.1007/978-981-19-4526-7_7

Guo, M., Sikha, G., & White, R. E. (2011). Single-Particle Model for a Lithium-Ion Cell: Thermal Behavior. *Journal of The Electrochemical Society*, *158*(2), A122. https://doi.org/10.1149/1.3521314

Han, J. W., Garud, K. S., Hwang, S. G., & Lee, M. Y. (2022). Experimental Study on Dielectric Fluid Immersion Cooling for Thermal Management of Lithium-Ion Battery. *Symmetry*, *14*(10). https://doi.org/10.3390/sym14102126

Han, S., Tang, Y., & Khaleghi Rahimian, S. (2021). A numerically efficient method of solving the full-order pseudo-2-dimensional (P2D) Li-ion cell model. *Journal of Power Sources*, *490*, 229571. https://doi.org/https://doi.org/10.1016/j.jpowsour.2021.229571

Han, U., & Lee, H. (2022). *Pubs Purdue e-Pubs International Refrigeration and Air Conditioning Conference School of Mechanical Engineering 2022 19 th International Refrigeration and Air Conditioning Conference at Purdue*. https://docs.lib.purdue.edu/iracc

Haosong He. (2024). *Novel battery thermal management systems for electric vehicles*. https://doi.org/10.26174/thesis.lboro.27038005.v1

Haran, B. S., Popov, B. N., & White, R. E. (1998). Determination of the hydrogen diffusion coefficient in metal hydrides by impedance spectroscopy. *Journal of Power Sources*, *75*(1), 56–63. https://doi.org/https://doi.org/10.1016/S0378-7753(98)00092-5

Hatchard, T., MacNeil, D., Stevens, D. A., Christensen, L., & Dahn, J. R. (2000). Importance of Heat Transfer by Radiation in Li-Ion Batteries during Thermal Abuse. *Electrochem. Solid-State Lett.*, *3*, 305–308.

He, H. (2024). *Novel battery thermal management systems for electric vehicles*. Loughborough University.

Horiba, T. (2014). Lithium-Ion Battery Systems. *Proceedings of the IEEE*, *102*(6), 939–950. https://doi.org/10.1109/JPROC.2014.2319832

Hua, J., Vie, P. J. S., & Wind, J. (2023). Fast Estimation of Entropy Profiles for Lithium-Ion Batteries. *Electrochemical Society Meeting Abstracts 244*, *8*, 3428.

Ianniciello, L., Biwolé, P. H., & Achard, P. (2018). Electric vehicles batteries thermal management systems employing phase change materials. *Journal of Power Sources*, *378*, 383–403. https://doi.org/https://doi.org/10.1016/j.jpowsour.2017.12.071

IEA. (2020). *Global electric car stock, 2010-2019*.

Jaguemont, J., Boulon, L., & Dubé, Y. (2016). Characterization and modeling of a hybrid-electric-vehicle lithium-ion battery pack at low temperatures. *IEEE Transactions on Vehicular Technology*, *65*(1), 1–14. https://doi.org/10.1109/TVT.2015.2391053

Jeon, D. H. (2014). Numerical modeling of lithium ion battery for predicting thermal behavior in a cylindrical cell. *Current Applied Physics*, *14*(2), 196–205. https://doi.org/10.1016/j.cap.2013.11.006

Jindal, P., Katiyar, R., & Bhattacharya, J. (2022). Evaluation of accuracy for Bernardi equation in estimating heat generation rate for continuous and pulse-discharge protocols in LFP and NMC based Li-ion batteries. *Applied Thermal Engineering*, *201*. https://doi.org/10.1016/j.applthermaleng.2021.117794

Kako, S. (2023). A Comparative Study about Accuracy Levels of Resistance Temperature Detectors RTDs Composed of Platinum, Copper, and Nickel. *Al-Nahrain Journal for Engineering Sciences*, *26*(3), 216–225. https://doi.org/10.29194/NJES.26030216

Kantharaj, R., & Marconnet, A. (2019). Heat Generation and Thermal Transport in Lithium-Ion Batteries: A Scale-Bridging Perspective. *Nanoscale and Microscale Thermophysical Engineering*, *23*, 1–29. https://doi.org/10.1080/15567265.2019.1572679

Kemper, P., Li, S. E., & Kum, D. (2015). Simplification of pseudo two dimensional battery model using dynamic profile of lithium concentration. *Journal of Power Sources*, *286*, 510–525. https://doi.org/https://doi.org/10.1016/j.jpowsour.2015.03.134

Khaleghi Rahimian, S., Rayman, S., & White, R. E. (2013). Extension of physics-based single particle model for higher charge–discharge rates. *Journal of Power Sources*, *224*, 180–194. https://doi.org/https://doi.org/10.1016/j.jpowsour.2012.09.084

Kim, S., & Kim, H. (2016). A new metric of absolute percentage error for intermittent demand forecasts. *International Journal of Forecasting*, *32*(3), 669–679. https://doi.org/10.1016/j.ijforecast.2015.12.003

Koech, A. K., Mwandila, G., & Mulolani, F. (2024). A review of improvements on electric vehicle battery. In *Heliyon* (Vol. 10, Issue 15). Elsevier Ltd. https://doi.org/10.1016/j.heliyon.2024.e34806

Korthauer, R. (2018). Lithium-Ion Batteries: Basics and Applications. In *Lithium-Ion Batteries: Basics and Applications*. https://doi.org/10.1007/978-3-662-53071-9

Kovács, G., Kocsis Szürke, S., & Fischer, S. (2025). Investigation of Convective and Radiative Heat Transfer of 21700 Lithium-Ion Battery Cells. *Batteries*, *11*(7). https://doi.org/10.3390/batteries11070246

Li, C., Cui, N., Wang, C., & Zhang, C. (2021). Reduced-order electrochemical model for lithium-ion battery with domain decomposition and polynomial approximation methods. *Energy*, *221*, 119662. https://doi.org/https://doi.org/10.1016/j.energy.2020.119662

Li, H., Duan, Q., Zhao, C., Huang, Z., & Wang, Q. (2019). Experimental investigation on the thermal runaway and its propagation in the large format battery module with Li(Ni1/3Co1/3Mn1/3)O2 as cathode. *Journal of Hazardous Materials*, *375*, 241–254. https://doi.org/https://doi.org/10.1016/j.jhazmat.2019.03.116

Li, K., Yan, J., Chen, H., & Wang, Q. (2018). Water cooling based strategy for lithium ion battery pack dynamic cycling for thermal management system. *Applied Thermal Engineering*, *132*, 575–585. https://doi.org/10.1016/j.applthermaleng.2017.12.131

Liang, Y., Zhao, C.-Z., Yuan, H., Chen, Y., Zhang, W., Huang, J.-Q., Yu, D., Liu, Y., Titirici, M.-M., Chueh, Y.-L., Yu, H., & Zhang, Q. (2019). A review of rechargeable batteries for portable electronic devices. *InfoMat*, *1*(1), 6–32. https://doi.org/https://doi.org/10.1002/inf2.12000

Liu, C., Xu, D., Weng, J., Zhou, S., Li, W., Wan, Y., Jiang, S., Zhou, D., Wang, J., & Huang, Q. (2020). Phase Change Materials Application in Battery Thermal Management System: A Review. *Materials*, *13*, 4622. https://doi.org/10.3390/ma13204622

Liu, J., Chen, H., Huang, S., Jiao, Y., & Chen, M. (2023). Recent Progress and Prospects in Liquid Cooling Thermal Management System for Lithium-Ion Batteries. *Batteries*, *9*, 400. https://doi.org/10.3390/batteries9080400

Liu, Y. (2025). Electrical and Thermal Simulations of a Lithium-Ion Battery Cell: A Comparative Study of Commercial Software Platforms. In *Japan J Res* (Vol. 6).

Liu, Y., & Zhang, J. (2019). Design a J-type air-based battery thermal management system through surrogate-based optimization. *Applied Energy*, *252*, 113426. https://doi.org/https://doi.org/10.1016/j.apenergy.2019.113426

Lu, X., Bertei, A., Finegan, D. P., Tan, C., Daemi, S. R., Weaving, J. S., O'Regan, K. B., Heenan, T. M. M., Hinds, G., Kendrick, E., Brett, D. J. L., & Shearing, P. R. (2020). 3D microstructure design of lithium-ion battery electrodes assisted by X-ray nano-computed tomography and modelling. *Nature Communications*, *11*(1). https://doi.org/10.1038/s41467-020-15811-x

Lu, X., Li, Z., Zou, J., Peng, D., Hu, W., Zhong, Y., Li, P., Su, S., Wang, X., Wang, S., Zhao, Z., & Zhang, J. (2023). Spent lithium manganate batteries for sustainable recycling: A review. In *Frontiers in Materials* (Vol. 10). Frontiers Media S.A. https://doi.org/10.3389/fmats.2023.1152018

Maknikar, S. K., & Pawar, A. M. (2023). Application of phase change material (PCM) in battery thermal management system (BTMS): A critical review. *Materials Today: Proceedings*. https://doi.org/https://doi.org/10.1016/j.matpr.2023.08.329

Mangaiyarkarasi, P., & Jayaganthan, R. (2024). Investigation on Thermal Characteristics and Performance of Cylindrical Lithium-Ion Battery Pack Using P2D Model with Varied Electrode Chemistries. *IEEE Access*, *12*, 76781–76793. https://doi.org/10.1109/ACCESS.2024.3400910

Mevawalla, A., Panchal, S., Tran, M. K., Fowler, M., & Fraser, R. (2020). Mathematical heat transfer modeling and experimental validation of lithium-ion battery considering: Tab and surface temperature, separator, electrolyte resistance, anode-cathode irreversible and reversible heat. *Batteries*, *6*(4), 1–26. https://doi.org/10.3390/batteries6040061

Milián, Y. E., Gutiérrez, A., Grágeda, M., & Ushak, S. (2017). A review on encapsulation techniques for inorganic phase change materials and the influence on their thermophysical properties. *Renewable and Sustainable Energy Reviews*, *73*, 983–999. https://doi.org/https://doi.org/10.1016/j.rser.2017.01.159

Murashko, K. A., Pyrhönen, J., & Jokiniemi, J. (2020). Determination of the through-plane thermal conductivity and specific heat capacity of a Li-ion cylindrical cell. *International Journal of Heat and Mass Transfer*, *162*. https://doi.org/10.1016/j.ijheatmasstransfer.2020.120330

Nasiri, M., & Hadim, H. (2025). Thermal management of Li-ion batteries using phase change materials: Recent advances and future challenges. In *Journal of Energy Storage* (Vol. 111). Elsevier Ltd. https://doi.org/10.1016/j.est.2025.115440

Nazari, A., & Farhad, S. (2017). Heat generation in lithium-ion batteries with different nominal capacities and chemistries. *Applied Thermal Engineering*, *125*, 1501–1517. https://doi.org/10.1016/j.applthermaleng.2017.07.126

Nazir, H., Batool, M., Bolivar Osorio, F. J., Isaza-Ruiz, M., Xu, X., Vignarooban, K., Phelan, P., Inamuddin, & Kannan, A. M. (2019). Recent developments in phase change materials for energy storage applications: A review. *International Journal of Heat and Mass Transfer*, *129*, 491–523. https://doi.org/https://doi.org/10.1016/j.ijheatmasstransfer.2018.09.126

Ng, B., Coman, P. T., Mustain, W. E., & White, R. E. (2020). Non-destructive parameter extraction for a reduced order lumped electrochemical-thermal model for simulating Li-ion full-cells. *Journal of Power Sources*, *445*, 227296. https://doi.org/https://doi.org/10.1016/j.jpowsour.2019.227296

Nicholls, R. A., Moghimi, M. A., & Sehhat, S. (2024). Thermal performance analysis of battery modules with passive cooling under different cycling loads in electric vehicles. *Journal of Energy Storage*, *94*, 112349. https://doi.org/https://doi.org/10.1016/j.est.2024.112349

Ning, J., & Zhang, L. (2015). *Method for Determining the SOC-OCV Curve of Lithium Battery*. Beiqi Foton Motor Co., Ltd. https://worldwide.espacenet.com/patent/search/family/050235209/publication/CN104297690A

Oh, H., Shin, J., Kang, T., Kim, W., & Lee, J. M. (2024). Analysis of Aging in Lithium-ion Batteries: Fundamental Modeling and Parameter Investigation. *IFAC-PapersOnLine*, *58*(14), 500–505. https://doi.org/10.1016/j.ifacol.2024.08.386

Olabi, A. G., Maghrabie, H. M., Adhari, O. H. K., Sayed, E. T., Yousef, B. A. A., Salameh, T., Kamil, M., & Abdelkareem, M. A. (2022). Battery thermal management systems: Recent progress and challenges. *International Journal of Thermofluids*, *15*, 100171. https://doi.org/https://doi.org/10.1016/j.ijft.2022.100171

Özdemir, T., Ekici, Ö., & Köksal, M. (2021). Numerical and experimental investigation of the thermal and electrical characteristics of a lithium ion cell. *E3S Web of Conferences*, *321*. https://doi.org/10.1051/e3sconf/202132103007

Paccha-Herrera, E., Calderón-Muñoz, W. R., Orchard, M., Jaramillo, F., & Medjaher, K. (2020). Thermal modeling approaches for a licoo2 lithium-ion battery—a comparative study with experimental validation. *Batteries*, *6*(3), 1–23. https://doi.org/10.3390/batteries6030040

Patel, J., Patel, R., Saxena, R., & Nair, A. (2025). Experimental investigation of thermal characteristics of a 12S1P Li-ion NMC-21700 battery module under different environments for EV applications. *International Journal of Thermofluids*, *26*. https://doi.org/10.1016/j.ijft.2025.101084

Pesaran, A. A. (2002). *Battery thermal models for hybrid vehicle simulations*.

Pesaran, A. A., & Burch, S. D. (1997). *Thermal Performance of EV and HEV Battery Modules and Packs Prepared under FWP HV71* (Vol. 7).

Petzl, M., & Danzer, M. A. (2013). Advancements in OCV measurement and analysis for lithium-ion batteries. *IEEE Transactions on Energy Conversion*, *28*(3), 675–681. https://doi.org/10.1109/TEC.2013.2259490

Pielichowska, K., & Pielichowski, K. (2014). Phase change materials for thermal energy storage. *Progress in Materials Science*, *65*, 67–123. https://doi.org/https://doi.org/10.1016/j.pmatsci.2014.03.005

Plett, G. L. (2015). *Battery Management Systems* (Issue v. 1). Artech House. https://books.google.fi/books?id=M-TasgEACAAJ

Purwamargapratala, Y., Sudaryanto, & Akbar, dan F. (2020). Neutron tomography study of a lithium-ion coin battery. *Journal of Physics: Conference Series*, *1436*(1). https://doi.org/10.1088/1742-6596/1436/1/012029

Qi, C., Wang, H., Li, M., Li, C., Li, Y., Wei, N., & Zhang, H. (2025). Study on the Multi-Stage Evolution of Thermal Runaway and the Flammability Threshold of Gas Generation in Lithium Iron Phosphate Batteries Based on SOC Gradient. *Micromachines*, *16*(5). https://doi.org/10.3390/mi16050544

Rao, Z., Wang, S., & Zhang, G. (2011). Simulation and experiment of thermal energy management with phase change material for ageing LiFePO4 power battery. *Energy Conversion and Management*, *52*(12), 3408–3414. https://doi.org/https://doi.org/10.1016/j.enconman.2011.07.009

Sharifi, N., Roesler, D., Gold, A., & Shabgard, H. (2024). *Thermal Management System for Lithium-Ion Batteries Using Phase Change Material, Heat Pipes and Fins*. https://doi.org/10.1115/IMECE2023-113854

Sheng, L., Zhang, H., Su, L., Zhang, Z., Zhang, H., Li, K., Fang, Y., & Ye, W. (2021). Effect analysis on thermal profile management of a cylindrical lithium-ion battery utilizing a cellular liquid cooling jacket. *Energy*, *220*, 119725. https://doi.org/https://doi.org/10.1016/j.energy.2020.119725

Shi, H., Wang, L., Wang, S., Fernandez, C., Xiong, X., Dablu, B. E., & Xu, W. (2022). A novel lumped thermal characteristic modeling strategy for the online adaptive temperature and parameter co-estimation of vehicle lithium-ion batteries. *Journal of Energy Storage*, *50*. https://doi.org/10.1016/j.est.2022.104309

Shinde, S. R., Song, Y., & Sahraei, E. (2023). Modeling Electric Vehicle's Battery Module using Computational Homogenization Approach. *International Journal of Energy Research*, *2023*. https://doi.org/10.1155/2023/9210078

Siddique, A. R. M., Mahmud, S., & Heyst, B. Van. (2018). A comprehensive review on a passive (phase change materials) and an active (thermoelectric cooler) battery thermal management system and their limitations. *Journal of Power Sources*, *401*, 224–237. https://doi.org/https://doi.org/10.1016/j.jpowsour.2018.08.094

Stan, A.-I., Świerczyński, M., Stroe, D.-I., Teodorescu, R., & Andreasen, S. J. (2014). Lithium ion battery chemistries from renewable energy storage to automotive and back-up power applications — An overview. *2014 International Conference on Optimization of Electrical and Electronic Equipment (OPTIM)*, 713–720. https://doi.org/10.1109/OPTIM.2014.6850936

Steinhardt, M., Barreras, J. V., Ruan, H., Wu, B., Offer, G. J., & Jossen, A. (2022). Meta-analysis of experimental results for heat capacity and thermal conductivity in lithium-ion batteries: A critical review. In *Journal of Power Sources* (Vol. 522). Elsevier B.V. https://doi.org/10.1016/j.jpowsour.2021.230829

Sun, T., Yan, Y., Wang, X., Rasool, G., Zhang, K., & Li, T. (2025). A comprehensive study on heat transfer mechanism and thermal runaway suppression of the lithium-ion battery. In *International Journal of Heat and Mass Transfer* (Vol. 245). Elsevier Ltd. https://doi.org/10.1016/j.ijheatmasstransfer.2025.127027

Tardy, F., & Sami, S. M. (2009). Thermal analysis of heat pipes during thermal storage. *Applied Thermal Engineering*, *29*(2), 329–333. https://doi.org/https://doi.org/10.1016/j.applthermaleng.2008.02.037

Teliz, E., Zinola, C. F., & Díaz, V. (2022). Identification and quantification of ageing mechanisms in Li-ion batteries by Electrochemical impedance spectroscopy. *Electrochimica Acta*, *426*. https://doi.org/10.1016/j.electacta.2022.140801

Thakur, A. K., Prabakaran, R., Elkadeem, M. R., Sharshir, S. W., Arıcı, M., Wang, C., Zhao, W., Hwang, J.-Y., & Saidur, R. (2020). A state of art review and future viewpoint on advance cooling techniques for Lithium–ion battery system of electric vehicles. *Journal of Energy Storage*, *32*, 101771. https://doi.org/https://doi.org/10.1016/j.est.2020.101771

Torregrosa, A. J., Broatch, A., Olmeda, P., & Agizza, L. (2024). A semi-empirical model of the calendar ageing of lithium-ion batteries aimed at automotive and deep-space applications. *Journal of Energy Storage*, *80*. https://doi.org/10.1016/j.est.2023.110388

Tran, M. K., Dacosta, A., Mevawalla, A., Panchal, S., & Fowler, M. (2021). Comparative study of equivalent circuit models performance in four common lithium-ion batteries: LFP, NMC, LMO, NCA. *Batteries*, *7*(3). https://doi.org/10.3390/batteries7030051

Tran, M. K., Mathew, M., Janhunen, S., Panchal, S., Raahemifar, K., Fraser, R., & Fowler, M. (2021). A comprehensive equivalent circuit model for lithium-ion batteries, incorporating the effects of state of health, state of charge, and temperature on model parameters. *Journal of Energy Storage*, *43*. https://doi.org/10.1016/j.est.2021.103252

Tran, M.-K., Mevawalla, A., Aziz, A., Panchal, S., Xie, Y., & Fowler, M. (2022). A Review of Lithium-Ion Battery Thermal Runaway Modeling and Diagnosis Approaches. *Processes*, *10*, 1192. https://doi.org/10.3390/pr10061192

Trumony. (2025, May 15). *Elecric Vehicle 18650 Li-ion Battery Snake Cooling Tube for Battery Pack Cooling System*.

Velev, B., Djudzhev, B., Dimitrov, V., & Hinov, N. (2024). Comparative Analysis of Lithium-Ion Batteries for Urban Electric/Hybrid Electric Vehicles. *Batteries*, *10*(6). https://doi.org/10.3390/batteries10060186

Vikram, S., Vashisht, S., Rakshit, D., & Wan, M. P. (2024). Recent advancements and performance implications of hybrid battery thermal management systems for Electric Vehicles. *Journal of Energy Storage*, *90*, 111814. https://doi.org/https://doi.org/10.1016/j.est.2024.111814

Walvekar, H., Beltran, H., Sripad, S., & Pecht, M. (2022). Implications of the Electric Vehicle Manufacturers' Decision to Mass Adopt Lithium-Iron Phosphate Batteries. *IEEE Access*, *10*, 63834–63843. https://doi.org/10.1109/ACCESS.2022.3182726

Wang, Y., Lu, Q., & Cheng, Y. (2025). An optimization study on the performance of air-cooling system for energy storage battery packs using a novel thermoelectric coupling model. *Applied Thermal Engineering*, *270*. https://doi.org/10.1016/j.applthermaleng.2025.126199

Wu, Q., Huang, R., & Yu, X. (2023). Measurement of thermophysical parameters and thermal modeling of 21,700 cylindrical battery. *Journal of Energy Storage*, *65*. https://doi.org/10.1016/j.est.2023.107338

Wu, W., Liu, J., Liu, M., Rao, Z., Deng, H., Wang, Q., Qi, X., & Wang, S. (2020). An innovative battery thermal management with thermally induced flexible phase change material. *Energy Conversion and Management*, *221*, 113145. https://doi.org/10.1016/j.enconman.2020.113145

Wu, X., Zhu, Z., Zhang, H., Xu, S., Fang, Y., & Yan, Z. (2020). Structural optimization of light-weight battery module based on hybrid liquid cooling with high latent heat PCM. *International Journal of Heat and Mass Transfer*, *163*, 120495. https://doi.org/https://doi.org/10.1016/j.ijheatmasstransfer.2020.120495

Xia, G., Cao, L., & Bi, G. (2017). A review on battery thermal management in electric vehicle application. *Journal of Power Sources*, *367*, 90–105. https://doi.org/https://doi.org/10.1016/j.jpowsour.2017.09.046

Xiao, B., & Faghri, A. (2008). A three-dimensional thermal-fluid analysis of flat heat pipes. *International Journal of Heat and Mass Transfer*, *51*(11), 3113–3126. https://doi.org/https://doi.org/10.1016/j.ijheatmasstransfer.2007.08.023

Xie, Y., Shi, S., Tang, J., Wu, H., & Yu, J. (2018). Experimental and analytical study on heat generation characteristics of a lithium-ion power battery. *International Journal of Heat and Mass Transfer*, *122*, 884–894. https://doi.org/10.1016/j.ijheatmasstransfer.2018.02.038

Yang, N., Zhang, X., Li, G., & Hua, D. (2015). Assessment of the forced air-cooling performance for cylindrical lithium-ion battery packs: A comparative analysis between aligned and staggered cell arrangements. *Applied Thermal Engineering*, *80*, 55–65. https://doi.org/https://doi.org/10.1016/j.applthermaleng.2015.01.049

Yoshino, A. (2012). The Birth of the Lithium-Ion Battery. *Angewandte Chemie International Edition*, *51*(24), 5798–5800. https://doi.org/https://doi.org/10.1002/anie.201105006

Zeng, X., Ye, L., Wang, C., Wu, D., Zhong, K., & Kong, Z. (2024). Highly stable solid-solid phase change materials for battery thermal management systems. *Journal of Energy Storage*, *88*, 111495. https://doi.org/https://doi.org/10.1016/j.est.2024.111495

Zhang, D., Dey, S., Couto, L. D., & Moura, S. J. (2020). Battery Adaptive Observer for a Single-Particle Model with Intercalation-Induced Stress. *IEEE Transactions on Control Systems Technology*, *28*(4), 1363–1377. https://doi.org/10.1109/TCST.2019.2910797

Zhao, Y., Zou, B., Zhang, T., Jiang, Z., Ding, J., & Ding, Y. (2022). A comprehensive review of composite phase change material based thermal management system for lithium-ion batteries. *Renewable and Sustainable Energy Reviews*, *167*, 112667. https://doi.org/https://doi.org/10.1016/j.rser.2022.112667

Zhao, Z. (2023). Applications of Nanotechnology: lithium-ion based batteries in electric vehicles. In *Highlights in Science, Engineering and Technology EMIS* (Vol. 2022).

Zhao, Z., Kollmeyer, P. J., Lempert, J. M., & Emadi, A. (2021). Experimental comparison of two liquid cooling methods for ultrafast charging lithium-ion battery modules. *2021 IEEE Transportation Electrification Conference and Expo, ITEC 2021*, 46–51. https://doi.org/10.1109/ITEC51675.2021.9490034

Zhi, M., Fan, R., Yang, X., Zheng, L., Yue, S., Liu, Q., & He, Y. (2022). Recent research progress on phase change materials for thermal management of lithium-ion batteries. *Journal of Energy Storage*, *45*, 103694. https://doi.org/https://doi.org/10.1016/j.est.2021.103694

Zilberman, I., Spingler, F. B., Rheinfeld, A., & Jossen, A. (2018). Temperature Path Dependent Voltage and Thermal Expansion Hysteresis in Li-Ion Cells. *ECS Meeting Abstracts*, *MA2018-01*(1), 34. https://doi.org/10.1149/MA2018-01/1/34

Appendix 1. Experimental and Modelling Temperature Results at Different C-Rate

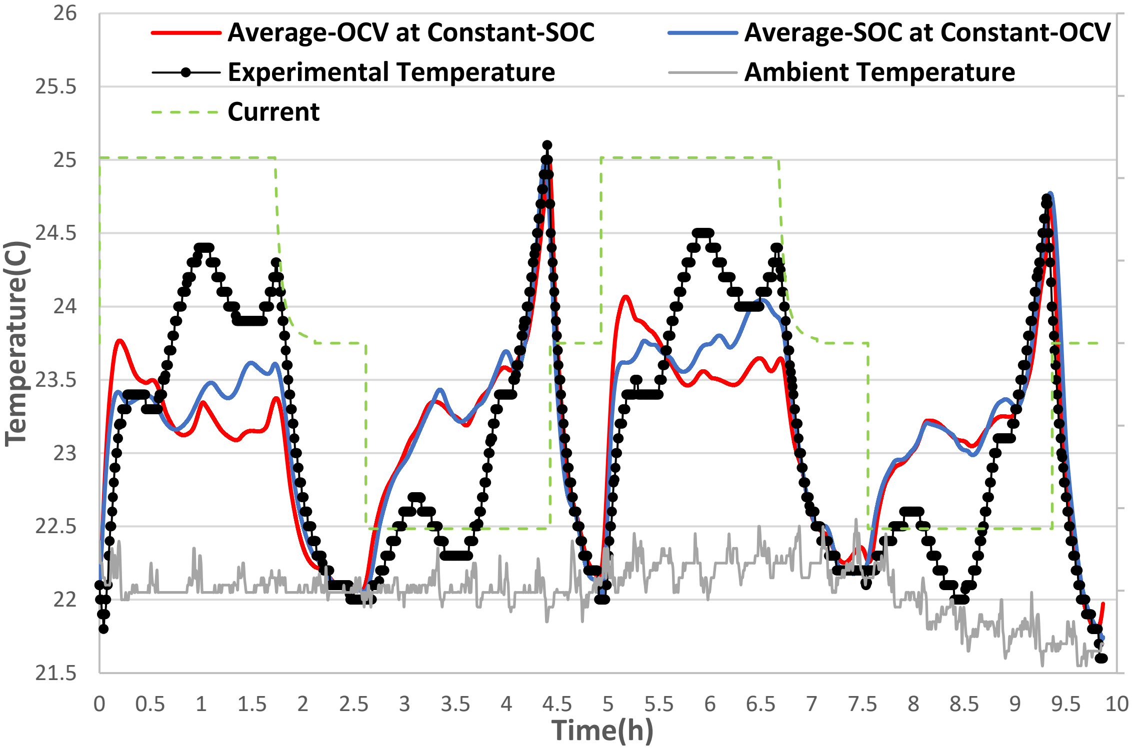

Figure A1 Experimental and Model-predicted Temperature Evolution During Cyclic Charge–discharge at 0.5C.

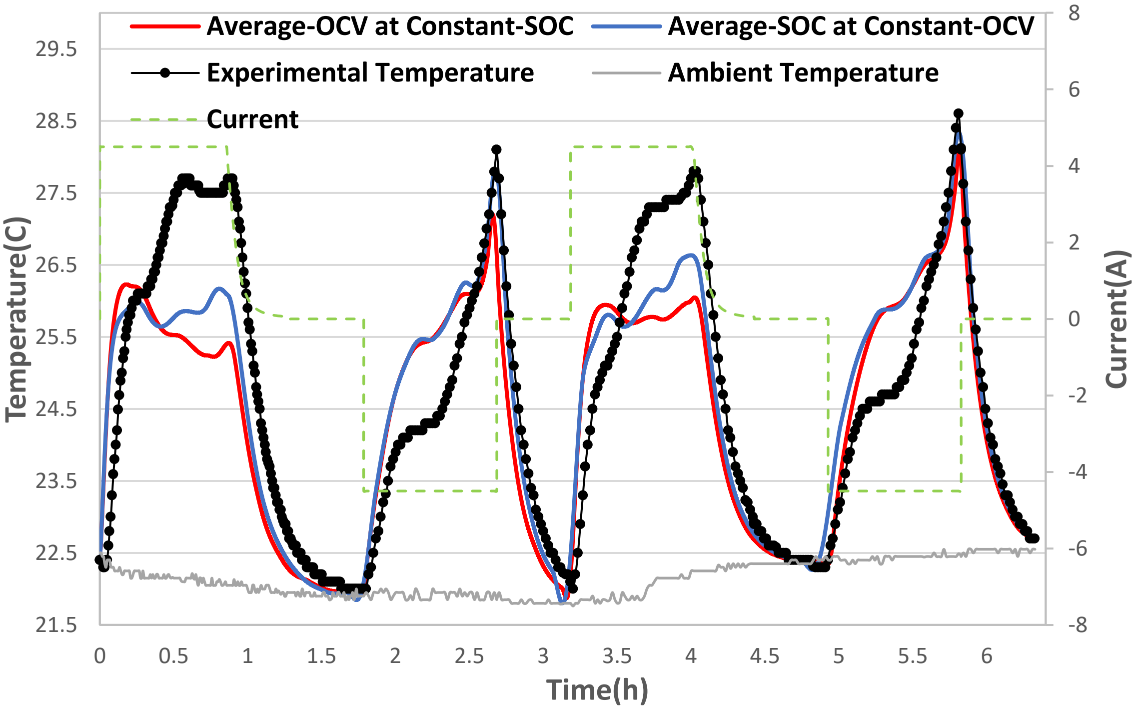

Figure A2 Experimental and Model-predicted Temperature Evolution During Cyclic Charge–discharge at 1C.

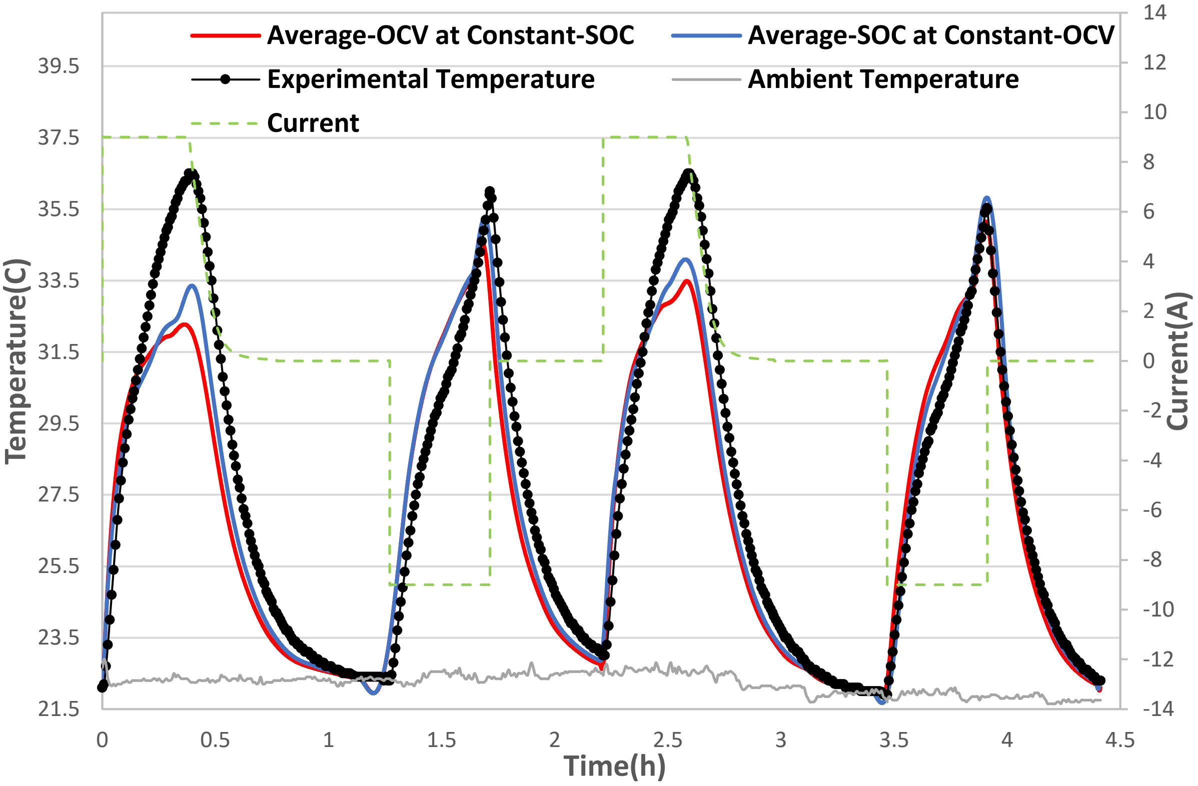

Figure A3 Experimental and Model-predicted Temperature Evolution During Cyclic Charge–discharge at 2C.